SCHOOL OF MATHEMATICAL SCIENCES
QUEENSLAND UNIVERSITY OF TECHNOLOGY

MODELLING OF VACUUM DRYING OF AUSTRALIAN HARDWOOD SPECIES

Adam Lloyd Redman

Bachelor of Engineering, UTAS
Graduate Diploma Engineering (Honours), UTAS
Master of Science in Engineering (M. Eng. Sc.), UTAS

Submitted in fulfilment of the requirement for the degree of Doctor of Philosophy in the Science and Engineering Faculty, Queensland University of Technology

Principal Supervisor: Prof. Ian Turner
Associate Supervisor: Prof. Patrick Perré
Associate Supervisor: Dr. Henri Bailleres
Associate Supervisor: Dr. Elliot Carr

2017

Keywords

Diffusivity, Permeability, Mass Transfer, Hardwood, Anisotropy, Wood Anatomy, Shrinkage, Viscoelasticity, Heat and Mass Transfer, Modelling, Vacuum Drying, Sensitivity Analysis, Experimental Validation, Drying Stress, Tsai-Wu Failure, Finite Element Analysis, Drying, Stress, Strain

Abstract

Drying hardwoods is the most expensive and time-consuming operation in the hardwood primary processing value chain. Conventional kiln drying and vacuum kiln drying both reduce drying time while controlling dried quality, but usually at an increased cost when compared to simple air-drying (i.e. drying outside in prevailing ambient weather conditions). Furthermore, most 25 mm thick Australian hardwoods can take anywhere from around 2 weeks to 4 months to dry using a kiln. Hence, improving the kiln drying process, by using classical techniques to run a series of optimisation drying trials, typically takes up to 5 years to optimise drying time, quality and cost. Therefore, the Australian hardwood processing industry realise the need to model the heat and mass transfer processes and associated stress-related degrade that evolve during drying, and use the simulations to optimise and reduce operational costs.

There are two main research objectives related to this study. The first is to develop a robust and precise hardwood heat and mass transfer drying model for vacuum and conventional drying. The second is to develop a finite element analysis stress/strain model able to predict stress-related drying-defect failure observed during vacuum and conventional drying.

The focus of the first part of this research is to adapt *TransPore*, a comprehensive heat and mass transfer softwood drying model, originally designed for simulating drying in softwoods and other porous media, to simulate drying of four highly commercial Australian hardwood species, namely: messmate (*Eucalyptus obliqua*), jarrah (*Eucalyptus marginata*), blackbutt (*Eucalyptus pilularis*) and spotted gum (*Corymbia citriodora*).

These species were chosen based on their vastly different wood properties and drying characteristics. The model encompasses multiscale and multiphysics descriptions of drying phenomena, where heat and mass transfer is governed by macroscopic laws describing conservation of liquid, water vapour, air and enthalpy, averaged over representative volumes. A critical component of this work is the measurement of a number of key wood properties and the inclusion of deterministic boundary condition data, derived from a series of vacuum and conventional drying trials, for each species. The second part of the research uses the time-based, discrete, moisture-content field output data from the *TransPore* model, as input data into a finite element analysis stress/strain model using a quasi-static solver in the *Strand7*[1] software. The stress related degrade, end splitting and surface checking, is investigated using Tsai-Wu failure criteria.

Compared with drying trials performed at the Salisbury Research Facility in Brisbane and various sawmills around Australia, the average moisture content and temperature simulation output using *TransPore* are able to predict the average moisture content during drying within an error of 2 to 10% depending on species, for both vacuum and conventional drying. A model sensitivity analysis of end-point moisture content determination is able to rank input variables according to sensitivity and found that wood density, desorption and transverse diffusion coefficient parameters were the most sensitive, and wood porosity the least sensitive. Measurement of wood water relationships, desorption isotherms, density, shrinkage characteristics and cell morphology improved the predictive capacity of the model. A highlight of the work is that by using measured diffusivity values the accuracy of the heat and mass transfer model is greatly

---

[1] http://www.strand7.com/

improved.

Results of the stress/strain model accurately predicted observed drying end splitting degrade between messmate and spotted gum species, as well as the differences in end splitting observed between vacuum and conventional drying. The finite element analysis model is able to predict the greater susceptibility of messmate species to end splitting and surface checking compared with spotted gum.

The outcomes of this research are important in that they provide the hardwood industry with a tool that can accurately determine the drying rate of a wide range of hardwood species, using different types of drying methods such as vacuum and conventional drying. We now recognise the key sensitive wood parameters necessary to accurately model Australian hardwood species, and without their measurement, robust modelling is not possible. This work contributes to a greater understanding of stress degrade formation in wood during drying, and may be used in future work to optimise drying times and limit degrade. An important contribution of the research is the provision of a modelling tool that makes it possible to reduce the time required to perform applied drying research, thus offering a greater understanding of the underlying heat and mass transfer phenomena that arise during vacuum drying. The new model is able to accurately predict the drying of Australian hardwoods and ultimately can be used by practitioners to optimise drying time, quality and overall costs.

Acknowledgements

Firstly, I would like to thank my principal supervisor Professor Ian Turner for his support, time and encouragement over the past years. I also express thanks to Professor Patrick Perré for his invaluable guidance, direction and hosting me in Nancy, France. To my supervisor, work colleague and friend Henri Bailleres, thanks for your encouragement, belief and ongoing support. Lastly, I would like to thank associate supervisor Elliot Carr and Chapter 6 co-author Benoit Gilbert for your support and guidance throughout key components of this work.

The substantial contributions of Centrale Supelec, Université Paris-Saclay, ENGREF, AgroParisTech, Queensland University of Technology (QUT), Queensland Cyber Infrastructure Foundation (QCIF), Forest and Wood Products Australia (FWPA), and the Queensland Government Department of Agriculture and Fisheries (DAF), to the successful undertaking of this collaborative project are gratefully acknowledged.

I would also like to thank my friends and family who have put up with my madness over the past years while completing this body of work. I would specifically like to dedicate this work to my late father and best mate, Lloyd Redman. Finally, I extend my biggest thanks to my very understanding wife, Khannasone Vongthongkham and wonderful daughter, Amelie Redman. You guys keep me sane.

Contents

List of Tables

List of Figures

List of Publications

1. Redman A.L., Bailleres H., Perré P. (2011). *Characterization of viscoelastic, shrinkage and transverse anatomy properties of four Australian hardwood species.* Wood Material Science & Engineering 6: p. 95-104.
2. Redman A.L., Bailleres H., Turner I., Perré P. (2012). *Mass transfer properties (permeability and mass diffusivity) of four Australian hardwood species*. BioResources, 7: p. 3410-3424.
3. Redman A.L., Bailleres H., Turner I., Perré P. (2016). *Characterisation of wood-water relationships and transverse anatomy and thier relationship to drying degrade*. Wood Science and Technology 50: p. 739-757.
4. Redman A.L., Bailleres H., Perré P., Carr E., Turner I. (2017). *A relevant and robust vacuum-drying model applied to hardwoods*. Wood Science and Technology. 51: p. 701-719.
5. Redman A.L., Bailleres H., Gilbert, B.P., Perré P., Carr E., Turner I. (2017). *Finite element analysis of stress-related degrade during drying of Corymbia citriodora and Eucalyptus obliqua.* Wood Science and Technology. Submitted for publication on 22 July 2017.

Statement of Original Authorship

The work contained in this thesis has not been previously submitted to meet requirements for an award at this or any other higher education institution. To the best of my knowledge and belief, the thesis contains no material previously published or written by another person except where due reference is made.

SIGNED:

QUT Verified Signature

DATE:

19/8/2017

Chapter 1
Introductory material

The purpose of this chapter is to introduce the reader to the research problem and provide a review of the relevant hardwood drying literature. Firstly, background information is provided describing the importance of wood drying and the motivation for developing a hardwood, vacuum and conventional, drying model. The physical and cell structure of wood is reviewed and related to the wood property characterisation components of the model development. A review of previous drying modelling conducted by other researchers with a highlighted summary of the *TransPore* heat and mass transfer model chosen for this study is included. The essential wood properties required for the *TransPore* model are examined. Finally, a review of previous stress/strain modelling approaches is provided emphasising the model chosen for this work including a description of the failure criteria selected to analyse surface check and end split stress-related drying-degrade. The chapter concludes with a summary of the thesis structure.

1.1 Introduction

When freshly sawn, wood contains a large quantity of water. Wood drying describes the removal of this water from wood before its intended end use. If the surfaces of wood are left exposed with sufficient airflow, wood will naturally dry over time to a final moisture content value dependent on the atmospheric temperature, pressure and humidity conditions. Among other properties, dried wood has the advantage over freshly sawn or ‘green’ wood, of having improved strength properties (i.e. hardness, stiffness, strength), is easier to transport, handle and process using wood-working machinery, and in terms of shrinkage and swelling is stable for end use.

The oldest form of wood drying is by racking sawn boards outdoors using sticks to separate them, allowing wind driven air to flow over the board surfaces. Eventually, the wood moisture content (MC) will equilibrate to the ambient conditions governed by the average local temperature and humidity conditions. Although effective, this can be a very slow process, particularly for many hardwood species, taking anywhere up to a year, or more, depending on the wood species and/or board thickness.

To make the process more time efficient, accelerated drying can be employed by increasing drying airflow and temperature, and by reducing ambient humidity and atmospheric pressure. This is common practice in the wood production industry where a range of different methods are used, mostly involving the use of a drying chamber or kiln [1].

Drying timber to produce material for high quality applications is an expensive and time-consuming operation. It is often referred to as the ‘bottleneck’ of the production process. The drying process consumes up to 70% of the energy and 90% of the time required to convert green logs into dried, value added products [2]. Additionally, estimates suggest that up to 10% degrade occurs in dried wood due to the drying process because of checking, collapse, distortion, and moisture variation [1]. Over the years, the timber industry worldwide, in conjunction with researchers, engineers and manufacturers, have strived to dry quality timber as quickly and cheaply as possible to maximise profitability. Therefore, the timber industry pursues techniques that can improve dried quality and reduce timber drying times and costs. Dried quality is defined by producing timber within acceptable drying induced degrade limits, and depends on customer requirements and the end use of the product [3].

Although the types of kiln used to accelerate wood drying are many and varied, they all have the same objectives; to (1) dry wood in the fastest and (2) most economical way possible with (3) minimal drying induced degrade, such as board end and surface splitting, large final moisture content variations and residual drying stresses. However, due to the complexity of wood drying, these three aims are mutually inclusive and one must find a balance between them to optimise the drying process. Drying time is usually restricted by the desired level of acceptable dried quality [3].

Timber drying depends on many different parameters, including the external drying conditions and the species of timber being dried. In general, industrial objectives are related to low drying costs, short drying time and reasonable drying quality. To achieve an overall satisfactory result of these industrial objectives, some compromises are required. The complex system of intricate physical and mechanical processes during timber drying includes external heat and mass flow in the kiln, coupled heat and mass transfer within wood, shrinkage induced stress deformation, and the mechanical memory behaviour of wood. Additional effects include chemical alterations leading to discolorations and physical phenomena, such as cell collapse.

Conventional kiln drying with controlled heating, humidity and air-flow under atmospheric pressure conditions is the primary method for drying timber in Australia [1]. In recent years, with emerging technological advancements in construction, computer control and less expensive materials, vacuum drying of hardwood timber has been proven in many applications to be a more economical alternative to drying using conventional methods, with similar or better quality outcomes [4]. For this reason, in 2008 Queensland Government's Department of Agriculture and Fisheries (DAF) expanded its drying research and development capacity through the purchase of a 2 m^3 research vacuum kiln to investigate the viability of vacuum drying technology for drying Australian hardwood species. Initial kiln trials drying native forest spotted gum (*Corymbia citriodora*) and young plantation Gympie messmate (*Eucalyptus cloeziana*) proved that these species can be vacuum dried approximately 60% faster than conventional drying, within acceptable grade quality limits [5].

The results obtained from these preliminary vacuum drying trials created much interest from the Australian hardwood timber industry. Forest and Wood Products Australia (FWPA – federal funding body for forestry research) in conjunction with various industry partners, and DAF, invested in a three-year project to establish the viability of vacuum drying technology for drying four high commercial volume Australian hardwood species, in terms of quality, time and cost. As 'trial and error' based drying optimisation research, using classical techniques to run a series of iterative drying trials, is so time consuming and expensive, a component of the project was to develop a mathematical model to simulate the heat and mass transfer characteristics for vacuum drying Australian eucalypts, and to use this data to develop a 'finite element' stress model to understand the various types and causes of stress related degrade. In particular, the predominantly observed degrade types; board end splitting and board surface splitting (also known as checking) was investigated.

In the past, substantial modelling work has been conducted for softwood species due to its commercial importance and relative homogeneity between species [6-9]. The increased complexity of the wood structure of hardwoods together with the huge variation within and between species, have resulted in limited deterministic modelling work using these species. Moreover, hardwoods often display complex mechanical and physical behaviour leading to specific forms of degrade phenomena such as cell collapse and internal checking (splitting), which are rarely a problem when drying softwoods.

Some native Australian hardwood species such as spotted gum (*Corymbia citriodora*) and Sydney blue gum (*Eucalyptus saligna*) can be easily dried whereas other species such as messmate (*Eucalyptus obliqua*) and mountain ash (*Eucalyptus regnans*) are considered to be some of the most difficult to dry in the world [10]. Much work has been conducted to identify the cause of severe drying degrade, however the methods used did not couple the entire mechanical and physical behaviour of the material as it relates to drying kiln conditions, such as temperature, air flow, humidity and atmospheric pressure [11-15]. The successful control of drying defects in a drying process, consists of maintaining a balance between the rate of evaporation of moisture from the surface and the rate of outward movement of moisture from the interior of the wood; i.e. controlling the MC gradient will in turn control the magnitude of drying stresses and subsequent susceptibility to stress related degrade.

One of the most accurate deterministic heat and mass transfer computational models identified from the review, originally developed for softwoods, is the *TransPore* model [7, 16]. The model encompasses multiscale and multiphysics descriptions of drying phenomena for a range of porous media such as wood and concrete [17, 18]. It is a deterministic model requiring a number of necessary input parameters to be measured for accurate input. Most of the modelling work described previously by other researchers cite and/or use aspects of this model in their work. It is a highly-regarded heat and mass transfer model and for this reason we chose it to adapt to a model for simulating the drying of Australian hardwoods.

The complexity of drying hardwoods, together with the huge variation within and between species, has resulted in limited modelling work being performed to date on these species. In particular, limited data are currently available for vacuum drying Australian hardwood species. This is detailed further in *section 1.2.3*.

This gap in the literature provides the motivation for the thesis research questions that underpin this work, which are formally stated as follows:

- Can the existing softwood drying model *TransPore* be adapted to produce a robust and precise heat and mass transfer, vacuum and conventional drying model, for a diverse range of Australian hardwood species?
- What are the necessary input parameters required to make the heat and mass transfer model a robust predictive tool and what are their order of sensitivity?
- Can the moisture content field simulation results be used to produce a finite-element-analysis (FEA) stress model that can predict stress-related drying degrade failure?

We recognised that to develop optimal models, collaboration to access different areas of expertise was required. This led to the following parties collaborating in this PhD work:

- Queensland University of Technology (QUT) for their mathematical modelling and visualisation expertise, and history of wood drying modelling development.
- Wood Science at Centrale Supelec, Université Paris-Saclay in Paris, France, and ENGREF and AgroParisTech in Nancy, France, for their expertise in wood drying modelling, instrumentation and wood property measurement.
- Queensland Cyber Infrastructure Foundation (QCIF) for their high-performance computing and model optimisation techniques.
- Griffith University (GU) for their expertise in finite element analysis of mechanical modelling.

Some of the wood property measurements, essential to develop an accurate model, required the use of specifically designed equipment only available in the ENGREF laboratory, Nancy, France. With the aid of funding from an FWPA Denis Cullity fellowship, the candidate travelled to the laboratory to perform the required tests. The results are reported by Redman [2]. For the modelling component, QCIF provided external funding to optimise the model convergence times and use of High Performance Computers (HPC). The results of which are reported by Redman [19].

The heat and mass transfer, and stress models developed are validated using data generated from a series of conventional and vacuum kiln drying trials using a selection of highly commercial Australian hardwood species. The trials were funded by FWPA and the resulting data is used widely in this thesis. The results of the trials are reported by Redman [20].

1.2 Literature review

Drying of native Australian hardwoods to satisfactory moisture levels with minimal degrade, cost and drying time is a challenging task. Australian eucalypt species are renowned for their difficult nature during drying. Not only is the drying considerably slower than other exotic hardwood species and most softwoods, eucalypts are particularly prone to drying induced degrade such as deformation, cell collapse, surface and internal splitting (checking) and residual drying stresses.

Drying is a complex operation combining intricate physical and mechanical processes that include external heat and mass flow, coupled heat and mass transfer within wood, shrinkage induced stress deformation, and the mechanical memory behaviour of wood. Limited validation of existing drying models and formulation of new drying models exist for Australian hardwood species. The following review describes the hardwood structure, previous research to measure wood properties essential to the heat and mass transfer model, the fundamental principles and limitations of the *TransPore* model chosen for adaptation for this research, together with previous modelling work used for Australian hardwood species. The review also describes previous research relating to stress/strain modelling of wood drying, particularly research relating to stress related degrade and methods to quantify failure criteria.

1.2.1 Wood structure

Before approaching the concepts governing the rheological and morphological behaviour of wood, it is necessary to have an understanding of wood structure as it relates to the movement of water within the physical and chemical structure. As the research is concerned only with Australian hardwood species (angiosperms), the information described in this section covers only hardwood structure. The following information was obtained and summarised from Siau [21], Ressel [22], Bootle [23] and Butterfield and Meylan [24].

Physical Structure

The physical structure of wood is inhomogeneous by nature. This is reflected in timber properties such as density, MC and its general physical appearance.

Tree growth takes place through the division of cells just underneath the bark and is known as the cambium layer. The cambium layer forms new sapwood or xylem on the inside of the cambium and new inner bark or phloem on the outside. A new sapwood cell is laid down at a particular distance from the ground and retains that position for the life of the tree, therefore inner bark cells are formed outward from the tree centre as the tree grows.

The sapwood is the newly formed wood that surrounds the heartwood. It is composed of living cells whose function is to conduct water and minerals from the roots to the leaves. The sapwood is usually lighter in colour than the heartwood. The inner sapwood gradually hardens and turns into heartwood as the tree grows.

The heartwood is the fully matured part of the tree. The transition to heartwood is marked by the deposition of extractives and other extraneous material in the cells, and in the case of most eucalypt species, by the accelerated production of tyloses. Tyloses are cellular membranes that enter vessels from adjacent parenchyma cells through pit pairs and greatly increase the resistance of water flow through the heartwood. The death of the living cells then follows so that the heartwood is physiologically dead tissue, which provides stability to support the tree.

Cell Structure

The basic cell structure of hardwoods consists of three cell formations produced on the inside of the cambium layer (xylem). These are the parenchyma cell (axial and ray), fibre and the vessel. Figure 1.1 shows a typical hardwood block magnified to 250 times with the various cell orientations and relative sizes shown. The LRT key represents the directions of the longitudinal, radial and tangential directions respectively.

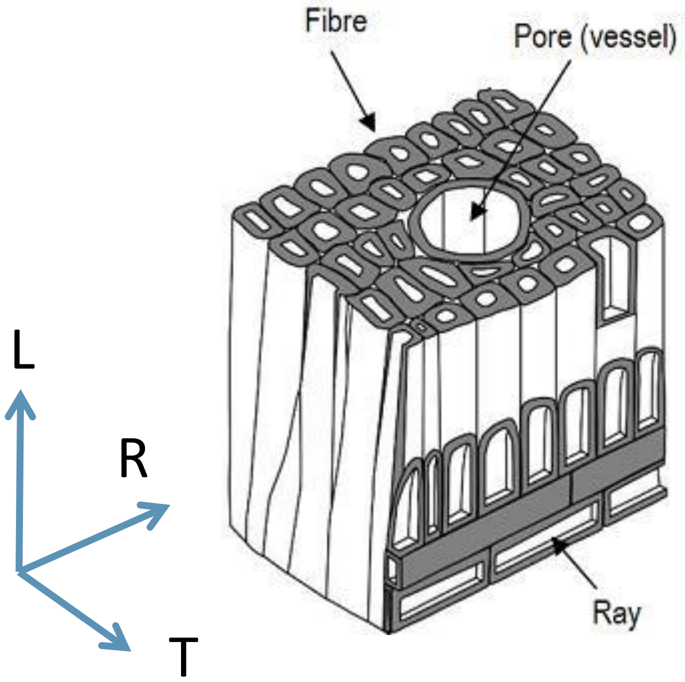

Figure 1.1 Diagram of a hardwood cube (magnification × 250), cell pits have been omitted. Diagram extracted from Butterfield and Meylan [24].

Fibres

Fibres make up the bulk volume of most hardwoods. Their primary role is to provide mechanical support for the tree. The proportion of fibres present, fibre diameter, and the average thickness of their cell walls largely govern the density of a hardwood. Fibres overlap longitudinally and the lumens of adjacent fibres are connected by pits. Although pits are present in fibres of most hardwood species, they are filled or occluded with various extractives.

Vessels

Hardwoods are sometimes called *porous woods* because of the vessels or pores that are sometimes visible to the naked eye in clean cut transverse faces. The vessels perform the major water carrying functions in the living tree.

Parenchyma Cells

Parenchyma cells have thin walls with numerous pits and are generally brick shaped. They act as a form of storage tissue and are scattered in strands (called rays), patches or bands amongst the vessels and fibres.

1.2.2 Essential wood properties required for heat and mass transfer modelling

Previous research [25, 26] has shown that a number of wood properties must be measured to provide the necessary structure for developing an accurate heat and mass transfer drying model. Other wood properties that govern the heat and mass transfer processes can be either inferred from essential wood properties or calculated via fundamental principles as discussed in *Appendix A*.

The following subsections provide details of the essential wood properties necessary for accurate heat and mass transfer modelling and, where appropriate a review of previous research is given.

Wood moisture content and basic density

Measurements of wood MC and basic density are fundamental physical properties that are made in accordance with Australian and New Zealand Standards. The standard method of test for wood MC is described in AS/NZS 1080.1:1997 Timber–Methods of test–Method 1: Moisture content [27], and for wood basic density is described in AS/NZS 1080.3:2000 Timber–Methods of Test–Method 3: Density [28]. Wood density is a function of the ratio of wood cell tissue to the cell cavities or lumens. Density varies between species, sapwood and heartwood. The basic density of the species used in this work ranged from 489 to 921 kg/m^3 [29]. The initial MC ranged from 32 to 85 % [30].

Wood porosity

Wood porosity is essentially a measure of the ratio of the wood cell lumen area to woody tissue in the transverse (radial/tangential) plane [3] in two dimensions. Wood porosity is generally determined using image analysis software on environmental scanning electron microscope scans in the transverse direction. The porosity range of the species investigated in this work ranged from 7 to 37 %.

Gas permeability

Permeability is the material property that indicates how freely fluids flow in response to an imposed pressure gradient. Permeability of wood to liquids and gases plays an important role in a number of technical processes such as wood treatment with preservative chemicals, the pulping process and wood drying. The more permeable the wood the more easily it can be processed or treated. Drying time and conditions are driven by the permeability, making it a crucial factor for the resulting product quality [31].

Wood permeability in hardwoods is affected mainly by anatomical features such as vessel size and obstructions (tyloses), pit aspiration, and the presence of extractives in heartwood [32]. For Australian hardwood species, as previous researchers suggest [33, 34], water movement during conventional drying is restricted predominantly to diffusion, mostly due to blocked wood-cell pits and extractives restricting the pathways for the movement of liquid water.

Gas permeability is often calculated using Darcy's law [35]:

$$K = \frac{Q\mu e P}{A\Delta P\overline{P}}, \qquad (1\text{-}23)$$

where K is the intrinsic permeability (m^2); Q is the air flux (m^2 s^{-1}); μ is the dynamic viscosity of air (Pa s); e is the sample thickness (m); P is the pressure at which flux Q is measured (Pa); A is the sample area (m^2); $\Delta P = P_2 - P_1$ is the pressure difference between the air outlet (P_2) and inlet (P_1) sides of the sample (Pa); $\overline{P} = \frac{(P_1+P_2)}{2}$ is the averaged pressure inside the sample (Pa).

Fluid migration in wood uses the vascular system developed by trees for physiological requirements. Therefore, wood has a number of specific features concerning permeability. Perré [36] suggests the two most important features are that:

- wood has dramatic anisotropy ratios: permeability can be 1000 times greater in the longitudinal direction than in the transverse direction for softwoods and this factor can be more than 10^6 for hardwoods,
- heartwood is usually much less permeable than sapwood: pit aspiration, tyloses development or extractives accumulation, are

responsible for this difference.

Table 1.1 summarises experimentally obtained directional gas permeability values sourced from the literature for different species. Depending on the experimental setup used by the authors, some data is missing. This data illustrates the huge variability in permeability between species as well as the dramatic anisotropy within a species.

Table 1.1 Experimentally obtained permeability values by unsteady and steady-state methods

Species	Notes	Permeability (m^2)			Anisotropy ratio			Authors
		L-10^{-12}	R-10^{-16}	T-10^{-16}	K_L/K_R	K_L/K_T	K_R/K_T	
Populus sp.	S l a	0.59	---	0.44	---	13 000	---	[37]
Populus sp	H l a	0.61	0.15	0.18	40 000	33 000	0.835	
Alnus rubra	S l a	1.9	0.15	0.12	125 000	166 000	1.327	
Liquidamber sp.	S l a	2.7	0.19	0.69	145 000	39 000	0.237	
Liriodendron sp.	H l a	5.4	---	0.80	---	67 000	---	
Sequoia sp.	S l a	4.9	11.2	19.4	4 000	2 000	0.580	
Sequoia sp.	H l a	0.25	0.112	0.88	23 000	3 000	0.127	
Pseudotsuga sp.	H l a	0.026	---	---	---	---	---	
Pseudotsuga sp.	S l a	0.049	---	0.37	---	1 300	---	
Pinus sp.	H l a	0.0026	---	0.17	---	153	---	
Acer rubrum	S g o	10.3	---	---	8 300	11 400	1.4	[38]
Acer rubrum	H g o	7.4	---	---				
Liriodendron sp.	S g o	28.9	---	---	1 450	1 600	1.1	
Liriodendron sp.	H g o	1.87	---	---				
Liquidamber sp.	S g o	13.9	---	---	13 00	2 750	2.1	
Liquidamber sp.	H g o	15.3	---	---				
Quercus rubra	S g	62	---	---	13 000	18 000	1.4	
Quercus rubra	H g	56	---	---				
Quercus falcata	S g	69	---	---	110 000	143 000	1.3	
Quercus falcata	Hg	13	---	---				
Liriodendron sp.	S l	26	4.5	---	57 000	---	---	[39]
Liriodendron sp.	H l	0.1	---	---	---	---	---	
Juglans nigra	S l	27	0.08	---	3 x 10^6	---	---	
Juglans nigra	H l	0.0052	---	---	---	---	---	
Quercus rubra	S l	61	0.68	---	900 000	---	---	
Quercus rubra	H l	45	---	---	---	---	---	
Picea sp.	g a	0.02	0.03	---	6 600	---	---	[40]
Pinus silvestris	g a	0.07	0.42	---	1 600	---	---	
Pinus pinaster	g a	0.15	8.6	---	170	---	---	
Picea sp.	S g a	0.2	---	---	700	---	---	[41],[42]
Fagus silvatica	S g a	3.8	---	---	3 000	65 000	21	
Fagus silvatica	H g a	1.4	---	---	3 000	---	---	
Populus sp.	H g a	0.03	---	---	10 000	---	---	
Tsuga heterophylla	S l o	0.20	0.554	0.689	3600	2900	0.804	[43]
Tsuga heterophylla	H l o	0.021	0.293	0.379	700	550	0.773	
Thuja plicata	S l o	0.1108	---	---	---	---	---	
Thuja plicata	H l o	0.0154	0.272	0.434	550	350	0.627	
Pinus taeda	S g a	9.5	2000	730	47	130	2.7	[32]

where S = sapwood, H = heartwood, g = permeability to gas, l = permeability to liquid, a = air dried sample and o = oven dried sample.

Bound water diffusion

Diffusion of water in wood refers to the molecular movement of bound water through the total wood system by a combination of transfer through cell wall mass and lumen void volume from a high water concentration area to a low area [44]. This process is a result of random molecular motions. Avramidis [44] suggests the understanding of the diffusion process can greatly improve our comprehension of the drying process, allowing researchers to develop drying schedules and decision support systems with the help of new robust models to improve the drying quality of timbers.

The first to recognize that the transfer of heat by conduction was also due to random molecular motions, in analogy with the diffusion process, was Fick in 1855 [45]. Diffusion into, or from, a medium with dynamic boundary conditions is expressed by Fick's second law, also called the unsteady-state law, which is given in differential form as follows:

$$\frac{\partial c}{\partial t} = \frac{\partial}{\partial x}\left(D\,\frac{\partial c}{\partial x}\right). \tag{1-24}$$

The diffusion coefficient can be either a constant, or can depend on concentration, pressure, temperature, and the composition of the medium.

There are two commonly accepted ways of measuring the bound water diffusion coefficient in wood, namely, the steady-state and unsteady-state methods [46]. The steady-state method involves using a diffusion cup and a thin wood specimen placed tightly (well sealed) at the top of the cup. The cup is partially filled with distilled water and a saturated salt solution to provide a constant relative humidity with constant temperature. The cup and attached specimen is placed in a conditioning chamber where the ambient temperature and relative humidity are accurately controlled.

Depending on the external/internal cup relative humidity, the assembly will either lose or gain weight. By plotting the change of weight loss/gain of the device with time, the diffusion coefficient can be determined.

The unsteady-state method involves the placement of thin wood samples in a controlled environment chamber under constant temperature and relative humidity, until they reach equilibrium with the surrounding conditions. Specimens are then placed in another environment with differing relative humidity conditions and are weighed periodically. The diffusion coefficient can again be determined by plotting the weight gain/loss with time.

It should be noted that the diffusion coefficient calculated by both methods does not always coincide numerically. At lower MCs they are quite similar, but at high MCs the steady-state diffusivity values can be up to double the unsteady-state ones due to stress relaxation phenomena in the latter case [44].

Table 1.2 summarises experimentally measured diffusion coefficient values sourced from the literature using the unsteady and steady-state methods. The material direction (L, R and T) is shown for each species tested as well as measurements on sapwood (S) and heartwood (H). Values otherwise stated were performed on heartwood material. By observation of the table results, it can be concluded that material direction and material type affects the coefficient of diffusion for individual species.

Table 1.2 Experimentally obtained diffusion coefficient values by unsteady and steady-state methods

MC range (%)	Temp. Range (ºC)	Species	D (m^2/s)	State	Reference
14-7	35	*P. sylvestris* (R)	1.5E-10	Unsteady	[47]
		P. sylvestris (T)	1.4E-10		
		P. sylvestris (L)	24.0E-10		
		F. sylvatica (R)	2.4E-10		
		F. sylvatica (T)	0.5E-10		
		F. sylvatica (L)	30.0E-10		
Green-6	50	*T. heterophyla* (S-R)	1.7 – 0.4E-10	Unsteady	[43]
		T. heterophyla (H-R)	1.1 – 0.4 E-10		
		T. plicata (S-R)	0.9 – 0.4E-10		
		T. plicata (H-R)	1.6 – 0.5E-10		
Green–7.5	60	*A. lasiocarpa* (R)	0.9E-10	Unsteady	[48]
Green–7.5		*A. lasiocarpa* (L)	8.5E-10		
23–7.5		*A. lasiocarpa* (R)	0.6E-10		
23–7.5		*A. lasiocarpa* (L)	6.7E-10		
7-14	35	*P. sylvestris* (R)	4.2E-10	Unsteady	[49]
		P. sylvestris (T)	2.8E-10		
		P. sylvestris (L)	18.6E-10		
		F. sylvatica (R)	1.8E-10		
		F. sylvatica (L)	0.94E-10		
		F. sylvatica (T)	19.4E-10		
14-10	25	*B. serrata* (R)	1.9E-10	Steady	[50]
		C. apetalum (R)	1.7E-10		
		E. delegatensis (R)	1.8E-10		
		F. brayleyana (R)	1.1E-10		
Green-0	30-40	*T. superb* (R)	0.1–0.5E-10	Steady	[51]
		T. superb (T)	0.1-0.3E-10		
		T. superb (L)	0.3-0.7E-10		

Shrinkage

To appreciate the fundamental phenomena of drying induced shrinkage and associated stress it is necessary to understand the relationship of each to the removal of water from wood. Green wood contains free water in the cell lumens and bound water in the cell wall. During drying, free water is generally removed before bound water. When the cell's lumens are empty of free water but all bound water remains, the wood is said to be at the fibre saturation point (FSP). The FSP is expressed as a percentage of MC. Normal shrinkage occurs at MCs below FSP in all timbers due to the removal of bound water from cell walls. Conversely, swelling occurs at MCs up to FSP when adsorption takes place. The phenomena of shrinkage and swelling differ according to the material direction because of the strong anisotropy of wood.

The shrinkage of wood during drying is one of the most important properties as it is responsible for deformations during drying (twist, spring, bow and cupping), dimensional variations in situ, and is the driving force for stress. In turn, stress is responsible for most drying related defects including surface and internal checking, end splitting, case hardening, and residual drying stress.

During wood drying, shrinkage starts once the outside layer reaches FSP (Figure 1.2a). The core of the timber is still above fibre saturation point and consequently will not shrink. This creates a stress gradient within the timber, as the shrinking surface fibres go into tension, and the core, which is restraining the shrinkage, goes into compression (Figure 1.2b). This sets up a shrinkage/stress gradient between the inner core of the timber and the outer shell. If the tensile force on the outer shell exceeds the modulus of rupture (MOR), the surface of the board will split or check (Figure 1.3). Once the core of the timber dries below fibre saturation point the stresses in the timber reverse, with the shell now restraining the core as it tries to shrink. The core then goes into tension and the shell into compression [52]. This effect can cause internal checking. Additionally, differential shrinkage caused by differences in radial, tangential, and longitudinal shrinkage is a major cause of distortion of timber during drying.

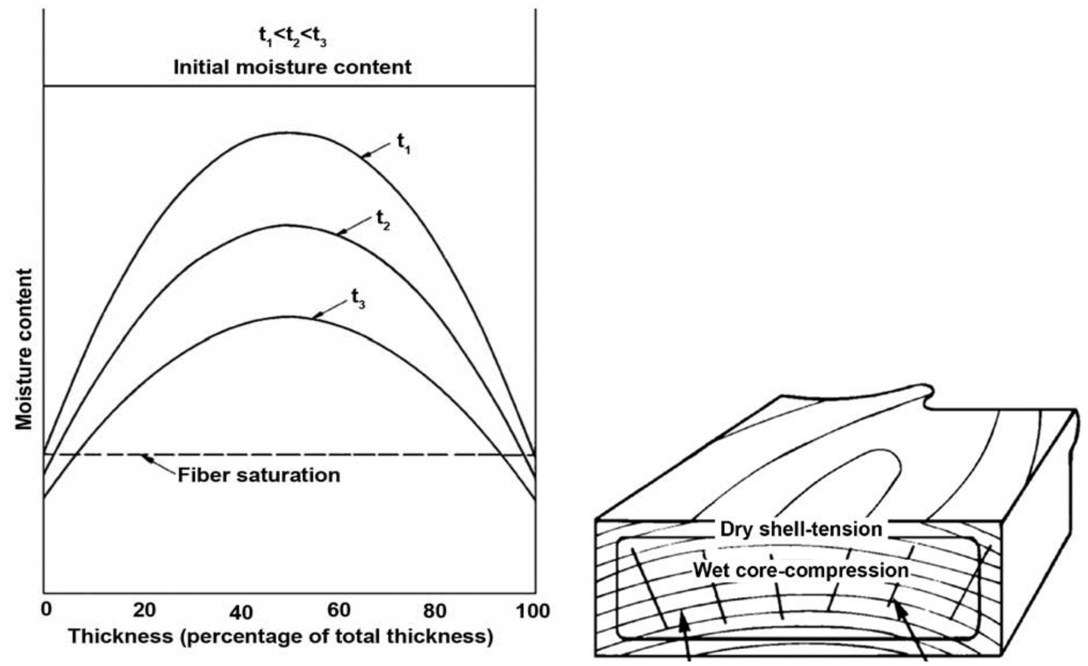

(a) (b)

Figure 1.2 Moisture gradient set up during drying through the thickness of a board (a) and the subsequent stress gradient that causes surface tension (b). Diagrams extracted from AFRDI [53].

(a) (b)

Figure 1.3 Examples of end split (a) and surface checking (b) stress-induced drying-degrade

Sorption isotherms

The sorption hysteresis effect, i.e. different wood equilibrium moisture content (EMCs) in desorption and adsorption for the same relative humidity, is well known. However, quantitative sorption isotherms in the form of tables or analytical correlations, are usually given as the average of the desorption and adsorption curves. Consequently, most drying simulation models use these average curves, and do not take into account the sorption hysteresis phenomenon [54].

Salin [54] proposes that traditional models that use average sorption curves (derived across a range of species) are problematic because different species have different sorption isotherms. Therefore, species-specific sorption isotherms, including the sorption hysteresis phenomenon, of which drying models are very sensitive, should be included in drying models as an improved tool in practical applications.

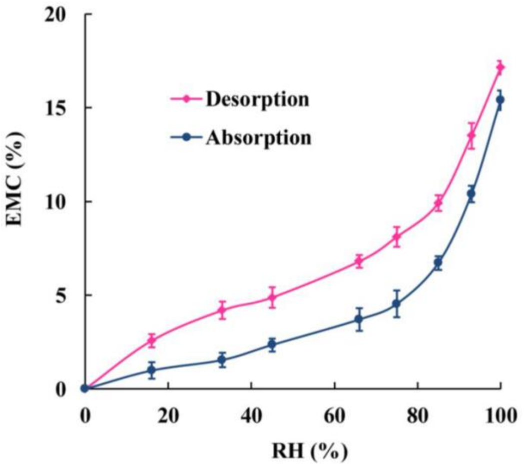

Figure 1.4 Example of a typical desorption and adsorption isotherms for Southern yellow pine. Diagram extracted from Lui et al. [55].

A summary of the measured and formulated wood properties used for the *TransPore* model are provided in *Appendix A*.

1.2.3 An overview of previous modelling of Australian hardwoods

As mentioned earlier, limited modelling work has been performed on drying of Australian hardwood species with most wood drying models focussed on softwood species. The following is a review of previous modelling work, particularly relating to heat and mass transfer and stress/strain modelling, performed on Australian hardwoods and the subsequent outcomes.

Schaffner [56] developed a model in the 80's for hardwood drying based on Fick's Law of diffusion, which focused on a computer model that predicted the stresses in hardwood timber during drying. Emeritus Professor Arch Oliver built on Schaffner's work to write a program called DRYWOOD from which *KilnSched* (Kiln Scheduling Program) was subsequently developed [57]. KilnSched is based on a nonlinear stress and drying model. As a result of a three-year collaborative grant, a kiln controller (the Clever Kiln Controller, or CKC) was developed. The CKC is an online modelling and acoustic emission (AE) monitoring program [58].

KilnSched models one-dimensional flow of heat and mass transfer from the board centre to the board surface. Wu [59] determined that a Fick's law based formula adequately described the drying of Tasmanian eucalypts. *KilnSched* employs a single reference diffusion coefficient dependent on temperature, but independent of MC. *KilnSched* also utilises a nonlinear stress-strain curve based on numerous laboratory compression and bending tests [57]. In the model, the directly measurable net strain is given as the sum of the unconfined shrinkage strain, instantaneous strain, creep strain and the mechano-sorptive strain.

KilnSched allows the operator to develop a low drying-degrade schedule during the early stages of drying, when limited material properties have been obtained. These material properties are basic density, fibre saturation point, equilibrium MC, unconfined shrinkage at fibre saturation point, unconfined shrinkage at equilibrium MC, diffusion coefficient, rack stick spacing, board width, board thickness, control strain and collapse threshold temperature [33]. The diffusion coefficient is measured by taking periodical slicings to determine moisture gradients during the early stages of drying. These gradients are then fitted to modelled data to determine the diffusion coefficient. The primary constraints of this model are collapse threshold temperature (the minimum temperature at which collapse degrade occurs) and maximum allowable surface strain.

Wu [59] performed a detailed investigation of the airflow through a timber stack, primarily to study the structure and development of the boundary layer. Measurements of surface shear stress, friction factor and the mechano-sorptive effect were investigated and incorporated into *KilnSched*.

SMARTKILN [60] is a program based on *KilnSched*, which generates a continuously varying schedule that maximises drying rate, whilst holding the surface instantaneous strain at a level below the theoretical onset of surface checking.

To date, the CKC program has been tested successfully on old growth Tasmanian eucalypt material and is yet to be successful in modelling ‘hard to dry’ regrowth and collapse prone materials due to the lower than ambient collapse threshold temperatures of these timbers [61].

Brooke [62] used a one-dimensional Fickian drying model combined with a one-dimensional shrinkage and elastic stress model to optimise timber drying schedules. The model was tested initially on ironbark (*Eucalyptus* *paniculata*) and produced a new drying schedule 10% faster than for the industry standard schedule, and reduced the surface checking by 75% [62]. The model was also used to create optimal schedules for New South Wales spotted gum (*Corymbia maculata*) and yellow stringybark (*Eucalyptus muellerana*). This resulted in reduced drying times, from the original drying time, of 40% and 15%, respectively. The checking in spotted gum was decreased by 50%, but the checking in yellow stringybark was increased by 130%.

Although, these previous models produced accurate simulations, they either 1) inferred input parameters from published data or were 2) specific to only a narrow species band. After an extensive review of heat and mass transfer models (refer section 1.1) the *TransPore* model was chosen for this work based in its greater adaptability to a wide range of porous media and international recognition by other researchers.

1.2.4 History of the *TransPore* heat and mass transfer model

Wood is a complicated hygroscopic cellular porous material within which moisture may coexist in different states including: free water in cell cavities (lumens); bound water that is hygroscopically held by the cell walls; water vapour in the voids or lumens of the cells; or constitutive water in the chemical composition within the cell walls. During drying, only the free, bound and vapour phases of the water are removed. The basic moisture migration mechanisms are liquid flow due to capillary and/or internal gaseous pressure gradient, diffusing water vapour, vapour convection in bulk gas flow and bound liquid diffusion. The difficulties involved in the modelling of timber drying are highlighted by the facts that wood is heterogeneous, hygroscopic, strongly anisotropic (with the ratio between longitudinal and transverse permeability being in the range of 10^2 to 10^4) and shrinks during drying with dimension changes causing internal stresses to occur [63].

Early modelling presented by past researchers [57, 59, 64-68] utilised one-dimensional drying models to assist with the understanding of the physics associated with the overall drying process. Subsequent advancements in computer technology have made it possible to extend the existing one-dimensional model to comprehensive and numerically efficient two-dimensional [7, 63, 69] and three-dimensional models [16, 70]. Multidimensional models are able to more closely represent reality and can be used to study the effects that the anisotropy of the wood can have on the drying process. For instance, stresses that develop during drying depend strongly on the board width, while the longitudinal direction is important to represent transport phenomena.

High-temperature drying and/or microwave, radiofrequency and vacuum drying induce an over-pressure within the board that increases the level of longitudinal transport compared with conventional drying methods. Perré and Turner [16] suggest that a three-dimensional model is absolutely necessary before a comprehensive vacuum and/or microwave drying simulation can be performed. However, three-dimensional modelling may not be necessary for Australian eucalypt species as previous researchers suggest mass flow during conventional drying of these species is restricted predominantly to the transverse (T and R) directions via diffusion [33, 34]. As far as this author is aware, this theory has not been tested previously for the vacuum drying of Australian hardwoods.

Due to its accuracy, robustness and adaptability, the previously discussed *TransPore* model, developed by Perré and Turner [7] was chosen for this work. We note here that recent enhancements of *TransPore* developed by Carr *et al*. include novel computational strategies to increase the accuracy and efficiency of the model. These enhancements include variable-stepsize Jacobian-free exponential time stepping [71] and a dual-scale modelling approach [72].

1.2.5 Modelling heat and mass transfer under vacuum drying

During drying, transport phenomena occur within the porous medium and at its surface. Due to the anatomy of wood and the existence of water transferring simultaneously in the solid, liquid, gaseous and bound water phases, different drying periods must be realised and modelled based on the drying mechanism used and the magnitude of MC within the wood. For low temperature (< 100 °C) convective drying, the role of internal gaseous pressure is almost negligible and transfer occurs mainly in the direction of the board thickness, whereby two drying periods exist [26].

The first is the constant drying rate period. During this period, the surface of the board remains above the fibre saturation point (FSP). As a result, the vapour pressure at the surface equals the saturated vapour pressure, and only depends on the surface temperature. During this stage, heat and vapour transfer occur in the boundary layer, where the drying rate is constant and depends only on the external psychrometric conditions. As the main energy transfer occurs within the medium during this period, the temperature of the board remains at the wet bulb temperature. The board surface is supplied with liquid water from within via capillary action. The constant rate drying period lasts as long as liquid is evident at the surface. The liquid flow inside the medium is expressed by Darcy's law. During this period, a MC gradient steepens as drying progresses and continues until the liquid flow directed towards the surface ceases, which indicates the commencement of the second drying rate period.

Once the surface becomes hygroscopic (where the MC is below the FSP), the vapour pressure exceeds the saturated vapour pressure. Subsequently, the external vapour flux is reduced and the heat flux applied to the medium is temporarily greater than what is necessary for liquid evaporation. The excess energy is used to heat the board, initially at the surface and then internally by conduction. The external vapour flow now depends on both temperature and MC. An inner zone develops within the wood where liquid migration prevails along with a surface zone where both bound water and water vapour diffusion occur. During this period, a conductive heat flux exists inside the board to increase the temperature and evaporate the liquid driven by gaseous diffusion.

For high-temperature and reduced pressure (vacuum) drying above the boiling point of water, an over-pressure is established within the wood implying that a pressure gradient drives the moisture (liquid and/or vapour) towards the boundary. When an over-pressure exists inside the board the effect of the pressure gradient on gaseous or liquid migration takes place in the longitudinal direction. This is a result of the anisotropic anatomical features of wood [26]. Although this phenomenon has been shown to occur in many softwoods, it may not hold true for highly impermeable hardwood species due to differing anatomical features.

1.2.6 Description of the *TransPore* model

As the anatomical configuration of wood is complex, one must write transport equations at the macroscopic scale. This leads to the definition of empirical laws of migration that can be demonstrated to a large extent by averaging over representative volumes [3]. By using this approach, we can write most fluxes as the product of an effective coefficient multiplied by the relevant driving force. The conservation of liquid, water vapour, air and enthalpy enable a set of equations governing transfer in porous media to be derived [73].

The most recent application of the model, and the one used in this research, describes the drying of single softwood boards [74]. This model, known as *TransPore 2D* describes the drying process in two-dimensions. That is in either the radial-tangential (R-T), radial-longitudinal (R-L) of tangential-longitudinal (T-L) planes. In the following sections, we outline the drying equations, the conditions that are assumed on the external surface of the board and the constitutive relationships required to close the model. A detailed description of the measured wood property values, formulated physical properties and symbol nomenclature are provided in Appendix A.

Liquid conservation is described by:

$$\frac{\partial}{\partial t}\left(\varepsilon_w\rho_w + \varepsilon_g\rho_v + \overline{\rho}_b\right) + \nabla\cdot\left(\rho_w\overline{\boldsymbol{v}}_w + \rho_v\overline{\mathbf{v}}_g + \overline{\rho_b\mathbf{v}_b}\right) \qquad (1\text{-}1)$$
$$= \nabla\cdot(\rho_g\overline{\overline{\boldsymbol{D}}}_{eff}\nabla\omega_v)$$

energy conservation by:

$$\begin{gathered}\frac{\partial}{\partial t}(\varepsilon_w\rho_w h_w + \varepsilon_g(\rho_v h_v + \rho_a h_a) + \overline{\rho}_b\overline{h}_b + \rho_s h_s - \varepsilon_g P_g)\\ +\nabla\cdot(\rho_w h_w\overline{\mathbf{v}}_w + (\rho_v h_v + \rho_a h_a)\overline{\mathbf{v}}_g + h_b\overline{\rho_b\mathbf{v}_b}) \qquad (1\text{-}2)\\ = \nabla\cdot\left(\rho_g\overline{\overline{\boldsymbol{D}}}_{eff}(h_v\nabla\omega_v + h_a\nabla\omega_a) + \boldsymbol{\lambda}_{eff}\nabla T\right)\end{gathered}$$

and, air conservation by:

$$\frac{\partial}{\partial t}\left(\varepsilon_g\rho_a\right) + \nabla\cdot\left(\rho_a\overline{\mathbf{v}}_g\right) = \nabla\cdot\left(\rho_g\overline{\overline{\boldsymbol{D}}}_{eff}\nabla\omega_a\right). \qquad (1\text{-}3)$$

The gas and liquid phase velocities are given by the Generalised Darcy's Law:

$$\overline{\mathbf{v}}_l = -\frac{\overline{\overline{K}}_l\overline{\overline{k}}_l}{\mu_l}\nabla P_l \tag{1-4}$$

where $l = w, g$.

This formulation accounts for the evolution of internal pressure through the air balance equation (1-3) and is thus able to deal with high temperature convective drying and vacuum drying.

Closure conditions

Wood is a highly hygroscopic porous medium, therefore bound water (b) must be separated from free water (w) as defined by:

$$\mathcal{X} = \mathcal{X}_w + \mathcal{X}_b \equiv \frac{\varepsilon_w \rho_w}{\rho_o} + \min\left(\mathcal{X}_{fsp}, \mathcal{X}\right), \tag{1-5}$$

Where $\mathcal{X}$ represents the moisture content. The volume fractions of the liquid and gaseous phases are defined as: $\varepsilon_w = \phi S_w$,$\varepsilon_g = \phi(1 - S_w)$,$\varepsilon_w + \varepsilon_g = \phi$, where ϕ is the porosity. The average air density is defined as $\overline{\rho}_a = \varepsilon_g \rho_a$ and the gaseous phase is a mixture of air and vapour, which is assumed to behave like an ideal gas. The saturation variable involved in the relative permeability functions is calculated according to the free water content only:

$$S_w = \frac{X_w}{X_{w\max}}. \tag{1-6}$$

Both liquid and gaseous water phases are present during the drying of wood. As a result of the curvature of the interface that exists between the liquid and gas phases within the wood pores, the liquid pressure is less than the gas pressure. The difference is represented by the capillary pressure:

$$P_w = P_g - P_c. \tag{1-7}$$

The values for fibre saturation point (X_{fsp}) is one of the essential wood properties necessary for the development of an accurate wood drying model. The measurement of fibre saturation point is detailed by Redman *et al.* [30] and Redman *et al.* [75] by observing the shrinkage behaviour of thin wood sections during desorption.

Initial and boundary conditions

The boundary conditions for the external drying surfaces are assumed to be of the following form [69]:

$$\mathbf{J}_w \cdot \hat{\mathbf{n}} = k_m c M_v \ln\left(\frac{1-x_\infty}{1-x_v}\right) \tag{1-8}$$

$$\mathbf{J}_e \cdot \hat{\mathbf{n}} = q(T - T_\infty) + h_v k_m c M_v \ln\left(\frac{1-x_\infty}{1-x_v}\right) \tag{1-9}$$

$$P_g = P_\infty, \tag{1-10}$$

where $\mathbf{J}_w$ and $\mathbf{J}_e$ represent the fluxes of total moisture and total enthalpy at the boundary, respectively; x_∞ and x_v represent the molar fraction of gas vapour in the kiln at the exchange surface, respectively. The pressure P_∞ and temperature T_∞ at the external drying surfaces are fixed at the kiln vacuum pressure and operating temperature. As one of the primary variables used for the computations is the average air density, the boundary pressure condition (1-10) is modified to form an appropriate nonlinear equation using the ideal gas law:

$$\varepsilon_g(P_v - P_\infty) + \frac{\overline{\rho}_a RT}{M_a} = 0. \tag{1-11}$$

Initially the board has some prescribed MC, with the pressure and temperature fixed throughout the board at the initial kiln pressure and temperature respectively.

The values for external pressure, temperature and air velocity, measured from the vacuum trials data, were used as model boundary condition input data, enabling the development of an accurate deterministic wood drying model. The parameters were measured as detailed by Redman [29] and used in this study.

As the kiln pressure, temperature, humidity and air velocity was measured at discrete time intervals, and a continuous input function for each parameter was required for the model boundary condition input data, the discrete data was fitted to a continuous sigmoid function using *TableCurve2D*[2] software. A sigmoid function is a mathematical function having an "S" shape (sigmoid curve). It is used in modelling systems that transition from one value to another and plateau at large values of time t [76]. In general, a sigmoid function is real-valued and differentiable; having either a non-negative or non-positive first derivative which is bell shaped. There is also a pair of horizontal asymptotes which provide the lowest and the highest Y values when X tends to infinity. In our case this is a convenient way to model the kiln parameters as they tend to increase or decrease to a final asymptotic value with time. Another advantage with this function is that if the model can be run at times greater than experimentally recorded times the parameter values remain stable.
The form of the sigmoid fitting function is:

$$y = a + \frac{b}{1+exp^{-\frac{(x-c)}{d}}}, \tag{1-12}$$

where b is the transition height, c is the transition centre, a is the asymptote, the transition width is given by 2.19224578 × d where $d \neq 0$ [76].

An example of the output of *TableCurve2D* sigmoid function curve fitting for kiln temperature for the messmate species is provided in Figure 1.5.

---

[2] https://systatsoftware.com/

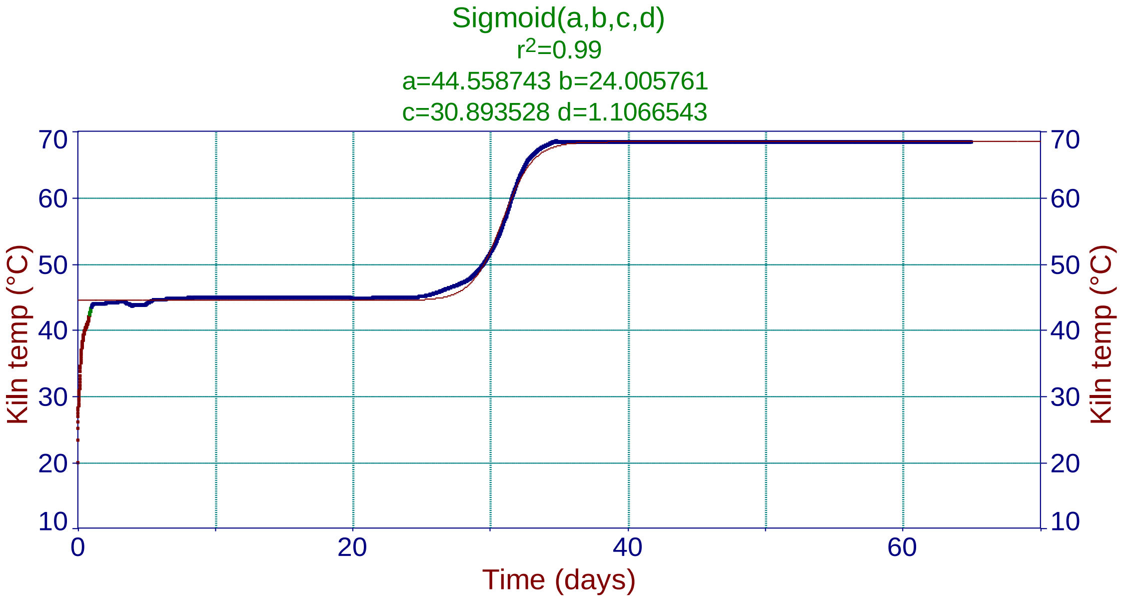

Figure 1.5 Sigmoid curve fitting example for messmate kiln drying temperature

Numerical solution procedure

The numerical procedure employed to resolve the drying model in this work has been extensively published, and the reader is referred to the most relevant literature for the finer details [7, 16, 71, 72]. A brief summary of the main components of the computational model are given here. Equation (1-11) must be resolved during the nonlinear iterations for every control volume within the computational domain. The finite volume method is implemented on a triangular mesh within a rectangular domain for the spatial discretisation of the conservation laws [71]. Meshes were generated over board transverse and longitudinal cross-sections. Thereafter, an efficient inexact Newton method is used to resolve in time the nonlinear system that describes the drying process. Upwinding is used as the spatial weighting scheme for all advection/convection terms in the equations and the introduction of the fixed phase ensures that full saturation $S_w = 1$ is never reached at the surface of the medium [77]. This enhances convergence of the model and ensures accurate resolution of the drying fronts on relatively coarse meshes that are evident during the vacuum drying process [69].

Control volume discretisation procedure

The following discretisation, upwinding and finite element interpolation procedures follow those described by Carr *et al*. [18].

To obtain a differential equation analogue of the theoretical drying model we use a Control Volume spatial discretisation procedure. For each element node, and using the underlying triangular mesh structure, control volumes are constructed by connecting the midpoints of each edge to the centroids of each element. Figure 1.6 depicts a typical internal control volume.

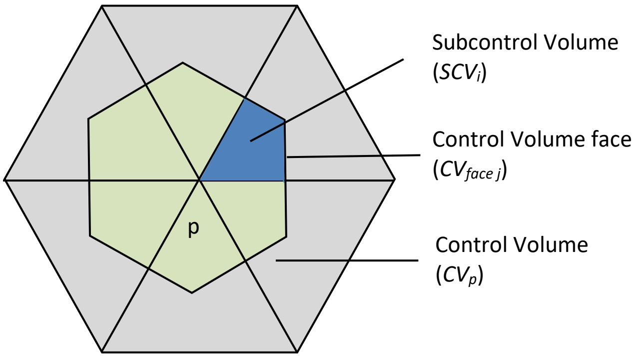

Figure 1.6 Control volume example for an internal node p

The discrete form of the equations are derived by noting that each of the conservation laws equations 1-1, 1-2 and 1-3 can be expressed in the following general conservative form:

$$\frac{d\overline{\psi}_l}{dt} + \frac{1}{V_{CV_p}} \sum_{j=1}^{NS_p} \int_{CV_{face_j}} (\boldsymbol{J_l} \cdot \boldsymbol{\hat{n}}) d\sigma = 0, \qquad (1\text{-}13)$$

where NS_p denotes the number of sub-sontrol volumes on the set $S_p$that share node p as a vertex, *l* = *w*, *e*, *a* and $\overline{\psi}_l$ is the averaged value of ψ_l over the control volume

$$\overline{\psi}_l = \frac{1}{V_{CV_p}} \int_{CV_p} \psi_l dV, \qquad (1\text{-}14)$$

$\hat{\boldsymbol{n}}$ is the outward unit normal and the surface integral (line integral) over the control volume boundary is expressed as the sum of the integrals at each of the faces. We follow the classical finite volume theory [18] by using a midpoint quadrature rule to approximate each integral. The averaged value $\overline{\psi}_l$ is approximated by the value of ψ_l at the node *p*, denoted by $\overline{\psi}_{l_p}$, to give:

$$\frac{d\psi_{l_p}}{dt} + \frac{1}{V_{CV_p}} \sum_{j=1}^{Nf_p} (\boldsymbol{J_l} \cdot \hat{\boldsymbol{n}})_{midCV_{face_j}} A_{CV_{face_j}} = 0, \qquad (1\text{-}15)$$

where the summation is taken over all control volume faces and $A_{CV_{face_j}}$ is the area (length) of the *j*^th^ face (edge) and the subscript $midCV_{face_j}$ denotes evaluation of the resolved flux in the direction of the normal at the midpoint of face *j*. Once each node is visited in the mesh, the spatially discrete analogue of the drying equations can be expressed as:

$$\frac{d}{dt}\begin{pmatrix} \psi_w \\ \psi_e \\ \psi_a \end{pmatrix} = -\frac{1}{V_{CV_p}} \sum_{j=1}^{Nf_p} \begin{pmatrix} \boldsymbol{J_w} \cdot \hat{\boldsymbol{n}} \\ \boldsymbol{J_e} \cdot \hat{\boldsymbol{n}} \\ \boldsymbol{J_a} \cdot \hat{\boldsymbol{n}} \end{pmatrix}_{midCV_{face_j}} A_{CV_{face_j}} = \boldsymbol{0}. \qquad (1\text{-}16)$$

For nodes situated on the boundary of the domain, $\boldsymbol{J_w} \cdot \hat{\boldsymbol{n}}$ and $\boldsymbol{J_e} \cdot \hat{\boldsymbol{n}}$ are replaced by equations (1-8) and (1-9) for control volume faces, in the discrete analogue of the water and energy conservation equations and the discrete analogue of the air equation is replaced by equation (1-10).

The spatially-discrete equations require the approximation of each of the flux terms: $\boldsymbol{J_w}$, $\boldsymbol{J_e}$ and $\boldsymbol{J_a}$. These have been approximated by using a combination of finite element interpolation strategies [78] and upwinding [79]. These strategies are explained for the air flux, $\boldsymbol{J_a}$ given by:

$$J_a = \rho_a v_g - \rho_g \overline{\overline{D}}_{eff} \nabla\omega_a = -\left(\frac{\rho_a \overline{\overline{K}}_g \overline{\overline{k}}_g}{\mu_g}\right) \nabla P_g - \rho_g \overline{\overline{\boldsymbol{D}}}_{eff} \nabla\omega_a \qquad (1\text{-}17)$$

with a similar description for the other two fluxes. To approximate J_a at the midpoint of a control volume face all gradients are approximated using interpolation (Figure 1.7). The remaining velocity and diffuse/convective terms are upwinded and interpolated respectively. The air flux, ρ_a and tensor components K_g^R, K_g^T, k_g^T and k_g^T are upwinded while ρ_g, ω_a, P_g and the tensor components D_{eff}^R and D_{eff}^T are approximated using interpolation.

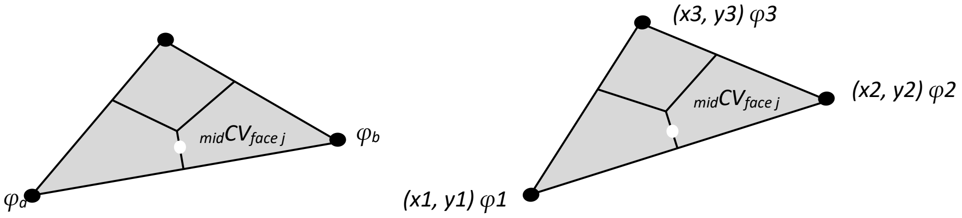

(a) upwinding (b) linear interpolation

Figure 1.7 Schematic depictions of an arbitrary triangular element denoting the upwinding and linear interpolation notation used.

Upwinding

Suppose the scalar quantity φ is to be approximated at the midpoint of the control volume face $midCV_{face_j}$ using upwinding (Figure 1.7a). This involves approximating the value of φ at the control volume boundary by either the value of φ at node a or node b based on the following:

If $\left(\boldsymbol{v}_g{}^{(n)} \cdot \boldsymbol{n}\right)_{midCV_{face_j}} < 0$ then $\varphi_{midCV_{face_j}}$ is approximated by φ_a
If $\left(\boldsymbol{v}_g{}^{(n)} \cdot n\right)_{midCV_{face_j}} > 0$ then $\varphi_{midCV_{face_j}}$ is approximated by φ_b,

where $\boldsymbol{v}_g{}^{(n)}$ is the gaseous phase velocity at time level n (previous time level).

Finite Element Interpolation

A linear profile is assumed over each element that are to be approximated using interpolation. To approximate a scalar variable, say φ over the element e (Figure 1.7b), the following interpolant is assumed over the element:

$$\varphi^{(e)}(x,y) = \alpha^{(e)}x + \beta^{(e)}y + \gamma^{(e)}, \tag{1-18}$$

which gives a constant gradient of $\nabla\varphi^{(e)} = \left(\alpha^{(e)}, \beta^{(e)}\right)^T$, across the element where $\alpha^{(e)}$, $\beta^{(e)}$ and $\gamma^{(e)}$ are chosen to ensure $\varphi(x_1, y_1) = \varphi_1$, $\varphi(x_2, y_2) = \varphi_2$ and $\varphi(x3, y3) = \varphi3$:

$$\alpha^{(e)} = \frac{1}{2A^{(e)}}\{\varphi_1(y_2 - y_3) + \varphi_2(y_3 - y_1) + \varphi_3(y_1 - y_2)\} \tag{1-19}$$

$$\beta^{(e)} = \frac{1}{2A^{(e)}}\{\varphi_1(x_3 - x_2) + \varphi_2\,(x_1 - x_3) + \varphi_3(x_2 - x_1)\} \tag{1-20}$$

$$\gamma^{(e)} = \frac{1}{2A^{(e)}}\{\varphi_1(x_2y_3 - x_3y_2) + \varphi_2(x_3y_1 - x_1y_3) + \varphi_3(x_1y_2 - x_2y_1)\} \tag{1-21}$$

and $A^{(e)}$ is the area of the element with

$$2A^{(e)} = x_1y_2 - x_2y_1 + x_2y_3 - y_2x_3 + x_3y_1 - x_1y_3. \tag{1-22}$$

To summarise, the value of the scalar variable, φ, at the midpoint of the control volume boundary, $\varphi_{midCV_{face_j}}$, is approximated by using equation (1-18) at the midpoint of the face. The gradient of $\nabla\varphi_{\left(midCV_{face_j}\right)}$ is approximated by $\left(\alpha^{(e)}, \beta^{(e)}\right)^T$.

1.2.7 Modelling drying stress

As stress during drying is the major influence on drying degrade, the understanding of stress formation behaviour is paramount to optimising wood drying to within acceptable degrade limits. Degrade limits are usually imposed by grade quality standards and acceptability is subject to customer requirements and the utilisation of wood material. For instance, the degrade limitations for wood for furniture are higher than for wood to produce pallets. Early work to characterise drying stresses involved destructively slicing samples during drying. The method was first reported by McMillen [52] and later used by other researchers [62, 80, 81] as a drying schedule development tool. Other methods to physically characterise drying stresses in real -time include the ‘flying wood’ technique developed by Brandao and Perré [82], using ‘force-measuring’ devices [83, 84] (load cells) and surface strain techniques [29, 85, 86]. The ‘flying wood’ test is based on non-symmetrical drying of wood samples (drying from one surface only) to characterise drying stress formation by measuring the curvature of the sample during drying. However, all of these methods are limited to laboratory testing and are not predictive tools, but rather investigative tests.

Since the work of McMillen [52], considerable research has been performed to develop predictive stress/strain drying models. Early work began in 1979 in Tasmania, Australia [87] by the Tasmanian Timber Promotion Board and the University of Tasmania who collaborated on a research project aimed at drying ‘backsawn’ Tasmanian oak species with minimal surface checking [88]. To slow down the drying rate, semi-impermeable coatings were trialled to develop a method of selecting a surface coating that would control moisture content gradients, and thus reduce surface checking. In parallel with this work, a number of physical wood properties were measured including diffusion coefficients, shrinkage behaviour, tensile and compressive failure stresses across the grain, and elastic moduli [56, 88]. A method to compute moisture gradients was also established using a one-dimensional model based on constant Fickian diffusion coefficients [89]. The use of constant diffusion coefficients was found to be a limiting factor for the model in terms of accuracy over a wide range of temperatures and moisture contents. More advanced models now use the full version of Fick’s Law that allows diffusion parameters to vary with temperature and moisture content.

Following this, the model was expanded to include a stress component with the ability to predict stress levels for different coatings, drying conditions and wood properties [56, 88]. The model was based on the theory of elasticity in anisotropic bodies, and assumed the wood to be linearly elastic and free of the effects of hysteresis and creep [87]. The governing equations used were airy stress functions that were solved by numerical methods.

The model was further refined by Oliver [90] who incorporated the effect of creep and mechano-sorptive stress. Creep describes the permanent deformation of wood over time when under load, while the mechano-sorptive stress describes the deformation of wood when under load with changing moisture content. Both creep and mechano-sorptive stress act to relieve elastic and shrinkage stresses during drying. The model developed by Oliver [90] defines the total strain from moisture loss as a combination of nonlinear elastic, creep, shrinkage, and mechano-sorptive components as follows:

$$\boldsymbol{\varepsilon} = \boldsymbol{\varepsilon}^{\boldsymbol{e}} + \boldsymbol{\varepsilon}^{\boldsymbol{X}} + \boldsymbol{\varepsilon}^{\boldsymbol{ms}} + \boldsymbol{\varepsilon}^{\boldsymbol{c}}, \qquad (1\text{-}25)$$

where: $\boldsymbol{\varepsilon}^{\boldsymbol{e}}$ is the elastic strain, $\boldsymbol{\varepsilon}^{\boldsymbol{X}}$ is the strain associated with moisture induced free shrinkage, $\boldsymbol{\varepsilon}^{\boldsymbol{ms}}$ is the mechano-sorptive strain and $\boldsymbol{\varepsilon}^{\boldsymbol{c}}$ is the creep strain.

Since the development of Oliver's one-dimensional model [90], similar one-dimensional models have been trialled [91, 92] and two-dimensional variants have been developed to simulate drying stresses [93-97] and board distortion during drying [98-101], and solved using Finite Element Analysis (FEA) techniques. Likewise, a three-dimensional model was developed to predict drying stresses [102] to simulate board distortion [103] taking into account the influence of annual ring orientation [104].

All of the reviewed models stem from the early work and theory developed by Schaffner [56] and later by Oliver [57]. For the model used in this thesis, the strain components in equation (1-25) are defined below.

Wood is an orthotropic material and it has three mutually orthogonal axes known as the axes of material symmetry. In the coordinate system defined by these three axes in the radial (*R*), tangential (*T*) and longitudinal (*L*) directions, material elastic stress is related to the elastic strain by the generalised Hooke's law [98], described by

$$\boldsymbol{\varepsilon^e} = \boldsymbol{C\sigma} \tag{1-26}$$

where

$\boldsymbol{\sigma}$ = stress vector $\boldsymbol{\sigma} = [\sigma_L \quad \sigma_T \quad \sigma_R \quad \tau_{RT} \quad \tau_{LT} \quad \tau_{LR}]^T$

$\boldsymbol{\varepsilon^e}$ = elastic strain vector $\boldsymbol{\varepsilon^e} = [\varepsilon_L \quad \varepsilon_T \quad \varepsilon_R \quad \gamma_{RT} \quad \gamma_{LT} \quad \gamma_{LR}]^T$

$\boldsymbol{C}$ = compliance matrix

The compliance matrix is given by

$$\mathbf{C} = \begin{bmatrix} \frac{1}{E_L} & \frac{-\upsilon_{RL}}{E_R} & \frac{-\upsilon_{TL}}{E_T} & 0 & 0 & 0 \\ \frac{-\upsilon_{LR}}{E_L} & \frac{1}{E_R} & \frac{-\upsilon_{TR}}{E_T} & 0 & 0 & 0 \\ \frac{-\upsilon_{LT}}{E_L} & \frac{-\upsilon_{RT}}{E_R} & \frac{1}{E_T} & 0 & 0 & 0 \\ 0 & 0 & 0 & \frac{1}{G_{RT}} & 0 & 0 \\ 0 & 0 & 0 & 0 & \frac{1}{G_{LT}} & 0 \\ 0 & 0 & 0 & 0 & 0 & \frac{1}{G_{LR}} \end{bmatrix} \tag{1-27}$$

where the material behaviour is described by the following parameters:

E_L, E_T, E_R = Young's moduli

G_{RT}, G_{LT}, G_{LR} = shear moduli

$v_{RT}, v_{LT,} v_{LR}, v_{RL}, v_{LT}, v_{LR} = \text{Poisson's ratios;}$

with $v_{RT} = v_{TR} \times \frac{E_R}{E_T}$; $v_{RL} = v_{LR} \times \frac{E_R}{E_L}$; $v_{LT} = v_{LT} \times \frac{E_T}{E_L}$.

The moisture induced shrinkage strain is dependent on the rate of change of moisture content $\mathcal{X}$ below the fibre saturation point and is given by:

$$\boldsymbol{\varepsilon}^{\mathcal{X}} = \boldsymbol{\alpha}\mathcal{X} \tag{1-28}$$

where $\boldsymbol{\alpha}$ is defined as:

$$\boldsymbol{\alpha} = [\alpha_L \quad \alpha_R \quad \alpha_T \quad 0 \quad 0 \quad 0]^T \tag{1-29}$$

and α_L, α_R and α_T are material shrinkage coefficients of moisture induced strain. Above the wood fibre saturation point, $\mathcal{X}_{fsp}$, these coefficients are assumed to be zero [46].

The model for mechano-sorptive strain was developed by Rybarkzyk [105] and is given by:

$$\frac{d\varepsilon^{ms}}{dt} = \boldsymbol{s}\boldsymbol{\sigma}\frac{d\mathcal{X}}{dt} \tag{1-30}$$

and was later updated by Salin [14] to include an upper deformation limit as follows:

$$\frac{d\varepsilon^{ms}}{dt} = \boldsymbol{s}(\boldsymbol{\sigma} - E_{ms}\varepsilon^{ms})\frac{d\mathcal{X}}{dt}, \tag{1-31}$$

where $E_{ms}$is a constant related to the maximal mechano-sorptive deformation achievable for a given stress level, $\mathcal{X}$ is the moisture content and matrix $\boldsymbol{s}$ is the mechano-sorptive matrix defined as:

$$\boldsymbol{s} = \begin{bmatrix} m_L & -u_{RL}m_R & -u_{TL}m_T & 0 & 0 & 0 \\ -u_{LR}m_L & m_R & -u_{TR}m_T & 0 & 0 & 0 \\ -u_{LT}m_L & -u_{RT}m_R & m_T & 0 & 0 & 0 \\ 0 & 0 & 0 & m_{RT} & 0 & 0 \\ 0 & 0 & 0 & 0 & m_{LT} & 0 \\ 0 & 0 & 0 & 0 & 0 & m_{LR} \end{bmatrix}, \tag{1-32}$$

where $m_L, m_R, m_T, m_{RT}, m_{LT}, m_{LR}, u_{LR}, u_{LT}, u_{RL}, u_{RT}, u_{TL}$ and u_{TR} are mechano-sorptive coefficients.

The following equation is commonly used to calculate creep strain in wood [100]:

$$\frac{d\varepsilon^c}{dt} = a.b.\boldsymbol{C}.\boldsymbol{\sigma}.\frac{t_h^{b-1}}{3600}, \qquad (1\text{-}33)$$

where a and b are constants, $\boldsymbol{C}$ is the compliance matrix given in equation (1-27) and t_h is elapsed time in hours.

Due to the complexity of developing the species specific mechano-sorptive coefficients [98], and previous reports stating that during drying, creep strain is only a minor component of the total strain [91, 106]. The stress/strain model used here includes only the elastic and moisture induced free shrinkage strains; the first two terms of equation (1-25). Therefore, a detailed review of the most recent works on mechano-sorptive and creep strains are not realised here because these mechanical properties are not considered further in the work. By excluding the stress relieving mechano-sorptive strain, our total strain results are expected to be higher than observed. However, the nature of our study is to investigate if a simplified version of the stress/strain model is able to predict the onset of surface checking and end splitting, as well as differences between the magnitude of these degrade types, observed between wood species, and conventional and vacuum drying trials.

1.2.8 Failure criteria and wood

The majority of stress/strain modelling outcomes presented in the previous section either describe the behaviour of drying stresses and strains in boards during drying, or are used to predict deformation in boards during drying. Very few researchers seem to have used their models to predict the failure of wood in terms of stress related drying degrade, in particular surface checking and end splitting.

The Tasmanian drying model developed by Schaffner [56] and Oliver [57] was refined by Booker [107] (SMARTKILN) to include an ultimate strain value for predicting the onset of surface checking for Tasmanian oak eucalypt species. The ultimate strain value was 0.02 and was determined by Schaffner [56] via laboratory tests. The SMARTKILN program has subsequently been used by Innes [33, 108] to predict internal and surface checking in Tasmanian oak species using the same ultimate strain value.

As the ultimate strain value depends on the species, and specialised equipment is required to perform laboratory tests, alternative methods were reviewed to predict wood failure for our model, focussing on surface checking and end splitting. A number of orthotropic multiaxial stress models exist that can be applied to wood failure [109]. Previous studies by Cabrero *et al*. [109] and Mascia and Simoni [110], investigated a number of different failure criteria for wood and concluded that the Tsai Wu failure criterion [111] is well suited for wood material.

Based on this work, the Tsai-Wu failure criteria, which takes into account the coupled tensile and compressive stresses experienced during drying, was chosen to predict surface check and end split failure for this study. End splitting and surface checking occur in the board cross-sectional plane: the board thickness and width directions. Therefore, in this research a two-dimensional Tsai-Wu criterion was used in the radial-tangential directions.

The Tsai-Wu criteria is a quadratic, stress-based criterion where failure is deemed to occur when the following condition is satisfied:

$$A + B + C + D + E + F \geq 1\,, \tag{1-34}$$

where the parameters in equation (1-34) are defined as [111]:

$$A = \frac{\sigma_1^2}{\sigma_{1t}^u \sigma_{1c}^u}, \tag{1-35}$$

$$B = \frac{\sigma_2^2}{\sigma_{2t}^u \sigma_{2c}^u}, \tag{1-36}$$

$$\mathrm{C} = \frac{\sigma_{12}^2}{(\tau_{12}^u)^2}, \tag{1-37}$$

$$D = \left(\frac{1}{\sigma_{1t}^u} - \frac{1}{\sigma_{1c}^u}\right)\sigma_1\,, \tag{1-38}$$

$$E = \left(\frac{1}{\sigma_{2t}^u} - \frac{1}{\sigma_{2c}^u}\right)\sigma_2\,, \tag{1-39}$$

$$F = \frac{2F_{12}^{*}\sigma_1\sigma_2}{\sqrt{\sigma_{1t}^u\sigma_{1c}^u\sigma_{2t}^u\sigma_{2c}^u}}. \tag{1-40}$$

In equations (1-35) to (1-40), the terms σ_1 and σ_2 represent the calculated stress in the perpendicular planar directions 1 and 2 (analogous to the Cartesian co-ordinates), respectively, and σ_{1t}^u, σ_{1c}^u, σ_{2t}^u and σ_{2c}^u represent the ultimate (*u*) tension (*t*) and compression (*c*) stress in directions 1 and 2. The shear strength in the 1-2 plane is represented by τ_{12}^u. Although the full Tsai-Wu failure criteria is used, simulations revealed that the compressive forces during drying are much less than the tensile forces, which reflects the tensile failure mode observed after drying. The F_{12}^{*} term in equation (13) is the *interaction coefficient* and is difficult to determine [109]. Tsai [112] proposed $F_{12}^{*} = -0.5$, which corresponds to the generalised Von Misses criterion [109] and is used for this analysis. The Tsai-Wu failure criteria in the wood radial (R and Tangential (T) directions can then be expressed as:

$$\begin{aligned}&\left(\frac{\sigma_T}{\sigma_{Tt}^u\sigma_{Tc}^u}\right)^2 + \left(\frac{\sigma_R}{\sigma_{Rt}^u\sigma_{Rc}^u}\right)^2 + \frac{\tau_{TR}^2}{(\tau_{TR}^u)^2} + \left(\frac{1}{\sigma_{Tt}^u} - \frac{1}{\sigma_{Tc}^u}\right)\sigma_T \\ &+ \left(\frac{1}{\sigma_{Rt}^u} - \frac{1}{\sigma_{Rc}^u}\right)\sigma_R - \frac{\sigma_T\sigma_R}{\sqrt{\sigma_{Tt}^u\sigma_{Tc}^u\sigma_{Rt}^u\sigma_{Rc}^u}} \geq 1\end{aligned} \tag{1-41}$$

The Tsai-Wu failure criteria used in this research is coupled to the drying model via the board shrinkage strain, and the relationship between stress and strain as explained by Hooke's law [98]. This is explained in detail in Chapter 6.

1.3 Objectives of the research

The objectives of the PhD research programme are stated in the following section and include two main objectives.

Objective 1. Develop a robust and precise hardwood heat and mass transfer drying model able to predict both vacuum and conventional drying behaviour.

The principal objective of this research is to gain a better understanding of the wood properties that explain the drying behaviour of Australian hardwoods, and to improve the modelling strategy for vacuum and conventional drying of these species. Wood properties that are difficult to predict will need to be identified and measured using specialised techniques. Where possible, other necessary wood properties will be predicted based on empirical formulae from the literature. Determined wood properties will be used as input parameters for the wood drying *TansPore* model.

Industry scale drying trial psychrometric kiln conditions, and the physical/mechanical behaviour of the boards, measured during drying trials will be used to validate and/or improve the drying model.

Two versions of the model will be developed: one modelling heat and mass transfer in the wood cross-sectional transverse radial (R)-tangential (T) plane, and the other in the transverse (R or T)-longitudinal (L) plane. This allows investigation of the effect of vacuum pressure on longitudinal migration and the associated internal pressures generated in the timber during vacuum drying compared with conventional drying.

Finally, a sensitivity analysis will be undertaken to rank the model input parameters in order of most to least sensitive, highlighting the input parameters essential for model precision. Model precision will be determined by calculating the error between simulated and experimental average moisture content and temperature during drying. The ability for the simulation to predict the time at the drying end point target average moisture content will be an important outcome of the modelling.

Objective 2. Develop a FEA stress/strain model that can predict stress-related drying degrade failure.

This objective stems from the results of a series of vacuum and conventional drying trials, used to validate objective 1, as reported by Redman [29]. During these trials, dried quality in terms of the distribution of average MC and MC gradient, and stress related degrade, including surface checking, end splitting, internal checking and collapse was quantified in accordance with Australian standards. Of the four species investigated, the following results were observed during the trials:

- messmate is prone to all forms of stress related degrade,
- messmate is the only species exhibiting collapse degrade,
- spotted gum has the lowest overall susceptibility to all of the combined forms of degrade, and
- vacuum drying typically induces less surface checking and end split type degrade of hardwoods, than conventional drying.

Therefore, the second objective of this work is, with the use of empirical wood property and input moisture content field data from the first objective, to develop a 3D stress-strain FEA model, allowing prediction of the development of stress related end splitting and surface checking degrade during conventional and vacuum wood drying. The mechanical wood properties necessary for this modelling work will be determined empirically from the literature.

Ultimately, the combined objectives will allow the optimisation of kiln drying schedules in terms of reducing drying times within acceptable levels of drying degrade.

For both objectives, four high commercial species based on their contrasting drying ability and wood properties were chosen. The reasons for this choice are to, (a) test the robustness of the *TransPore* model at simulating vacuum and conventional drying for a wide range of Australian hardwood species, and (b) to determine why some species are comparatively more prone to degrade from different forms of drying than others. The species chosen are spotted gum (*Corymbia citriodora*), messmate (*Eucalyptus obliqua*), blackbutt (*Eucalyptus pilularis*) and jarrah (*Eucalyptus marginata*). Spotted gum is the highest density (921 kg/m^3 BD) hardwood chosen, which is an easy-to-dry species whose drying rate is limited by surface checking and drying stress. Messmate, on the other hand, is the lowest density (489 kg/m^3 BD) species chosen and is prone to cell collapse and external and internal checking during drying. The drying ease, in terms of drying induced degrade, and density of the other two species lies in between the extremes of spotted gum and messmate.

1.4 Thesis structure

This thesis is presented by publications. The contribution to the literature is provided in the form of four published articles and one submitted manuscript. These five articles comprise each individual chapter of the thesis and are detailed below.

The underpinning contributions of the candidate (Adam Redman) were to identify the research problem, formulate the questions and to forge the necessary interdisciplinary collaborations required to answer the research questions. In particular, the candidate first identified the industry research need to establish the viability of vacuum drying Australian hardwoods in terms of drying time, quality and cost. Subsequently, the candidate recognised that, to fully understand the problem, accurate mathematical modelling of heat and mass transfer and stress related degrade prediction during drying, was necessary. The research question was so complex that the candidate needed to form collaborative links with experts in wood science, mathematics, engineering and computational techniques. The candidate, with the guidance from his supervisors, initiated collaborations with experts at the Centrale Supelec, Université Paris-Saclay, Queensland University of Technology (QUT), Queensland Cyber Infrastructure Foundation (QCIF) to answer the research question and embark on this PhD work.

The following thesis structure contains a ‘Statement of Authorship’ section for each chapter in accordance with the Queensland University of Technology requirements.

1.4.1 Chapter 2: Mass transfer properties

Article. Redman A.L., Bailleres H., Turner I.W., Perré P. (2012), Mass transfer properties (permeability and mass diffusivity) of four Australian hardwood species, Bioresources, 7(3): 3410-3424.

Abstract. Characterisation of mass transfer properties was achieved in the longitudinal, radial, and tangential directions for four Australian hardwood species: spotted gum, blackbutt, jarrah, and messmate. Measurement of mass transfer properties for these species was necessary to complement current vacuum drying modelling research. Mass diffusivity was determined in steady state using a specific vapometer. Permeability was determined using a specialized device developed to measure over a wide range of permeability values. Permeability values of some species and material directions were extremely low and undetectable by the mass flowmeter device. Hence, a custom system based on volume evolution was conceived to determine very low, previously unpublished, wood permeability values. Mass diffusivity and permeability was lowest for spotted gum and highest for messmate. Except for messmate in the radial direction, the four species measured were less permeable in all directions than the lowest published figures demonstrating the high impermeability of Australian hardwoods, partly accounting for their relatively slow drying rates. Permeability, mass diffusivity, and associated anisotropic ratio data obtained for messmate were extreme or did not follow typical trends and is consequently the most difficult of the four woods to dry in terms of collapse and checking degrade.

1.4.2 Chapter 3: Wood property characterisation – Part 1

Article. Redman A.L., Bailleres H., Perré P. (2011), Characterisation of viscoelastic, shrinkage and transverse anatomy properties of four Australian hardwood species, Wood Material Science and Engineering, 7: 95-104.

Abstract. Several key wood properties of four Australian hardwood species: spotted gum, blackbutt, jarrah and messmate, were characterised using 'state of the art' equipment in France. The wood properties were measured for input into microscopic (cellular level) and macroscopic (board level) vacuum drying models currently under development. Morphological characterisation was completed using a combination of environmental scanning electron microscopy and image analysis software. A clear difference in fibre porosity, size, wall thickness and orientation was evident between species. Viscoelastic properties were measured in the tangential and radial directions using dynamic mechanical analysis instrumentation. The glass transition temperature was markedly different for each species due to anatomical and chemical variations. The radial direction showed higher stiffness, internal friction and glass transition temperature than the tangential directions. A highly sensitive microbalance and laser technology were used to measure loss of moisture content in conjunction with directional shrinkage on microsamples. Collapse shrinkage was clearly evident with this method for messmate, but not with other species, consistent with industrial drying experience. To characterise the wood-water relations of messmate, free of collapse, thinner sample sections (in the radial-tangential plane) are recommended.

1.4.3 Chapter 4: Wood property characterisation – Part 2

Article. Redman A.L., Bailleres H., Turner I.W., Perré P. (2016), Characterisation of wood-water relationships and transverse anatomy and their relationship to drying degrade, Wood Science and Technology, Volume 50, Issue 4, pp. 739-757 (2016).

Abstract. Characterisation of a number of key wood properties utilising 'state of the art' tools was achieved for four commercial Australian hardwood species: spotted gum, blackbutt, jarrah and messmate. The wood properties were measured for input into microscopic (cellular level) and macroscopic (board level) vacuum drying models currently under development. Morphological characterisation was completed using a combination of ESEM, optical microscopy and a custom vector-based image analysis software. A clear difference in wood porosity, size, wall thickness and orientation was evident between species. Wood porosity was measured using a combination of fibre and vessel porosity. A highly sensitive microbalance and scanning laser micrometres were used to measure loss of moisture content in conjunction with directional shrinkage on micro-samples of messmate to investigate the validity of measuring collapse-free shrinkage in very thin sections. Collapse-free shrinkage was characterised, and collapse propensity was verified when testing thicker samples. Desorption isotherms were calculated for each species using wood–water relations data generated from shrinkage experiments. Fibre geometry and wood shrinkage anisotropy were used to explain the observed difficulty in drying of the different species in terms of collapse and drying stress-related degrade.

1.4.4 Chapter5: Heat and mass transfer drying model

Article. Redman A.L., Bailleres H., Perré P., Carr E.J., Turner I.W. (2017). A relevant and robust vacuum drying model applied to hardwoods, Published online in Wood Science and Technology journal on 24 April 2017.

Abstract. A robust mathematical model was developed to simulate the heat and mass transfer process that evolves during vacuum drying of four commercially important Australian native hardwood species. The hardwood species investigated were spotted gum (*Corymbia citriodora*), blackbutt (*Eucalyptus pilularis*), jarrah (*Eucalyptus marginata*), and messmate (*Eucalyptus obliqua*). These species provide a good test for the model based on their extreme diversity between wood properties and drying characteristics. The model uses boundary condition data from a series of vacuum drying trials, which were also used to validate predictions. By using measured diffusion coefficient values to calibrate empirical formula, the accuracy of the model was greatly improved. Results of a sensitivity analysis showed that the model outputs provide excellent agreement with experimental observation despite the large range of species behaviour and variation in wood properties. This study confirms that the drying rate is significantly improved as a direct result of the enhanced convective and diffusive transfer along the board thickness. Contrary to softwood, it appears that longitudinal migration provides only a secondary effect. Not only is the model able to predict the heat and mass transfer behaviour of a range of hardwood species, it is also flexible enough to predict the behaviour for both conventional and vacuum drying scenarios. The outcomes of this work provide the hardwood industry with a well calibrated predictive drying tool that can be used to optimise drying schedules.

1.4.5 Chapter 6: Drying stress FEA model

Article. Redman A.L., Bailleres H., Perré P. Gilbert B.P., Carr E.J., Turner I.W., Perré P. (2017). Finite element analysis of stress-related degrade during drying of *Corymbia citriodora* and *Eucalyptus obliqua,* Wood Science and Technology, submitted after review on 22 July 2017.

Abstract. With the use of experimental wood properties and input moisture content field data, we developed a predictive 3D stress-strain finite element analysis (FEA) model allowing us to predict the development of stress related end splitting and surface checking degrade during conventional and vacuum wood drying. Simulations were carried out for two Australian hardwood species, messmate (*Eucalyptus obliqua*) and spotted gum (*Corymbia citriodora*) as these species contrast, in terms of wood properties, drying rates and stress degrade susceptibility. The simulations were performed using a 1/8 symmetry model where the full board dimensions are 1,900 mm long x 30 mm thick x 100 mm wide. Moisture content field data model simulations were utilised in a three-dimensional FEA model by extruding a 2D moisture content field computed in the T-L plane across the radial direction to create a 3D model. Material mechanical properties and shrinkage were calculated in relation to moisture content, over discrete time intervals, using a quasi-static solver. End split failure was investigated at the board end, and surface check failure at the board surface, using a Tsai-Wu failure criterion. Simulations showed that messmate was more susceptible to end splitting than spotted gum and that conventionally dried messmate was more susceptible to surface checking than vacuum dried messmate. The same results were observed from drying trials. The location of predicted surface

check failure also matched drying trials and are compared.

1.4.6 Conclusions

This chapter will summarise and review the work, demonstrate how the objectives outlined in Section 1.3 were achieved, list the key results of the research, and conclude with some directions for future research.

Chapter 2
Mass transfer properties

This chapter features the bulk of the published journal article "*Mass transfer properties (permeability and mass diffusivity) of four Australian hardwood species*" published in Bioresources, Volume 7, Issue 3, pp. 3410-3424 (2012), where some minor alterations have been made based on reviewers' comments.

Statement of Authorship. This work was divided as follows:

- *Mr. Adam Redman* (Candidate) wrote the majority of the article, performed the experimental procedures and designed most of the experimental methods to characterise the wood properties required to model the drying process.
- *Dr. Henri Bailleres* assisted in the methodology and proposed the collaboration with Professors Turner and Perré to perform experiments in France.
- *Prof. Ian Turner* assisted in developing the collaboration and was instrumental in developing the mathematics and code for the *TransPore* model.
- *Prof. Patrick Perré* directed and guided the work, designed many of the experimental methods and proposed the customised technique to measure very low wood permeability.

SIGNED:

DATE:
19/8/2017

2.1 Introduction

In recent years, with emerging technological advancements in construction, design, computer control, and less expensive materials, vacuum drying of hardwood timber, particularly in Europe and USA, has proven in many applications to be a more economical alternative to drying using conventional methods, with similar or better quality outcomes [4]. In light of this, the Australian hardwood timber industry invested in a project with Queensland Government's Department of Employment, Economic Development and Innovation (DEEDI) to establish the viability of vacuum drying technology for drying four high volume and value commercial Australian hardwood species with respect to drying quality, time, and cost. Australian *Eucalyptus* are notoriously difficult to dry without degrade [10, 113]. Moreover, we recognized that a better knowledge of the material and associated drying behaviour is required to optimize the vacuum drying process in the future. Therefore, a component to develop a hardwood vacuum drying model was included in the project.

Currently, much modelling work has been conducted for softwood species due to its commercial importance and relative homogeneity between species [8, 16, 63, 114, 115]. The complexity of the wood structure of hardwoods paired with the huge variation within and between species has resulted in limited deterministic modelling work being performed to date on these species.

Previous research [25, 116] has identified a number of essential wood properties that must be measured to provide the necessary structure for developing an accurate drying model. For the mass transfer component of drying modelling, measurement of the key parameters permeability and water-vapour diffusivity are required. Knowledge of these parameters is also important for understanding and describing the mechanisms that govern wood preservative impregnation. Very little data is available on the permeability and water vapour diffusivity characteristics for the species under investigation.

The objectives of this study are to characterize (1) the air permeability, which defines the mass flux in response to a pressure gradient, and (2) the water-vapour diffusivity, which defines the mass flux in response to a concentration gradient, of four highly commercial Australian hardwood species to complement current vacuum drying modelling research. This research takes advantage of the existing deterministic model *TransPore* [7, 16] used to predict the drying behaviour of softwoods and drying of other porous media such as concrete.

The species under investigation are mature native forest spotted gum (*Corymbia citriodora* Hook), blackbutt (*Eucalyptus pilularis* Sm), jarrah (*Eucalyptus marginata* D.Don ex Sm.), and messmate (*Eucalyptus obliqua* L'Herit.). We chose the species based on their large commercial volume, value, and range of drying characteristics and wood properties. For example, spotted gum is the easiest species to dry in terms of resistance to drying degrade and has the highest basic density (BD) of 1000 kg/m^3 [117], followed by blackbutt (710 kg/m^3) and jarrah (670 kg/m^3), which are mildly susceptible to surface checking. Finally, messmate is one of Australia's hardest species to dry due to its propensity to collapse, internal and surface check, and has the lowest BD of 630 kg/m^3. This raises the question as to what role do wood anatomy and properties play in the vastly different drying behaviours of these species. This forms the basis of the study.

2.2 Materials and methods

2.2.1 Materials

Material for this study was selected from kiln dried material from concurrent vacuum drying studies [20], where the median density board most closely aligned to the average drying rate during a drying trial. Thus, for each species, we selected the board having the median basic density from a quantity of 100 samples to measure the mass transfer properties. For each species, one quartersawn and one backsawn board with dimensions 300 x 100 x 8 mm (L, R, T and L, T, R orientations, respectively) was prepared. Three 74 mm diameter samples were cut using an 80 mm diameter hole-saw for each board producing three radial and three tangential (in thickness direction) samples per species. In addition, one 200 x 100 x 28 mm thick sample was prepared. From those boards, we cut three 19 mm diameter, 20 mm long cylinders using a 24 mm hole-saw in the same longitudinal symmetry plane (Figure 2.1). These samples were used to determine longitudinal permeability. Due to the amazingly low permeability encountered for spotted gum, the samples were cross cut in half to produce 10 mm long samples. The side surfaces of all specimens were coated with two layers of epoxy resin to guarantee the air tightness of the lateral surfaces during measurement.

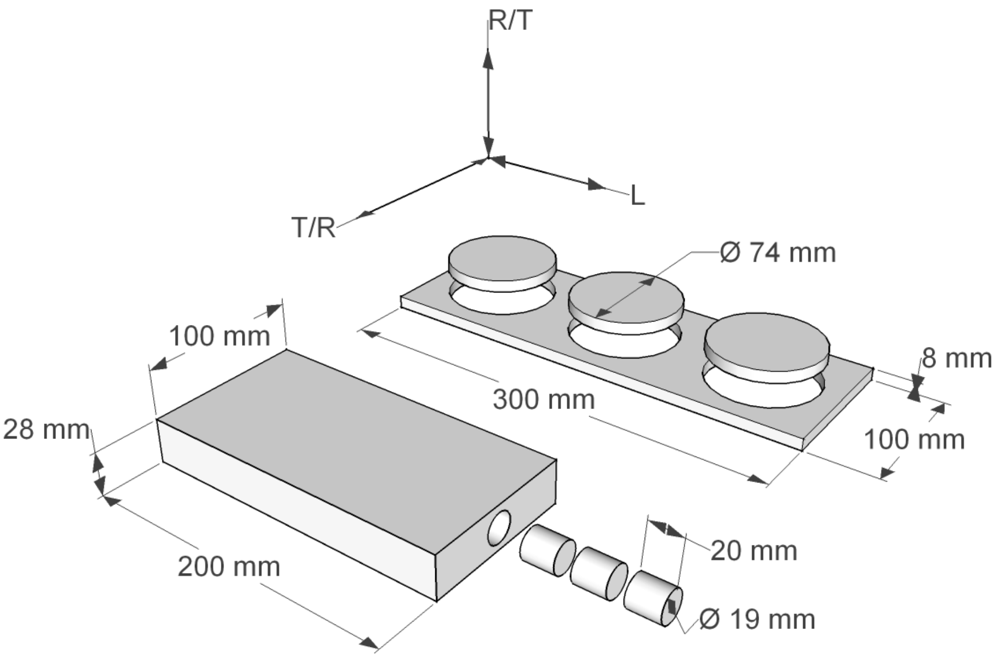

Figure 2.1 Sample preparation for permeability tests: foreground – longitudinal (L) sampling, background – radial (R), and tangential (T) sampling

2.2.2 Permeability

The need to carry out measurements of permeability to air of various species, along the three material directions and at different pressure levels requires an accurate and reliable device capable of measurement over a wide range of permeability values. For this purpose, the team at AgroParisTech, France developed a system called ALU-CHA as described by Rousset *et al.* [118]. The originality of this medium lies in a high reliability of lateral air tightness, the rapid operation, and the possibility to measure permeability with the same samples as those employed for the diffusion measurements. This device (Figure 2.2) allows us to apply an accurate and constant pressure difference between the two faces of the sample. We can determine the corresponding gas flux by a mass flowmeter, whose principle lies in the measurement of the thermal perturbation due to the gas flux when it passes through a capillary tube.

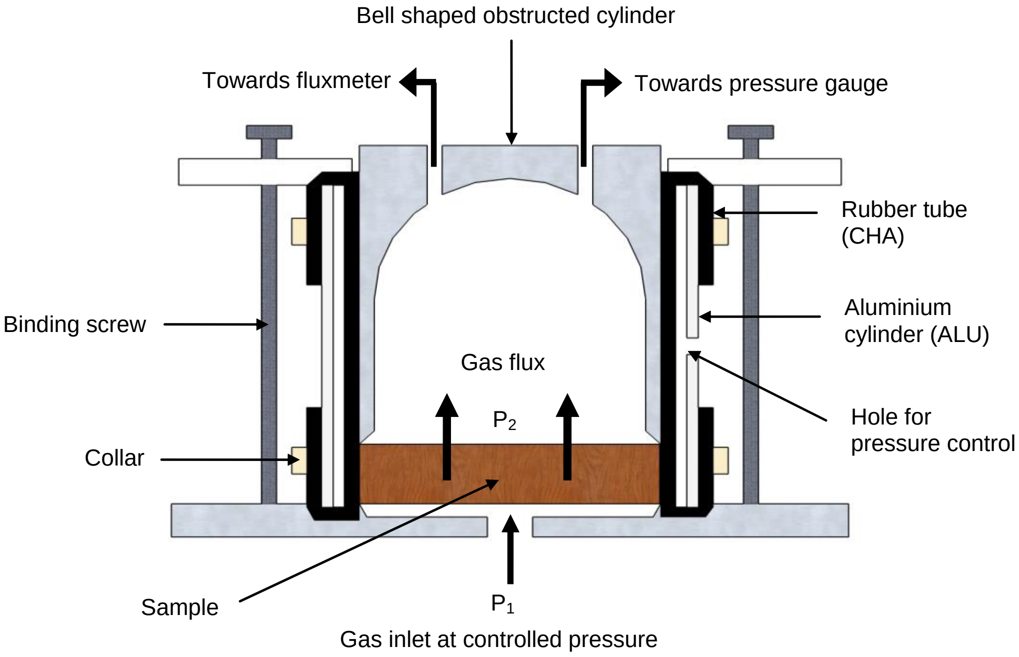

Figure 2.2 Schematic of sample support with ALU-CHA system for permeability measurements

Note the presence of a rubber tube around the sample. A partial vacuum applied over the hole in the aluminium chamber, sucking the rubber tube to the aluminium chamber, enables easy placement or removal of the sample. During measurement, we applied a typical pressure of 2–3 bar in the chamber to press the rubber joint against the lateral face of the sample for air tightness. In addition, before placing the specimen in the ALU-CHA system, a silicone-based grease of high viscosity (vacuum grease) applied on the lateral surfaces of the specimen inhibits surface flow in the micro-porosity layer formed between the epoxy resin and rubber surfaces. We carried out measurements by applying a controlled and constant pressure difference (ΔP) between two faces of the specimen and then measuring the corresponding air flux (Q). All measurements occurred in a temperature-controlled room with minimum temperature fluctuations. Due to the effect of temperature on the air viscosity, we recorded room temperature before each measurement. The air flux permeating through the specimen was recorded when the flowmeter exhibited a nearly constant airflow. The air permeability of each sample was then calculated by Darcy’s law [35]

$$K = \frac{Q\mu eP}{A\Delta P\overline{P}'} \qquad (2\text{-}1)$$

where K is the intrinsic permeability (m^2); Q is the air flux (m^2 s^{-1}); μ is the dynamic viscosity of air (Pa s); e is the sample thickness (m); P is the pressure at which flux Q is measured (Pa); A is the sample area (m^2); $\Delta P = P_2 - P_1$is the pressure difference between the air outlet (P_2) and inlet (P_1) sides of the sample (Pa); $\overline{P} = \frac{(P_1+P_2)}{2}$ is the averaged pressure inside the sample (Pa).

For each measurement, we tested three pressure differentials: between 100 and 1000 mbar. The validity of Darcy’s law was proved for all test samples by the linear correlation found between the pressure difference (ΔP) and air flux (Q).

We remark that although Knudsen diffusion for gas flow is considered as a potential factor affecting the accuracy of permeability measurements, we assumed it negligible for the gas permeability measurements performed here. To justify this, we argue as follows: It is well known that when the capillary dimensions are smaller or of the same order as the mean free path (the average distance molecules travel between collisions), Knudsen diffusion or slip flow occurs because the molecules frequently collide with the capillary wall. The mean free path of air molecules at 20°C and 1 atmosphere is 0.068 μm and slip flow is significant in capillary openings near this size or smaller [21]. However, as the average pit aperture diameter for eucalypts is reported to be 0.6 μm [119], a factor of 10 times larger than the mean free path, the effect of Knudsen diffusion or slip flow on gas permeability measurements was deemed negligible.

Two ALU-CHA systems were used to cater for the two diameter classes of specimens. One system for the longitudinal samples and another for the larger diameter transverse samples.

For most species, permeability measurements in the radial and tangential directions could not be achieved using the regular experimental set-up, as the permeability was too low (less than 10^{-18} m^2), which is below the range offered by the flowmeter. Consequently, we disconnected the flowmeter and conceived a custom system, based on volume evolution, connected to the gas output of the ALU-CHA system. This entailed a flexible silicon hose connected to a glass tube with an internal radius of 2.87 mm. We calibrated the radius of the tube using a laboratory pipette. We placed the glass tube in a beaker of water next to a 0.5 mm increment gauge (Figure 2.3). The permeability of the sample could then be measured using equation 1, where the flux was determined by measuring the volume of the displacement of water in the tube as a function of time (measured using a chronometer) at different pressure gaps. Instead of measuring permeability over a matter of seconds or minutes, the flow was so low that, in spite of the small tube diameter, hours or days were required to obtain accurate measurements using this method. This method, although relatively simple, was able to increase the range of permeability values by four orders of magnitude, from 10^{-18} to 10^{-22} m^2.

We considered the effect on the backpressure caused by the water in the glass during testing as insignificant and was not included in the calculations. As the height of displaced water measured was never more than 10mm this represents a static backpressure of approximately 1 mbar. When compared to the pressure gap imposed on both sides of the sample ranging from 100 to 1000 mbar then the effect of the water column represents an error 1 to 0.1%, respectively.

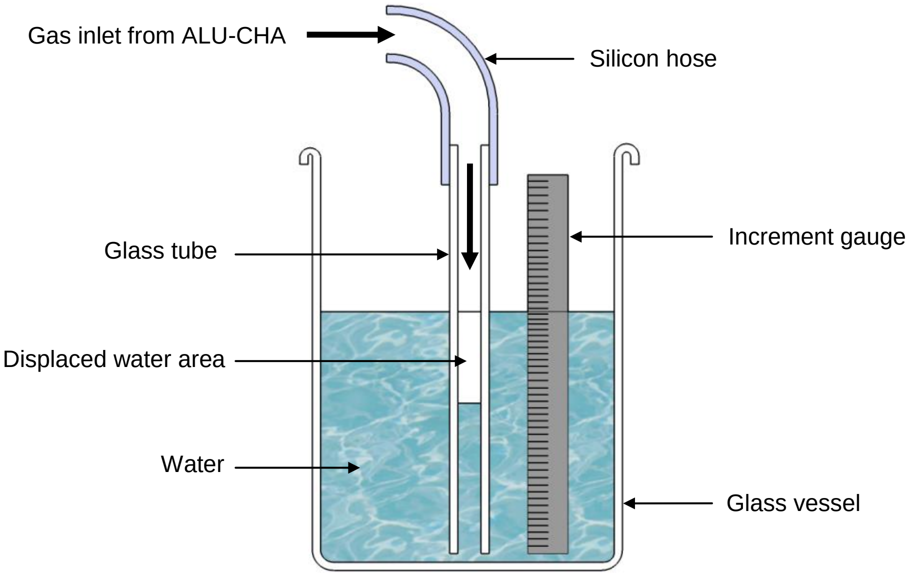

Figure 2.3 Schematic of system developed to measure samples with very low permeability

2.2.3 Water-vapour diffusivity

We used the same specimens to determine the mass diffusion coefficient as those used to measure permeability in each direction for each species. Due to its reduced complexity, we chose the steady-state determination of water-vapour diffusivity, whereby two different values of air humidity are applied on each side of the sample. The principle of measurement in the steady-state regime uses the technique of the vaporimeter (Figure 2.4). The vaporimeters used for these experiments are based on the PVC-CHA system developed by the team at AgroParisTech, France as described by Agoua and Zohoun [49].

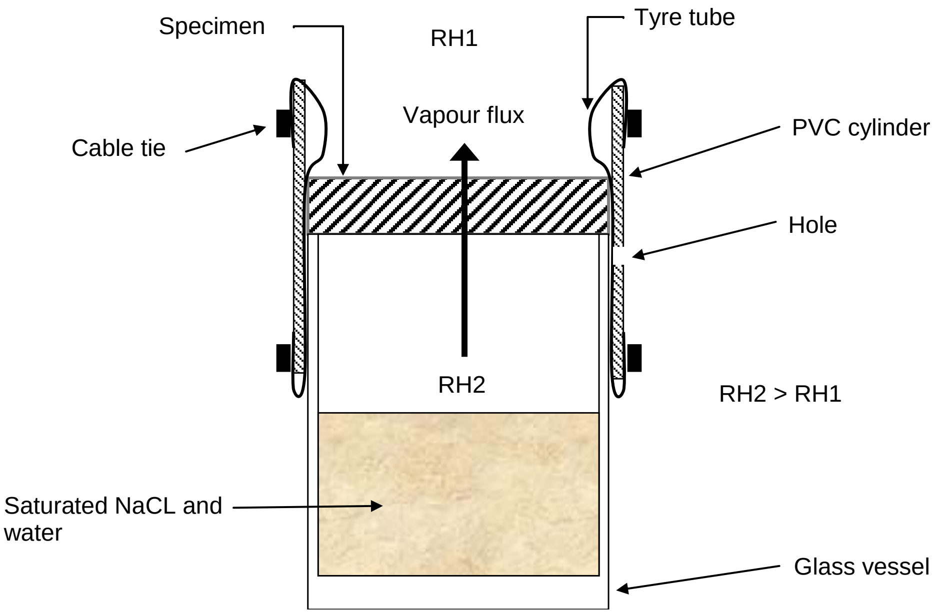

Figure 2.4 Schematic of sample support with PVC-CHA system for water-vapour diffusivity measurements

Wood specimens were initially equalized in a constant humidity and temperature chamber at 75 ± 2% relative humidity and 35 ± 0.1ºC to produce equilibrium conditions of 14% moisture content (MC).

The circular specimens were placed onto similar diameter cylindrical glass vessels containing a saturated solution of de-ionized/purified water and chemical grade (>99.9%) NaCl. For a given temperature, the partial pressure of vapour relates directly to relative humidity. A saturated salt solution inside the vessel generates a relative humidity (RH2) of 75% at 35ºC.

To create an airtight seal around the device, we used a cylinder of PVC with piece of inner tube attached inside the PVC, clamped using cable ties. Using a vacuum, we removed air through a small hole drilled into the side of the PVC pipe sucking the inner tube against pipe wall. This enabled the apparatus to be lowered over the specimen and glass. By releasing the vacuum, the inner tube relaxes tightly against the specimen and the vessel creating an airtight seal.

We placed the vaporimeter devices into the constant environment chamber at 35ºC and 40% relative humidity (RH1) to produce equilibrium conditions of 7% MC. With this device assembly, two different relative humidities occur on each side of the wood specimen to create a diffusive flux driving force through the sample. By weighing the device periodically over time, the device allowed the calculation of vapour flux. To make sure the experimental environment was undisturbed; we weighed the samples inside the chamber via sealed glove gauntlets attached to the chamber door, using a mass balance, accurate to 1 mg, placed inside the chamber.

By plotting the weight change as a function of time, we observed a steady-state relationship after a few days when the plot of weight change versus time becomes a straight line (constant rate). The diffusion coefficient through gross wood (D_b) is calculated from the following formula [21]

$$D_b = \frac{mL}{tAG\rho_w \mathit{\Delta} X}, \tag{2-2}$$

where m is the mass of vapour transferred (kg); L is the specimen thickness (m); t is time (s), A is the specimen surface area (m^2); G is the specific gravity of the specimen at moisture content X; $\rho_w$is the density of water (kg m^{-3}); $\mathit{\Delta} X$ is the moisture content difference between the two parallel surfaces of the specimen (kg kg^{-1}). $\mathit{\Delta} X$ is calculated using

$$\Delta X = \frac{X_b + X_t}{2}, \tag{2-3}$$

where X_b is the moisture content of the specimen bottom (kg kg^{-1}); X_t is the moisture content of the specimen top (kg kg^{-1}). For these tests, $X_b$andX_t were calculated using previously determined specific sorption/desorption isotherms for each species [20].

2.3 Results and discussion

2.3.1 Permeability

Table 2.1 contains the average permeability results measured for each species in the longitudinal, radial, and tangential directions. The results highlight the dramatic anisotropy ratios of these species and the vast difference between species. It is stated in Perré [36] that "wood has dramatic anisotropy ratios: the longitudinal permeability can be 1000 times greater than the transverse permeability for softwoods, and more than 10^6 for hardwoods". This is certainly the case for the species measured here, where the longitudinal to transverse anisotropy ratio was in the order of 10^6 for some species. No permeability values were measured for spotted gum in the radial direction as, even after 24 hours, no noticeable measurement could be made, indicating this species is highly impermeable in this direction ($<10^{-23}$ m^2).

Table 2.1 Longitudinal (L), radial (R), and tangential (T) permeability (K) and anisotropy ratios for spotted gum, blackbutt, jarrah, and messmate

Species	K (m^2)			Anisotropy Ratio		
	L×10^{-15}	R×10^{-18}	T×10^{-18}	K_L/K_R	K_L/K_T	K_R/K_T
Spotted gum	0.4	-	0.003		4750	
Blackbutt	35.0	0.01	0.02	2440000	2305000	0.9
Jarrah	67.4	0.05	0.04	3005000	1531000	1.1
Messmate	55.5	8.6	0.30	16400	3086000	177

Spotted gum was the least permeable species, with the permeability order of magnitude of the other species changing depending on wood direction. The radial to tangential permeability anisotropy ratio of messmate was in the order of 10^2 and is markedly higher than the other species tested. Table 2.2 shows permeability for other species published by Agoua and Perré

[120]. Data are provided for maritime pine and spruce (softwoods), beech (temperate hardwood), and teak (tropical hardwood). Except for messmate in the radial direction, the four species measured in this work are less permeable in all directions than the lowest published figure Table 2.2. This demonstrates the low permeability of Australian hardwoods compared to other species [120] partly accounting for their relatively slow drying rates.

Table 2.2 Published longitudinal (L), radial (R), and tangential (T) gas permeability (K) and anisotropy ratios for other species [120]

	K (m^2)			Anisotropy Ratio		
Species	$L \times 10^{-15}$	$R \times 10^{-18}$	$T \times 10^{-18}$	K_L/K_R	K_L/K_T	K_R/K_T
Maritime pine *(Pinus pinasta)*	328	1650	542	199	606	3
Spruce (*Picea abies*)	94	110	516	858	182	0.2
Beech (*Fagus sylvatica*)	742	74	367	9970	2020	0.2
Teak (*Tectona grandis*)	1750	4.82	5.69	363000	307000	0.8

2.3.2 Water-vapour diffusivity

Figure 2.5 to Figure 2.8 show the evolution of mass loss over time in the transverse and longitudinal directions for each species. As radial and tangential sample diameters were much larger than those in the longitudinal direction, and because the samples were of slight varying thickness, to correct for the effect of sample geometry, we divided the mass loss by the sample cross-sectional area and multiplied by the sample length. Both figures show two distinctive groups of curves, one of small slopes and one of extensive, larger slopes. The large sloped curves represent fluxes of water vapour in the longitudinal direction, and the small sloped curves through the transverse directions.

The vapour flux in all directions is markedly lower for spotted gum than for messmate, with the other species falling in between. This may be attributed to the vast anatomical and chemical differences between these species [30] that would lead to different structural parameters [120].

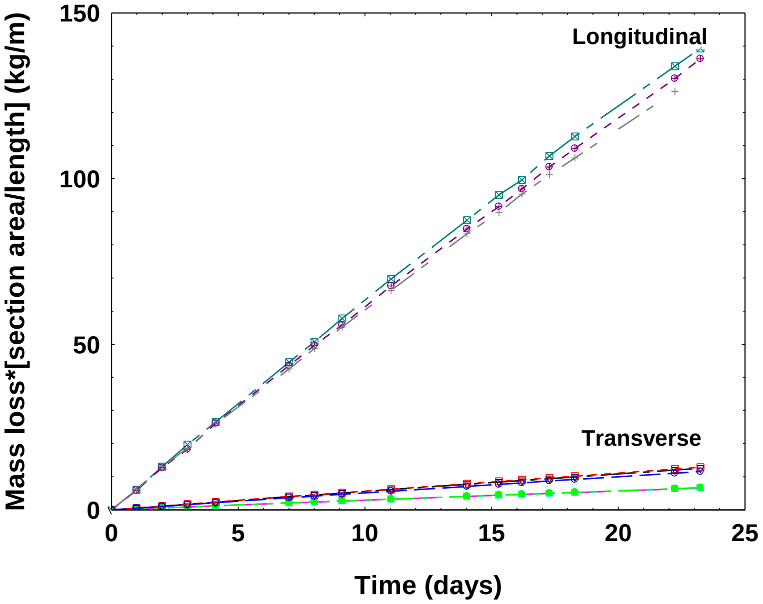

Figure 2.5 Evolution of bound water flux corrected for sample geometry in the R, T, and L directions for messmate

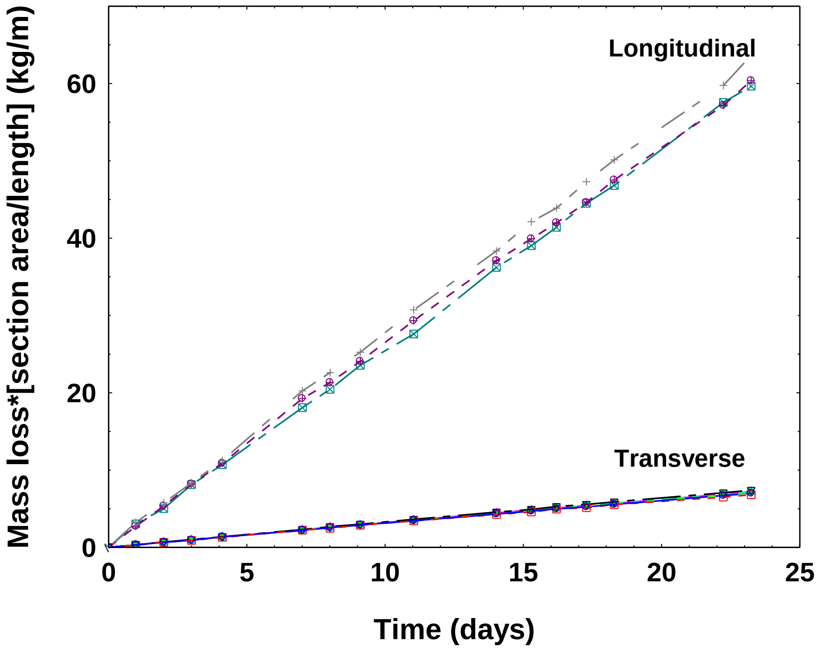

Figure 2.6 Evolution of bound water flux corrected for sample geometry in the R, T, and L directions for jarrah

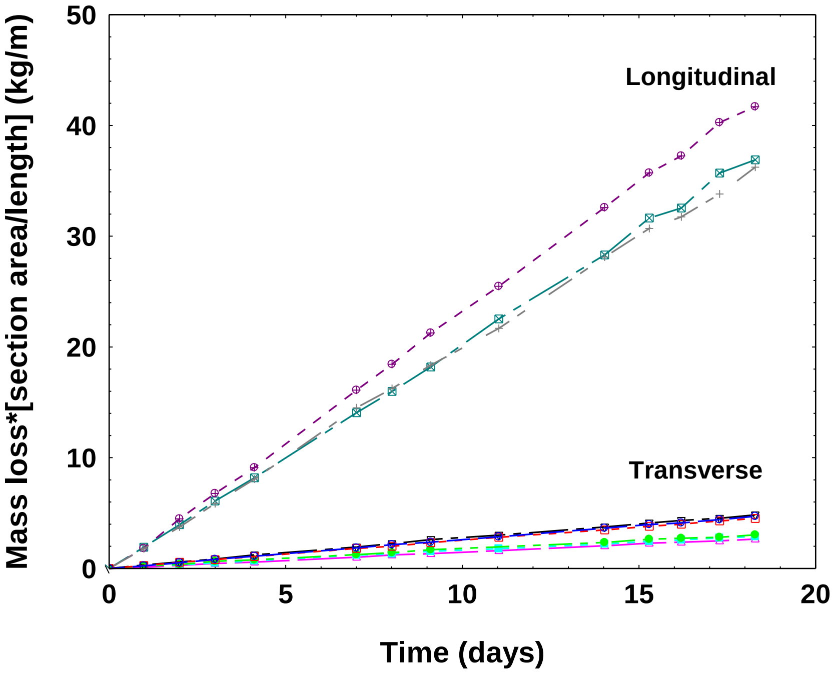

Figure 2.7 Evolution of bound water flux corrected for sample geometry in the R, T, and L directions for blackbutt

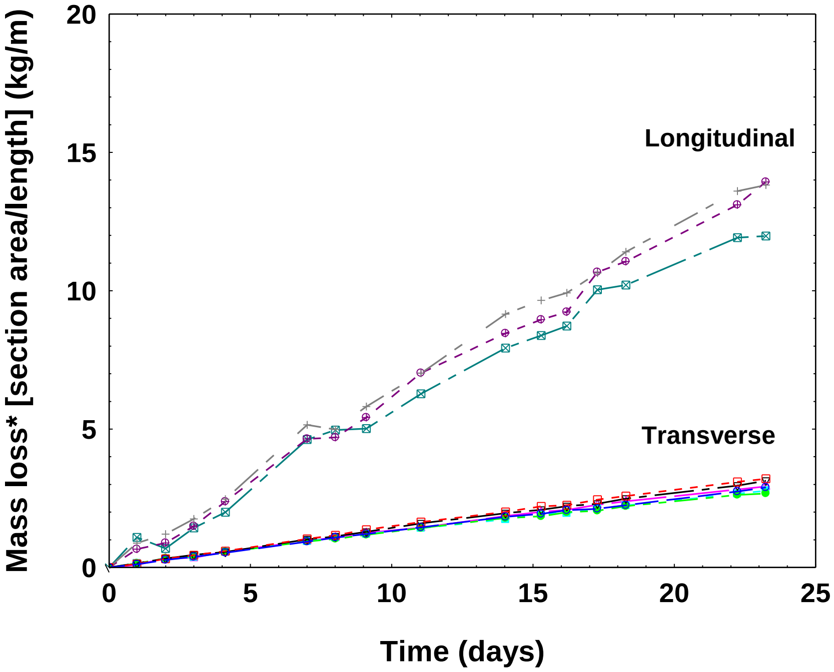

Figure 2.8 Evolution of bound water flux corrected for sample geometry in the R, T, and L directions for spotted gum

Table 2.3 contains the measured diffusion coefficients in the radial, tangential, and longitudinal directions for each species. Spotted gum diffusion coefficients were much lower in all directions compared with the other species tested, with messmate having the highest value. The radial to tangential anisotropic ratio of the diffusion coefficient for spotted gum was approximately 1:1 indicating a behaviour close to isotropy in this plane. This is evident in many other wood property ratios measured for this species [30]. The converse is true for the other species tested where we observed relatively higher diffusion-coefficient anisotropy ratios, which is again reflective of the other wood properties measured for these species.

Table 2.3 Longitudinal (L), radial (R), and tangential (T) diffusion coefficients (D_b) and anisotropy ratios for spotted gum, blackbutt, jarrah, and messmate

Sample #	D_b (m^2 s^{-1})			Anisotropy ratio		
	L×10^{-10}	R×10^{-10}	T×10^{-10}	D_{bL}/D_{bR}	D_{bL}/D_{bT}	D_{bR}/D_{bT}
Spotted gum	0.6	0.1	0.1	4.2	4.2	1.0
Blackbutt	2.3	0.3	0.2	8.8	14.2	1.6
Jarrah	2.7	0.3	0.4	10.5	7.2	0.7
Messmate	10.3	0.7	0.4	14.6	25.4	1.7

Published diffusion coefficient data measured using the steady-state method is shown in Table 2.4 [120]. We measured these data using the same samples as the permeability shown in Table 2.1. The diffusion coefficient results for the Australian hardwoods were, in all cases, markedly lower than the published figures. This indicates that the low diffusivity of Australian hardwoods compounds their relatively slow drying rates.

We can observe the relatively low diffusivity and permeability of Australian hardwoods compared to other published hardwood and softwood species by plotting diffusion coefficients against permeability using Table 2.1 and Table 2.4 data (Figure 2.9 in the transverse directions and Figure 2.10 in the longitudinal direction). We observe that in both the transverse and longitudinal directions, there is an obvious demarcation between the Australian hardwood and published species groups emphasizing the slow and difficult nature of removing water from Australian hardwoods.

Table 2.4 Published longitudinal (L), radial (R), and tangential (T) gas diffusion coefficients (D_b) and anisotropy ratios for other species [120]

	D_b (m^2 s^{-1})			Anisotropy Ratio		
Species	L×10^{-10}	R×10^{-10}	T×10^{-10}	K_L/K_R	K_L/K_T	K_R/K_T
Maritime pine *(Pinus pinasta)*	143	4.3	2.9	33.1	49.1	1.5
Spruce (*Picea abies*)	196	1.6	1.3	123	148	1.2
Beech (*Fagus sylvatica*)	86	4.8	2.1	18.1	40.6	2.25
Teak (*Tectona grandis*)	40	2.8	1.7	14.1	23.7	1.68

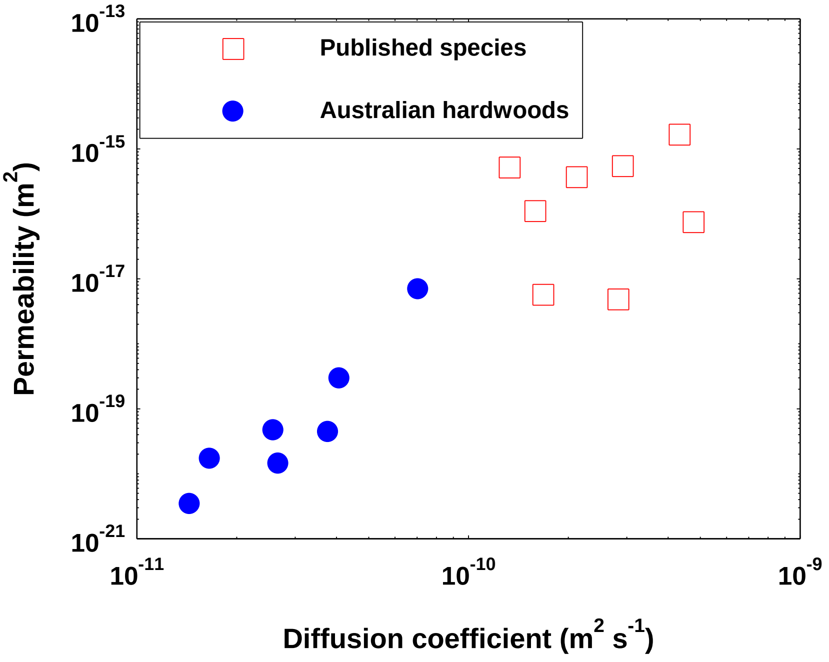

Figure 2.9 Relationship between diffusion coefficient and permeability in the radial and tangential directions for Australian hardwoods and published mixed species

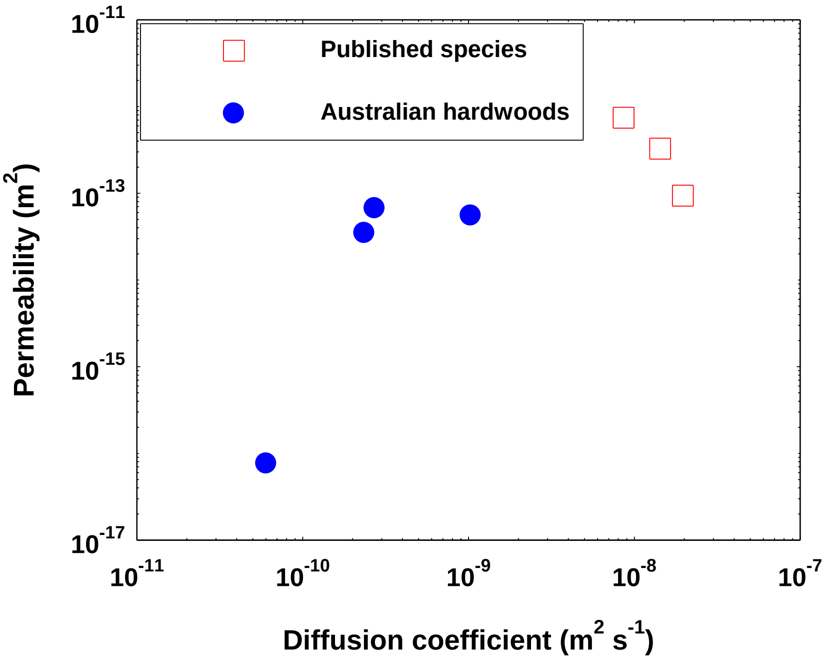

Figure 2.10 Relationship between diffusion coefficient and permeability in the longitudinal directions for Australian hardwoods and published mixed species

2.4 Conclusions

We characterized air permeability and mass diffusivity transfer properties of four highly commercial Australian hardwood species in the longitudinal, radial, and tangential directions.

Through the development of a custom system, based on volume evolution, we were able to measure, previously unpublished, very low wood permeability values.

We found spotted gum to be highly impermeable, particularly in the radial direction as, even after 24 hours, no noticeable measurement could be made.

The radial to tangential permeability anisotropy ratio of messmate was in the order of 10^2, markedly higher than for the other species tested.

Except for messmate in the radial direction, the four species measured were less permeable in all directions than the lowest published figures demonstrating the high impermeability of Australian hardwoods partly accounting for their relatively slow drying rates.

Diffusion coefficient was lowest in all directions for spotted gum and highest for messmate.

The ratio of longitudinal diffusion to both radial and tangential directions is much greater for messmate than spotted gum, indicating messmate's greater propensity for drying in the longitudinal direction. This is advantageous during vacuum drying and acts to complement current vacuum drying modelling research.

Comparing the relationship between permeability and diffusion coefficient values of the Australian hardwood species tested and published mixed species in all material orientations reveals markedly lower values for the Australian hardwood species, which highlights their comparatively slow drying rates.

The permeability, water-vapour diffusivity, and associated anisotropic ratio data obtained for messmate were extreme or did not follow typical trends compared with other species. Messmate is by far the hardest wood to dry in terms of collapse and checking drying degrades. It seems that heterogeneity and isotropy at this level correlates well with ease of drying.

Chapter 3
Wood property characterisation – Part 1

This chapter features the bulk of the published journal article "*Characterisation of viscoelastic, shrinkage and transverse anatomy properties of four Australian hardwood species*" published in Wood Material Science and Engineering, Volume 6, Issue 3, pp. 95-104 (2011), where some minor alterations have been made based on reviewers' comments.

Statement of Authorship. This work was divided as follows:

- *Mr. Adam Redman* (Candidate) wrote the majority of the article, performed the experimental procedures and proposed further experiments to characterise the messmate species wood-water relations, free of collapse degrade.
- *Dr. Henri Bailleres* assisted in the methodology and proposed the collaboration with Professor Perré to perform experiments in France.
- *Prof. Patrick Perré* directed and guided the work, designed many of the experimental methods and proposed the important wood properties required for accurate wood drying modelling.

SIGNED:

DATE:
19/8/2017

3.1 Introduction

Conventional kiln drying with controlled heating, humidity and air-flow under atmospheric pressure conditions is the primary method for drying timber in Australia [1]. In recent years, with emerging technological advancements in construction, design, computer control and less expensive materials, vacuum drying of hardwood timber (particularly in Europe and USA) has been proven in many applications to be a more economical alternative to drying using conventional methods, with similar or better quality outcomes [4]. For this reason, the Department of Employment, Economic Development and Innovation (DEEDI) purchased a 2 m^3 research vacuum kiln.

Preliminary results generated much interest from the Australian hardwood timber industry. In response, DEEDI invested in a project to establish the viability of vacuum drying technology for drying four high volume commercial Australian hardwood species with respect to drying quality, time and cost. Moreover, we recognised that a better knowledge of the material and associated drying behaviour is required to optimise the vacuum drying process in the future. Therefore, a component to develop a hardwood vacuum drying model was included in the project.

Currently, much modelling work has been conducted for softwood species due to its commercial importance and relative homogeneity between species [8, 16, 114, 115]. The complexity of the wood structure of hardwoods together with the huge variation within and between species, have resulted in limited deterministic modelling work being performed to date on these species.

As drying models require a number of physical and mechanical parameters to operate, appropriate initial parameters were chosen to gain a better understanding of the wood properties that explain the drying behaviour of Australian hardwood species and satisfy major requirements for a drying model. The challenge is to identify wood properties and characteristics that account for specific behaviour, such as collapse and surface/internal checking in Eucalypts and related species. Based on this, we measured the following parameters for each species:

1. measurement of wood anatomy characteristics using a combination of ESEM (environmental scanning electron microscope) scans and image analysis using *MeshPore* to characterise cell morphology;

2. measurement of the wood-water relationship on micro samples using a highly accurate microbalance and scanning laser micrometers to accurately measure loss of moisture content (MC) in conjunction with directional shrinkage and;

3. measurement of the viscoelastic nature in the tangential and radial directions using dynamic mechanical analysis (DMA).

The viscoelastic properties measured were the storage modulus, loss modulus and loss factor. The storage modulus describes the capacity of material to support load and thus describes the elastic component of the sample. The loss modulus describes the viscous component of the sample and is proportional to the dissipated energy. The loss factor describes the damping capacity of the sample. The variations of these parameters with temperature give an indication about the relevant temperature level used during drying.

3.2 Materials and methods

3.2.1 Materials

The species under investigation are mature native forest spotted gum *(Corymbia citriodora* Hook), blackbutt(*Eucalyptus pilularis* Sm.), jarrah(*Eucalyptus marginata* D.Don ex Sm.) and messmate (*Eucalyptus obliqua* L'Herit). We chose the species for this study based on their large range of drying characteristics. For example, spotted gum is the easiest species to dry in terms of its resistance to drying degrade, followed by blackbutt and jarrah, which are mildly susceptible to surface checking. Finally, messmate is one of Australia's hardest species to dry due to its propensity to collapse, internal and surface check. This raises the question as to why, given that these species are anatomically similar, they exhibit vastly different drying abilities. This forms the basis of this study.

3.2.2 Morphological characterisation

We cut small heartwood samples from unseasoned boards. One sample per species was carefully cut using a laboratory bandsaw to the approximate dimensions: 4 mm (radial) x 4 mm (tangential) x 20 mm (longitudinal). The samples were cut in half-lengthwise to produce two matched samples of dimension: 4 mm x 4 mm x 10 mm. We used one section for two-dimensional ESEM analysis in the radial-tangential plane and the other section to determine basic density. We analysed one image per species.

We calculated basic density by determining a sample's green volume and dry weight in accordance with *Australian and New Zealand Standard*

AS/NZS 1080.3:2000 – Timber – Methods of Test – Method 3: Density [121] using:

$$\rho_b = \frac{m_d}{V_g} \tag{3-1}$$

where ρ_b is the basic density (kg/m^3), m_d is the oven dry mass (kg), and V_g is the green volume (m^3).

The ESEM images were analysed using *MeshPore* [122]. *MeshPore* is a standalone application allowing a comprehensive Finite Element (FE) mesh to be prepared from digital microscopic images of heterogeneous and porous media, and fast measurements of the wood morphology can be calculated. Using *MeshPore*, cell lumen contours were automatically generated (*Figure 3.1*) to determine the average fibre cell wall thickness and porosity. The fibre (%) were calculated by *MeshPore* using equation 3.2:

$$\varphi_f = \frac{\sum_{j=1}^{n} A_{jf}}{A_i} \times 100 \tag{3-2}$$

where φ_f is the fibre porosity (%), A_i is the area of the fibre image (m^2), A_j is the fibre void area (m^2) of void number j and n is the number of voids in the image. The average fibre cell wall thickness (μm) was calculated by *MeshPore* using equation 4-1:

$$t_f = \frac{A_i - \sum_{j=1}^{n} A_j}{t \sum_{j=1}^{n} l_j} \tag{3-3}$$

where t_f is the average fibre thickness and l_j is the fibre void circumference of void number j.

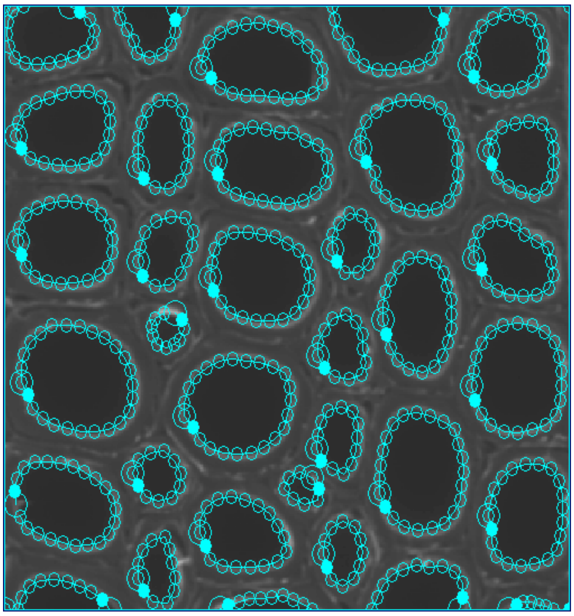

Figure 3.1 Example of automated MeshPore contours generated for blackbutt

The average minimum fibre thickness was also determined using *MeshPore* by manually drawing and measuring lines from the shortest point between adjacent cell wall/lumen interfaces (Figure 3.2).

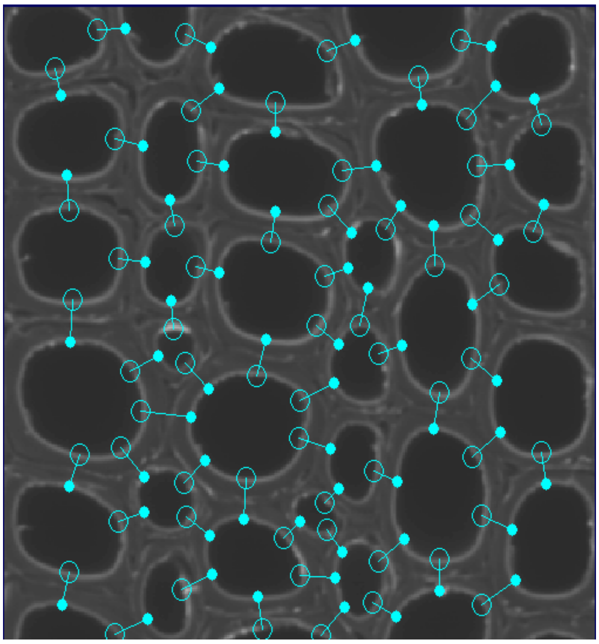

Figure 3.2 Example of manually drawn line method to determine minimum cell wall thickness for blackbutt

3.2.3 Viscoelastic characterisation

The viscoelastic behaviour of wood is critical in many fields of the wood industry such as drying, steam bending, veneer processing and gluing. It is also a critical property for characterising collapse, in particular reconditioned collapse recovery.

We performed viscoelastic tests in both the radial and tangential directions for each species. Samples cut successively from a board parallel to the longitudinal direction of the log allowed the measurement of similar radial-tangential cross sections, yielding matched samples with very similar properties (Figure 3.3). Samples were cut to approximate dimension, 40 mm x 13 mm x 2 mm using a Struers-Accutom-5™ automatic precision cut-off machine. Samples were cut under saturated conditions to minimise heating due to friction and subsequent sample drying.

Viscoelastic characterisation tests were performed using a TA Instruments DMA 2980 analyser. A single cantilever clamp was used, whereby samples were rigidly clamped at one end and fixed to a movable clamp at the other. During operation, samples were coated in 4 layers of thin 'plastic food wrap' to maintain MC above the fibre saturation point, mounted in the device and then subjected to alternate, symmetric (sinusoidal) oscillatory changes in stress/strain while undergoing changes in temperature. As collapse generally occurs in the early stages of drying above the fibre saturation point we are interested in characterising the viscoelastic relationships within this moisture content zone.

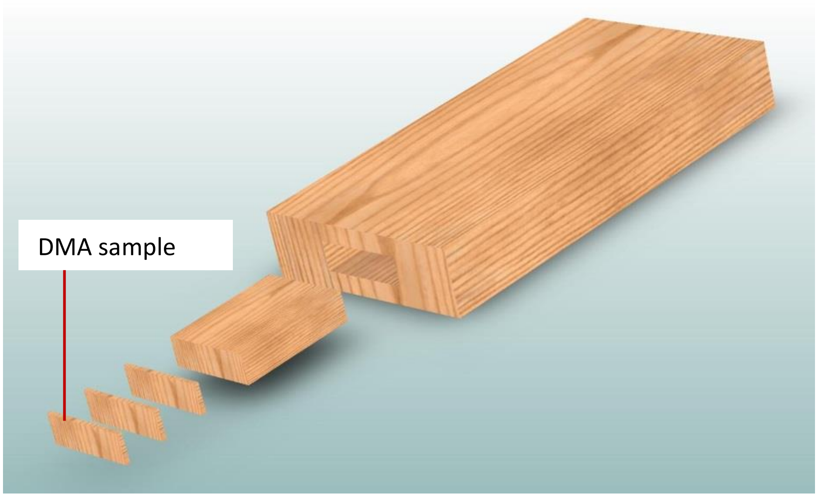

Figure 3.3 DMA sampling - example of radial sample cutting to dimension 40 mm x 13 mm x 2 mm

For each species and direction, we tested three samples. Each sample was submitted to multi-frequency temperature scans with maximum displacement amplitude of 100 µm. The temperature range for each test was 35°C to 95°C, with a heating rate of 2.0°C/minute and isothermal plateau duration of 1 minute. At each temperature increment of 5°C, the viscoelastic properties were measured under oscillatory stress at frequencies: 0.1, 1 and 10 Hz. For each frequency the viscoelastic properties of storage modulus (E'), loss modulus (E'') and loss factor (tanδ= E'/ E'') were determined.

When graphed against temperature we identify the softening or glass transition temperature as the peak of the loss factor (tanδ) curve. As measurements were made at 5°C increments, to accurately determine the temperature of the peak of the tanδ curve, a least square Gaussian function was fitted. We chose this technique due to its accuracy of fit and ease of peak extraction.

3.2.4 Wood water relations – shrinkage

We carried out wood water relationship tests on small micro-samples (1 mm thick) using specialised precision apparatus. Such thin samples are used to produce a relatively uniform MC field, thus minimising the stress field so as not to produce checks or cracks during testing.

We measured the dimensions of micro-samples using a non-contact laser system while continuously measuring the MC of samples using a highly sensitive electronic microbalance (MC2, Sartorius) with a capacity of 2 g and typical sensitivity of 0.1 μg. Two high-speed laser micrometers (Keyence, LS-5000 series) were incorporated to measure changes in the width and height of samples without contact (2 μm accuracy).

The measurement system was placed in a climatic chamber where the dry bulb temperature was held constant at 30°C. Relative humidity inside the chamber was controlled using a water bath maintained at the desired dew point temperature. A small fan ensured even temperature and humidity conditions throughout the chamber. The dew point and water temperature were measured to an accuracy of 0.1°C using a dew point analyser [123].

For each species, a small block of unseasoned material was initially prepared with the approximate dimensions: 13 mm in the tangential (T) direction, 10 mm in the radial (R) direction and 40 mm in the longitudinal direction (L). We sliced the block in the longitudinal direction using a diamond wire saw to accurately obtain 1 mm thick radial/tangential cross-sectional samples.

Prior to testing, we inserted samples into a sample support specifically designed so:

- it does not interfere with the laser beams,
- shrinkage measurements are made at the same material locations, and
- the sample is sufficiently restrained to avoid flexure while maintaining freedom to shrink (Figure 3.4).

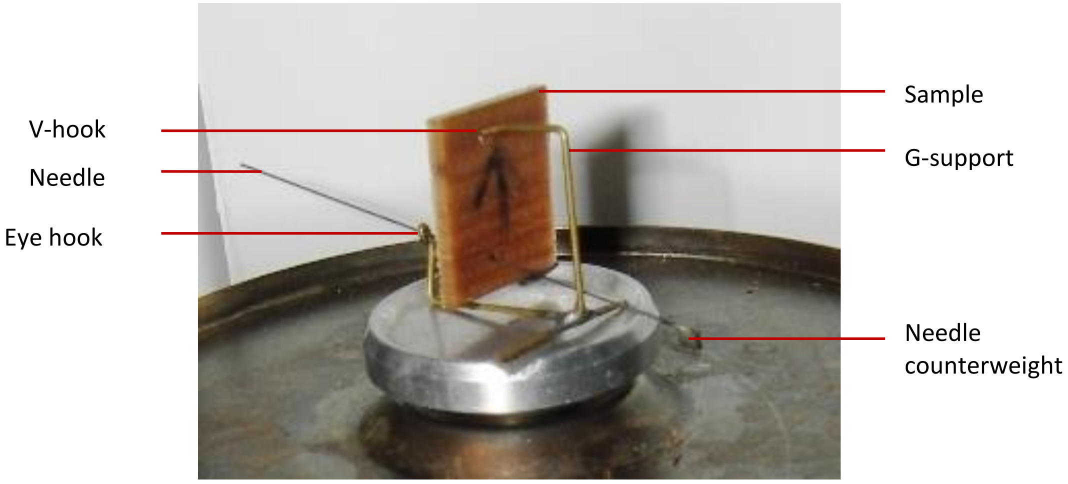

Figure 3.4 Sample in support resting on microbalance

The support is made from soldered brass. The sample is hung from a G-shaped support via a 1 mm diameter hole drilled in the upper part. The upper branch of the G-support is curved to create a V shaped hook. The V-shaped hook inhibits sample movement in the direction of the support branch to which the V-hook is connected (sample thickness direction). Rotation around the V-hook (sample width direction) is inhibited by using a needle and attached counterweight. The needle is inserted in a second hole (0.8 mm diameter) drilled in the bottom of the sample. One end of the needle is held by an eyehook at the bottom part of the G-support. The two holes are both offset from the central width of the sample, so that gravity forces the sample to rotate around the V-hook until the needle leans against the G-support. Due to friction, as a result of the needle counterweight, the sample is also blocked from rotating in the direction of the needle. Even though rotational movement of the sample is blocked in all directions, it is still free to shrink. The shrinkage is thus measured symmetrically in a given direction.

We investigated the radial and tangential shrinkage on two samples for each species. For each test, the temperature in the chamber was held constant at 30°C and the dew point temperature and relative humidity was cycled as shown in Figure 3.5.

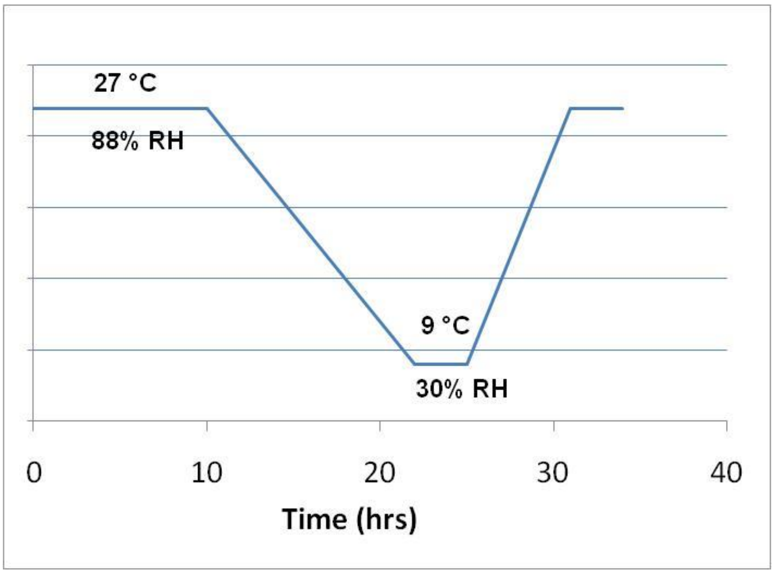

Figure 3.5 Climatic dew point and relative humidity schedule used for shrinkage tests

During each test, shrinkage, temperature and sample weight measurements were recorded at regular intervals and stored. At the end of the experiment, the sample was oven dried to determine the final MC of the sample and previous MC evolution during the test.

3.3 Results and discussion

3.3.1 Morphological characterisation

We used images taken at 800 × magnification for measurement of fibre properties using *MeshPore*. The ESEM images taken at this magnification were cropped to contain only wood fibre (Figure 3.6). Ray parenchyma and vessel cells were excluded.

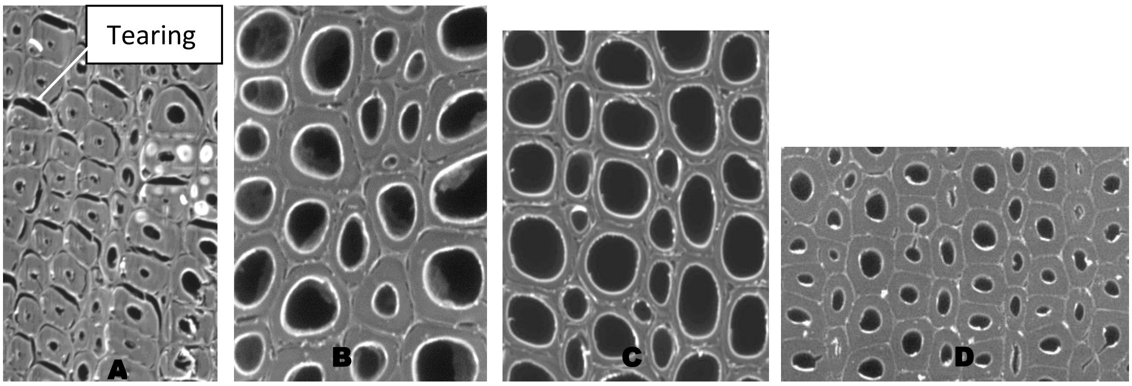

Figure 3.6 Cropped ESEM images for MeshPore (800 × mag.): spotted gum (A), jarrah (B), blackbutt (C), and messmate (D)

Table 3.1 lists the number of fibres measured, average and minimum fibre cell wall thickness, fibre porosity, and density for each species sample. Although the number of fibres investigated for each species varies, little or no influence on the measurements is presumed owing to the homogeneity of these species with respect to earlywood and latewood and their diffuse porous nature. As the calculated cell wall thickness using *MeshPore* is based on the global sum of contours and tissue area, individual values are not calculated which does not allow standard deviations to be determined.

Table 3.1 Average cell wall thickness (using MeshPore and manual methods), fibre porosity and density for each species in the unseasoned condition (n=1)

Species	No. fibres	Fibre cell wall thickness (µm) – 2 methods MeshPore	Manual method	Fibre Porosity (%)	Density (kg/m³)
Spotted gum	56	16.4	5.4	5.4	833
Jarrah	26	5.0	2.8	31.4	721
Blackbutt	34	4.3	2.6	43.8	681
Messmate	52	8.7	4.2	13.4	418

We measured distinct fibre porosity and fibre cell wall thickness differences between species, as visually observed from ESEM images. The average fibre cell wall thickness generated for each species is approximately double the minimum cell wall thickness measured, except for spotted gum where the average value is nearly triple the minimum measured. The automated average calculations are subject to errors for wood cells with very small lumens and thick cell walls, and cells that are irregular in shape, as opposed to perfectly round cells, which are heavily dependent on the length of lumen contours. Spotted gum clearly has a much smaller fibre lumen/fibre area ratio (Figure 6A). Tearing of the middle lamella of the spotted gum sample also contributed to the generation of average cell wall thickness errors when generating average cell wall thickness. Apart from this anomaly, the results are consistent with published data [124] which suggests the average fibre cell wall thickness for wood generally ranges from around 3 µm to 8 µm.

Except for messmate, species density decreases with decreasing fibre cell wall thickness and increasing fibre porosity. Although fibre cell wall thickness and porosity plays an important role in the overall density of wood, the frequency and cell wall thickness of ray parenchyma cells, and the frequency and size of hardwood vessels also contribute [124].

3.3.2 Viscoelastic characterisation

Figure 3.7 shows a typical example of the storage modulus and loss factor as a function of temperature at different frequencies, shown for messmate in the tangential direction.

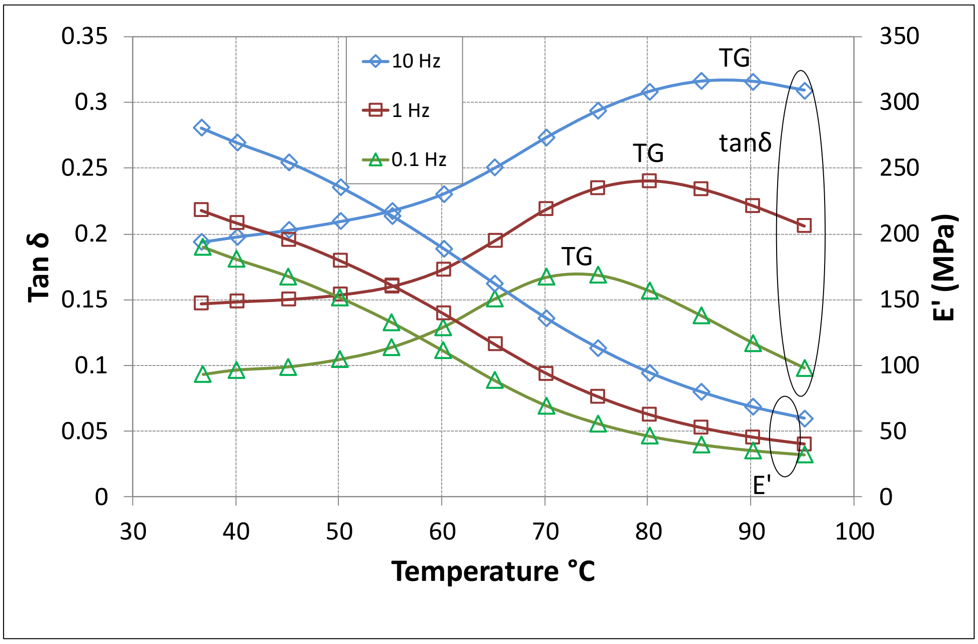

Figure 3.7 Viscoelastic characterisation for messmate in the tangential direction. TG= glass transition temperature; E′ = storage modulus

These curves uncover the typical characteristics of the viscoelastic behaviour of wood on this temperature range. The storage modulus decreases with increasing temperature and a softening transition appears between 70-100°C corresponding to in situ lignin relaxation [125]. The storage modulus curves are perfectly staggered. As for all viscoelastic solid materials the modulus of wood increases with frequency due to time dependant molecular relaxation, and the glass transition temperature (peak of tanδ curves) shifts to higher values as the frequency increases [126]. Furthermore, the glass transition temperature appears to approach an asymptotic limit with decreasing frequency, suggesting that the viscoelastic properties measured at lower frequencies are more representative of static material.

For some species and directions, particularly at higher frequencies, we were unable to determine the glass transition temperature as it occurs somewhere over 95°C, which was the maximum temperature tested.

The storage modulus was clearly different between the radial and tangential directions regardless of the frequency, temperature and species (Figure 3.8). This is consistent with findings reported by Placet *et al* [126]. For the species studied, spotted gum was the stiffest, followed in order of reducing stiffness by, blackbutt, jarrah and messmate. These results follow the same trend of published static bending evaluation of the modulus of elasticity for these species [117]. The storage modulus was consistently larger in the radial direction than the tangential direction for each species; however, the E'_R/E'_T ratio differed between species (Table 3.2), more so for messmate, possibly due to anatomical variations.

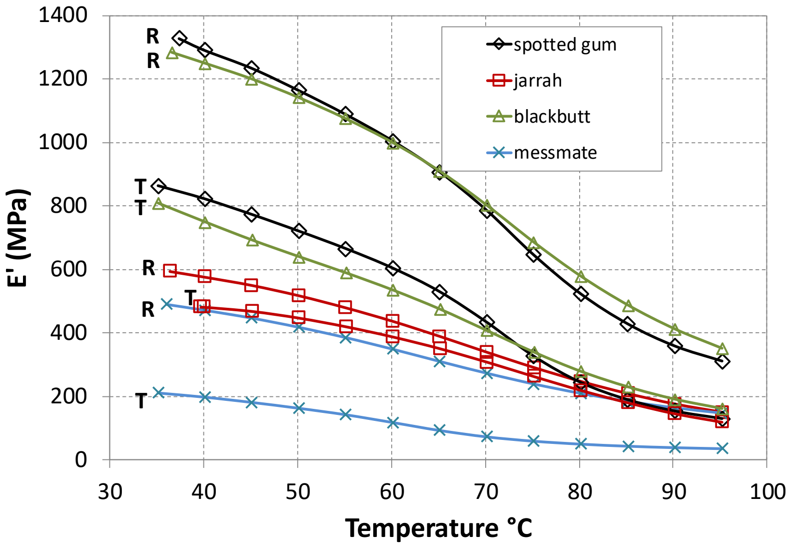

Figure 3.8 Storage modulus evolution in the tangential and radial directions for each species (frequency 0.1 Hz). E′ = storage modulus

Table 3.2 Summary of viscoelastic properties for each species, TG= glass transition temperature; E′ = storage modulus

	Spotted gum		Jarrah		Blackbutt		Messmate	
	R	T	R	T	R	T	R	T
Tg (°C)								
0.1 Hz	87	87		90	89	87	80	73
1 Hz							91	81
10 Hz								87
E' (MPa) (0.1 Hz, 35°C)								
Mean	1400	849	687	504	1302	752	485	200
Range	1454-1327	877-805	746-594	531-481	1414-1209	808-680	497-467	211-190
SD	66	38	82	25	104	65	16	10
E'R/E'T	1.65		1.36		1.73		2.42	

Regardless of the wood species and frequency of test, the storage modulus determined from 35°C to 95°C decreased less in the radial direction than the tangential direction (Table 3.3). Additionally, the percentage of storage modulus loss R/T ratio was much less for messmate, compared with the other species.

Table 3.3 Storage modulus values at 35°C and 95°C for each species (E′ at 0.1 Hz)

		E' at 0.1 Hz (MPa)				
Species	Direction	35°C	95°C	E'_{35}/E'_{95}	Loss (%)	Loss R/T ratio
Spotted gum	R	1400	318	4.4	77	0.91
	T	849	128	6.6	85	
Jarrah	R	687	167	4.1	76	1.00
	T	504	121	4.2	76	
Blackbutt	R	1302	349	3.7	73	0.92
	T	752	157	4.8	79	
Messmate	R	485	147	3.3	70	0.84
	T	200	34	5.9	83	

Figure 3.9 shows the loss factor as a function of temperature (at 0.1 Hz) in the radial and tangential directions. The average glass transition

temperatures for each species and test frequency are provided in Table 3.2. The results show a clear difference in loss factor between the radial and tangential directions, where the peak value of tanδ was greater in the radial than the tangential direction for all species. Furthermore, the glass transition temperature varied greatly between species with the lowest recorded in the tangential direction for messmate (73.2°C, at 0.1 Hz) and the highest in the radial direction for jarrah (> 95°C, all frequencies).

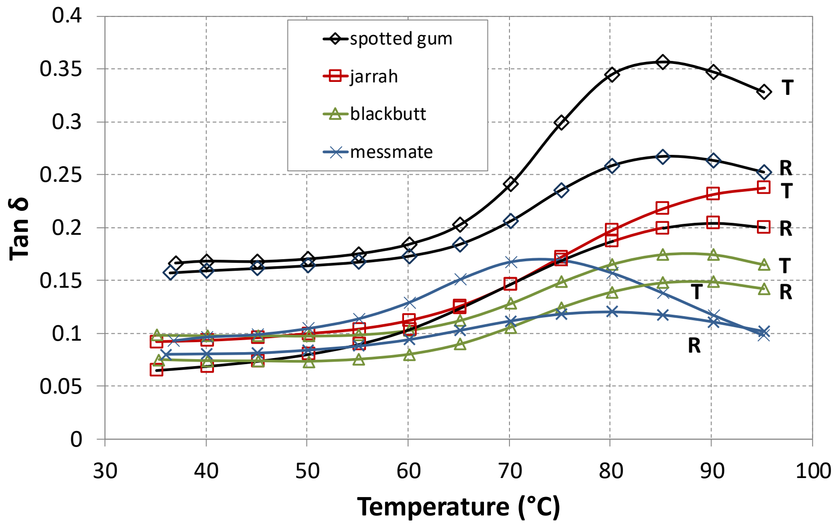

Figure 3.9 Loss factor versus temperature for each species in radial and tangential directions (frequency 0.1 Hz)

The glass transition temperature was the same or greater in the radial direction than the tangential direction at an oscillation frequency of 0.1 Hz for spotted gum, blackbutt jarrah and messmate and at 1 Hz for messmate by varying amounts. For all other circumstances, the same comparison cannot be made owing to the glass transition temperature occurring outside of the experimental temperature range. A similar trend was observed by Placet *et al* [126] who concluded that the internal friction is greater in the radial direction, likely due to enhanced rigidity caused by the presence of radially aligned ray cells.

The viscoelastic measurements overall revealed many differences concerning the rheological behaviour of wood, depending on the species and anatomical direction. The greatest influence is caused by the molecular structure of elemental wood components within the cell wall, which influence the softening properties. In the temperature range observed, the viscoelastic wood behaviour largely reflects the properties of lignin. To a lesser extent, the microfibril angle of the cell wall layers may also hold influence [126].

3.3.3 Wood water relations - shrinkage

For each species, shrinkage versus MC curves were plotted as illustrated in Figure 3.10 and Figure 3.11. Note that the data defines a very accurate curve during the test period as the adsorption/desorption shrinkage closely follows the same curve (low MC tail of the graph). Observation of the curve distinguishes two different phases:

- the removal of free water with minimal shrinkage, and
- a noticeable shrinkage phase, denoting the removal of bound water with a linear relationship with MC.

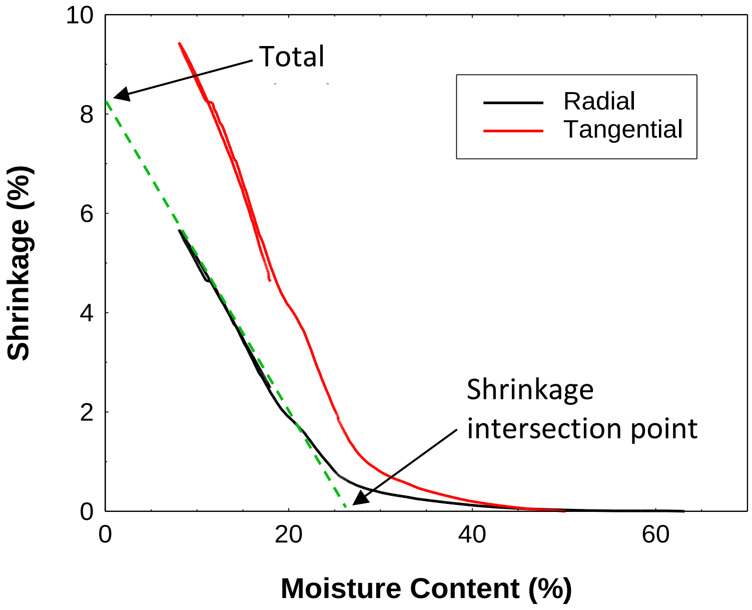

Figure 3.10 Typical shrinkage curve shown for blackbutt

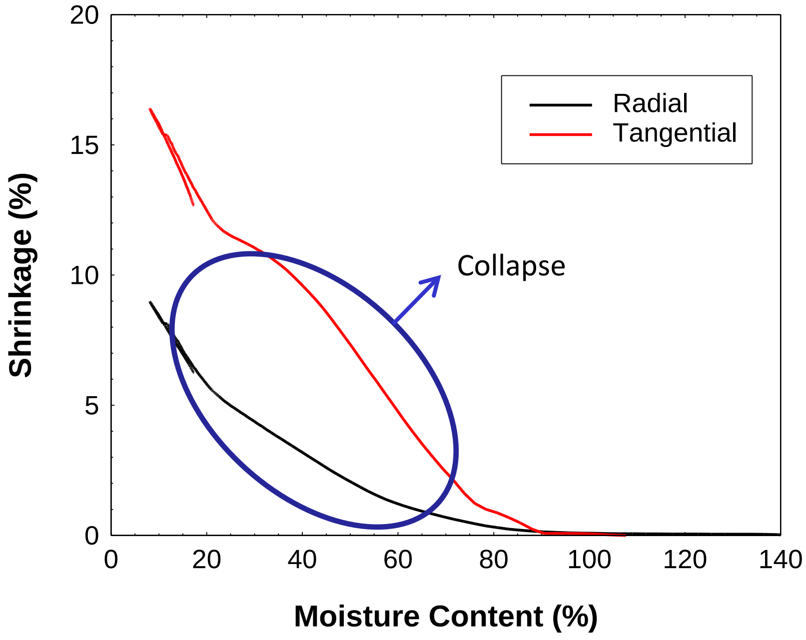

Figure 3.11 Shrinkage curve showing collapse for messmate

Similar plots resulted for all species except messmate, which showed abnormal shrinkage occurring at high moisture content due to cell collapse during free water removal (Figure 3.11).

Messmate is a renowned collapse prone species [117]. The radial and tangential shrinkage begins very soon after drying and increases abnormally up to 20-40 % MC. At this point, the collapse shrinkage slows down as the sample reaches the bound water domain. In the domain of bound water, normal shrinkage takes place (< 20 % MC). Only this part of the shrinkage is recovered when the sample re-absorbs water. The messmate collapse results observed are consistent with results observed by Perré [123] for *Eucalyptus gundal* (*Eucalyptus gunnii x dalrympleana*). Collapse seems to occur continuously along the desorption range.

It may be possible to avoid collapse shrinkage during shrinkage tests for this species by cutting thinner R-T sections in the longitudinal direction. Clarke *et al*. [127], observed most eucalypt species have short fibres around 0.6-0.8 mm long. Thus, by reducing the dimension of samples to less than 0.6 mm thickness, the majority of wood fibres will be severed. A cut fibre will not readily collapse as tension of the cell wall will not be set up if the ends of the fibres are not whole [128].

The shrinkage intersection point and total shrinkage were calculated from the shrinkage versus MC curves by subtending the linear portion of the curve, in the bound water/shrinkage phase, until it intersects the x and y axis (Figure 3.10). We calculated the shrinkage at 12%, a common published quantification of shrinkage, from the equation of the subtended line. Table 3.4 Shrinkage data measured and published per species provides the total shrinkage, intersection point, shrinkage at 12 %, and the radial/tangential (R/T) shrinkage ratios for each species. Published intersection point [129] and 12% MC shrinkage values [117] are also included.

For messmate samples, we could not calculate the total shrinkage and intersection point due to the presence of atypical collapse shrinkage. Shrinkage measurements were indeterminate for the second spotted gum sample in the tangential direction, due to abnormal sample movement during the test. No published intersection point values were available for jarrah or messmate.

Table 3.4 Shrinkage data measured and published per species

		Intersection point (%)				Total shrinkage (%)		Shrinkage at 12 % MC					
		Measured		Budgen (1981)				Measured			Bootle (2005)		
Sample #	Species	R	T	R	T	R	T	R	T	R/T	R	T	R/T
1	Spotted gum	23.6	25.9	21.4	24.5	8.6	8.8	4.4	4.9	0.90	4.5	6.0	0.75
2	Spotted gum	24.4	N/A			8.4	N/A	4.4	N/A	N/A			
3	Spotted gum	24.5	23.0			8.3	8.6	4.5	5.2	0.87			
1	Jarrah	29.0	34.7	-	-	8.2	11.9	4.8	7.8	0.62	5.0	7.5	0.67
2	Jarrah	26.0	34.6			8.4	13.4	4.7	8.9	0.53			
1	Blackbutt	24.5	31.8	25.1	31.2	8.5	12.6	4.5	7.9	0.57	4.0	7.0	0.57
2	Blackbutt	25.2	30.6			8.4	12.1	4.4	7.3	0.60			
1	Messmate	N/A	N/A	-	-	N/A	N/A	N/A	N/A	N/A	3.5	6.5	0.54
2	Messmate	N/A	N/A			N/A	N/A	N/A	N/A	N/A			

Measured intersection point, total shrinkage and 12% MC shrinkage are consistent within species providing good repeatability. Published intersection point and 12% MC shrinkage values are consistent with measured data. Shrinkage values and R/T ratios vary greatly between the tangential and radial directions as expected. Moreover, shrinkage values between species differ due to variations in physical and chemical properties. It is interesting to note that the measured and published R/T shrinkage ratios at 12 % MC are inversely proportional to a species propensity to collapse. However, the lower R/T ratio experienced for collapse prone species may actually be due to partial collapse occurring during testing.

Table 3.5 Qualitative results comparison

Species	Density	Stiffness	Fibre thickness	Fibre porosity	Total radial shr.	Total tangential shr.	Glass transition temp.	Collapse shr. observed
Spotted gum	high	high	high	low	high	medium	medium	no
Jarrah	medium	medium	low	high	high	high	high	no
Blackbutt	medium	med.-high	low	high	high	high	medium	no
Messmate	low	low	medium	medium	N/A	N/A	low	yes

3.4 Conclusions

Characterisation of viscoelastic, shrinkage and transverse anatomy properties were achieved for four Australian hardwood species for input into a micro and macro scale vacuum drying model.

For comparative purposes, the main results are summarised in Table 3.5, expressed as qualitative adjectives (comprehensive measurements are available in the core of the paper). Fibre cell wall thickness and porosity were realised indicating clear differences between these species. Results suggested that characterisation of the entire cross-sectional cellular morphology (including vessels) is required to determine linkages between the properties measured in this study and the relevant drying characteristics for each species.

Viscoelastic properties of wood, in terms of stiffness, internal friction and glass transition temperature were considerably different in the radial and tangential directions within and between species. We found the viscoelastic properties measured at lower frequencies to be more representative of static material.

The highly accurate, dynamic method of determining shrinkage used was unable to characterise radial and tangential shrinkage for messmate due to the existence of collapse shrinkage. To characterise the wood-water relations of this species, free of collapse, we propose that thinner sample sections (in the R-T plane) should be used.

It was of much interest that the data obtained for messmate was generally extreme or did not follow typical trends compared with the other species. Messmate is by far the hardest to dry compared in terms of collapse and checking. It seems that heterogeneity and anisotropy at this level is correlated with ease of drying, although more investigations are required to quantify this.

Chapter 4
Wood property characterisation – Part 2

This chapter features the bulk of the published journal article "*Characterisation of wood-water relationships and transverse anatomy and their relationship to drying degrade*" published in Wood Science and Technology, Volume 50, Issue 4, pp. 739-757 (2016), where some minor alterations have been made based on reviewers' comments.

Statement of Authorship. This work was divided as follows:

- *Mr. Adam Redman* (Candidate) wrote the majority of the article, performed the experimental procedures and proposed experiments to characterise the messmate species wood-water relations, free of collapse degrade.
- *Dr. Henri Bailleres* assisted in the methodology and proposed the collaboration with Professors Turner and Perré to perform experiments in France.
- *Prof. Ian Turner* was instrumental in developing the drying model and assisted in determining characteristic wood properties required to model the drying process.
- *Prof. Patrick Perré* directed and guided the work, designed many of the experimental methods and proposed the linkages between wood property measurements and degrade propensity.

SIGNED:

DATE:

19/8/2017

4.1 Introduction

Timber drying concerns the removal of water from wood before its end use and consists of a complex system of intricate physical and mechanical processes. For industry, the desired outcome is to dry wood in the fastest time possible, while minimising cost and maximising quality. However, due to the complexity of wood drying, these three aims are not independent; they influence each other and must be balanced to optimise the drying process. Drying time is usually restricted by the desired level of acceptable dried quality.

Dried quality includes the variation in final moisture content within and between wood boards, residual drying stress, distortion, wood cell collapse deformation, and external or internal tearing of wood tissue in the form of splits or checks. Many eucalypt species, particularly those of low density, are prone to collapse deformation, splitting and checking.

When wood dries, its exterior dries more rapidly than the interior to form a moisture content gradient. Once the exterior layers dry below the fibre saturation point, below which wood starts to shrink, and while the interior is still saturated, stresses are set up because the shrinkage of the outer layers is restricted by the wet interior (this is known as differential shrinkage). The wood tissues rupture and consequently splits and cracks occur if these stresses across the grain exceed the strength. Collapse describes the deformation of single cells, due to capillary forces during removal of free water, resulting in larger than normal levels of shrinkage and irregular deformation of timber surfaces. Different species are more prone to certain forms of drying induced degrade than others depending on a number of factors mostly relating to wood anatomy, chemistry and growth conditions.

The successful control of drying defects in a drying process consists in maintaining a balance between the rate of evaporation of moisture from the surface and the rate of outward movement of moisture from the interior of the wood. One of the most successful ways of controlled wood drying is by kiln drying.

Conventional kiln drying with controlled heating, humidity and air-flow under atmospheric pressure conditions is the primary method for drying timber in Australia [1].In recent years, with emerging technological advancements in construction, design, computer control and less expensive materials, vacuum drying of hardwood timber(particularly in Europe and USA) has been proven in many applications to be a more economical alternative to drying using conventional methods, with similar or better quality outcomes [4]. For this reason, the Department of Agriculture, Fisheries and Forestry (DAF) purchased a 2 m3 research vacuum kiln.

Preliminary results from vacuum drying trials generated much interest from the Australian hardwood timber industry. In response DAF invested in a project to establish the viability of vacuum drying technology for drying four high volume commercial Australian hardwood species with respect to drying quality, time and cost. Moreover, it was recognised that a better knowledge of the material and associated drying behaviour is required to fully optimise the vacuum drying process in the future [130]. Therefore, a component to develop a hardwood vacuum drying model was included in the project. The full details of the modelling and simulation work will be reported in a future paper.

Currently, much modelling work has been conducted for softwood species due to its commercial importance, and relatively simple anatomical pattern [6, 8, 16, 115]. The most accurate deterministic model to date encompasses multiscale and multiphysics descriptions of drying phenomena for softwoods [17]. The proposed modelling development for the vacuum drying of hardwood species will take advantage of the existing model *TransPore* [7, 16] used to predict the drying behaviour of softwoods and drying of other porous media, such as concrete. The complexity of the wood structure of hardwoods together with the huge variation within and between species, have resulted in limited deterministic modelling work being performed to date on these species. Additionally, limited data is currently available for vacuum drying eucalypt species.

As drying models require a number of physical and mechanical parameters to operate, appropriate initial parameters have been chosen to gain a better understanding of the wood properties that explain the drying behaviour of Australian hardwood species and satisfy major requirements for a drying model. The challenge is to identify wood properties and characteristics that account for specific behaviour, such as collapse and surface/internal checking in eucalypts and related species. These phenomena are quite difficult to assess as they result from an intricate coupling between the anatomical level, and even the ultra-structural level, and the macroscopic level. Based on this premise, the following parameters were previously measured for each species as presented by Redman et al. [30]:

1. Wood anatomy characteristics, particularly wood fibre cell wall thickness and porosity (in the radial-tangential cross-section);
2. Wood-water relationship on micro samples particularly

shrinkage characteristics, and;

3. Permeability and diffusivity
4. Viscoelastic nature in the tangential and radial directions using dynamic mechanical analysis (DMA).

On average, the anatomy of Australian hardwood species is made mostly of fibres and vessels; approximately 75%. Ray and axial parenchyma cells make up the rest at approximately 15 and 10%, respectively [131]. The ratio of fibres to vessels, on average for Australian hardwoods is 2:1 [131]. The results of Redman *et al.* [30] characterised wood porosity of the species of interest using only measurements of fibre properties. However, due to the substantial proportion of vessels, characterisation of the entire cross-sectional cellular morphology, including vessels, is required to accurately determine wood porosity for, precise drying modelling, linkages between morphological properties and the relevant drying characteristics for each species.

Additionally, Redman *et al*. [30] were unable to characterise radial and tangential shrinkage for *E. obliqua* in their study, using 1mm thick cross-sectional samples, due to the existence of collapse shrinkage. The most widely accepted theory of collapse occurrence was proposed by Tiemann [132], who attributed collapse to the hydrostatic tensions in the fibre cell lumina caused by water removal. Essentially, when drying above the fibre saturation point, free capillary water in the cell lumina is withdrawn through small cell wall openings (pits) forming a meniscus at the air-water interface thus inducing a hydrostatic tension. If this hydrostatic tension exceeds the compressive strength of the cell wall, the cell collapses. Kauman [133] postulates that thin cross-sections, thinner than the minimum fibre length, do not collapse since each fibre has been severed and tensions cannot develop. The average fibre length for *E. obliqua* is reportedly 1.15 mm, ranging from 1.04 to 1.27 mm [134], measured on 20 heartwood samples. The existence of collapse shrinkage in 1 mm thick samples observed by Redman *et al*. [30], suggests that the minimum fibre length was less than the minimum reported by Dadswell [134], the measurement of which was outside the scope of this work.

Based on previous findings and postulations, the following parameters were measured for each species and are presented in this paper:

1. Wood anatomy characteristics, particularly porosity as a combination of fibre and vessel porosity, using a combination of ESEM (environmental scanning electron microscope) scans and image analysis using *MeshPore*, which is a vector-based software package developed by Perré [135] to characterise cell morphology and;
2. Wood-water relationship on thin sections of*E. obliqua* micro samples (less than 1mm) with the aim of characterising 'collapse free' shrinkage, using a highly accurate microbalance and scanning laser micrometers to accurately measure loss of moisture content (MC) in conjunction with directional shrinkage.

Wood-water relationship measurements also allow the calculation of sorption/desorption curves, the mathematical description of which is used in modelling. The sorption hysteresis effect, i.e. different wood equilibrium moisture content (EMCs) in desorption and adsorption for the same relative humidity, is well known [46]. However, quantitative sorption isotherms in the form of tables or analytical correlations, are usually given as the average of the desorption and adsorption curves. Consequently, most drying simulation models use these average curves, and do not take into account the sorption hysteresis phenomenon [54].

Salin [54] proposed that traditional models that use average sorption curves (derived across a range of species) are problematic because different species have different sorption isotherms. Therefore, species specific sorption isotherms, including the sorption hysteresis phenomenon, of which drying models are very sensitive, should be included in drying models as an improved tool in practical applications. For this reason, we present in this paper sorption isotherms calculated from the results of Redman *et al*. [30] for spotted gum (*Corymbia citriodora* Hook.), blackbutt(*Eucalyptus pilularis* Sm.) and jarrah(*Eucalyptus marginata*, D.Don ex Sm.) and from the results of this paper for messmate(*Eucalyptus obliqua* L'Herit.).

We chose these species for this study based on their large commercial volume, value and range of drying characteristics and wood properties. For example spotted gum is the easiest species to dry in terms of resistance to drying degrade and has the highest basic density (BD) of 1000 kg/m^3 [117], followed by blackbutt (710 kg/m^3 BD) and jarrah (670 kg/m^{3}BD) which are mildly susceptible to surface checking. Finally, messmate is one of Australia's hardest species to dry due to its propensity to collapse, internal and surface check and has the lowest BD of 489 kg/m^3.

The basis of this study consists of accurately quantifying a number of morphological and wood-water relation variables necessary to develop a precise deterministic hardwood vacuum drying model using the aforementioned species as case studies. Additionally, linkages between these and previously measured properties and the susceptibility for drying induced degrade to occur between the species are observed.

4.2 Materials and methods

We selected material for this study from concurrent vacuum drying studies. These trials indicated that for any given species, the median density board most closely aligned to the average drying rate during a drying trial [20]. Therefore, for each species, we selected the board having the median basic density from a quantity of 100 samples to perform morphological characterisation and investigate wood water relations. Figure 4.1 shows an example of the typical normal (calculated using the Shapiro-Wilk test) density distribution histogram for messmate.

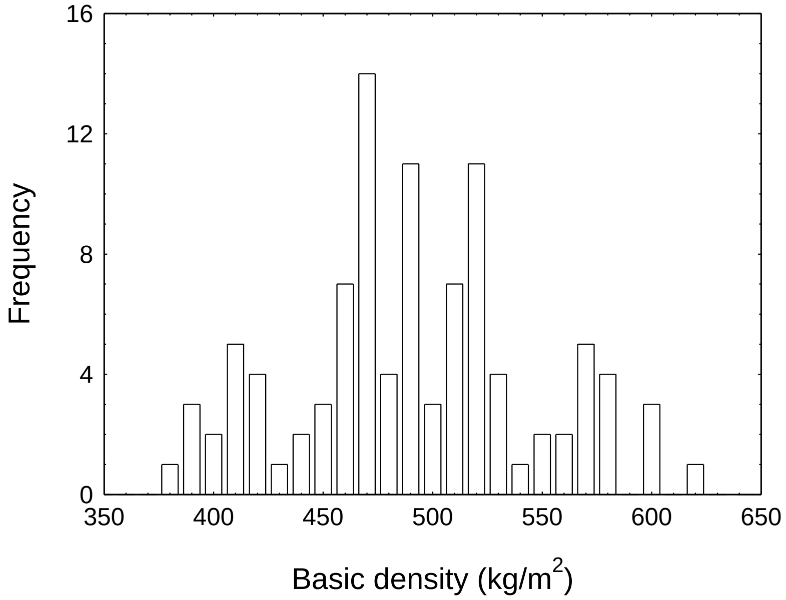

Figure 4.1 Density distribution histogram example for messmate

4.2.1 Morphological characterisation

For each species, we captured fibre morphology using an FEI Quanta 200 ESEM microscope with a beam voltage of 12.2 kV and vacuum pressure of 12 mbar. Vessel morphology was captured using a Zeiss Axioplan stereo optical microscope, using transmitted light, fitted with a monochrome digital camera.

We cut small heartwood samples from unseasoned boards. One sample per species was carefully cut using a laboratory bandsaw to the approximate dimensions: 4 mm (radial) x 4 mm (tangential) x 20 mm (longitudinal). The samples were cut in half-lengthwise to produce two matched samples of dimension: 4 mm x 4 mm x 10 mm. Samples were soaked in water at room temperature for at least 24 hours, before further processing, to soften the wood tissue prior to image surface preparation. Radial/tangential plane surfaces were prepared for ESEM imaging using a precision MICROM HM 440™ sledge/sliding microtome. We used one section for microscopic analysis in the radial-tangential plane and the other to determine basic density. One image was analysed per species. We should note that the earlywood and latewood variation is not high in these species as they are all diffuse porous.

Images taken at 700 × magnification were used for measurement of fibre properties (Figure 4.2) and images taken at 50 x magnification were used for measurement of vessel properties (Figure 4.3) using *MeshPore* [135]. The fibre ESEM images were cropped to contain only wood fibres excluding ray parenchyma and vessel cells. *MeshPore* is a standalone application allowing a comprehensive Finite Element (FE) mesh to be prepared from digital microscopic images of heterogeneous and porous media, and fast measurements of the wood morphology can also be calculated. Using *MeshPore*, fibre and vessel lumen contours were automatically generated to determine the average fibre cell wall thickness, fibre, vessel and total porosities (Figure 4.4).

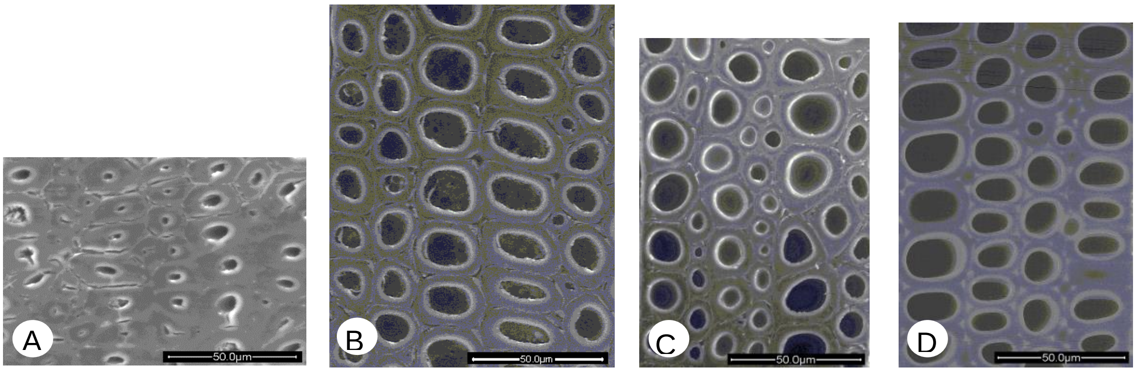

Figure 4.2 Cropped ESEM images for fibre morphology analysis: spotted gum (A), jarrah (B), blackbutt (C), and messmate(D)

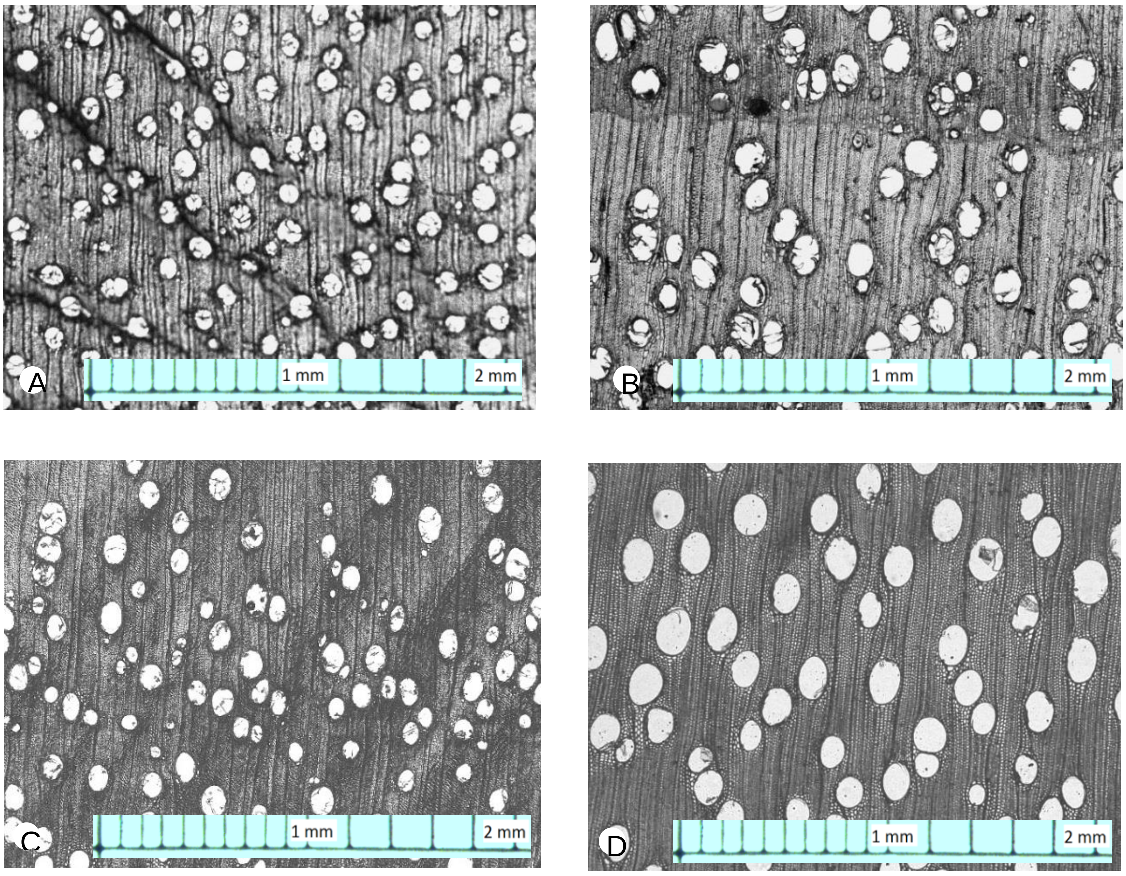

Figure 4.3 Optical microscope images for vessel morphology analysis: spotted gum (A), jarrah (B), blackbutt (C), and messmate(D)

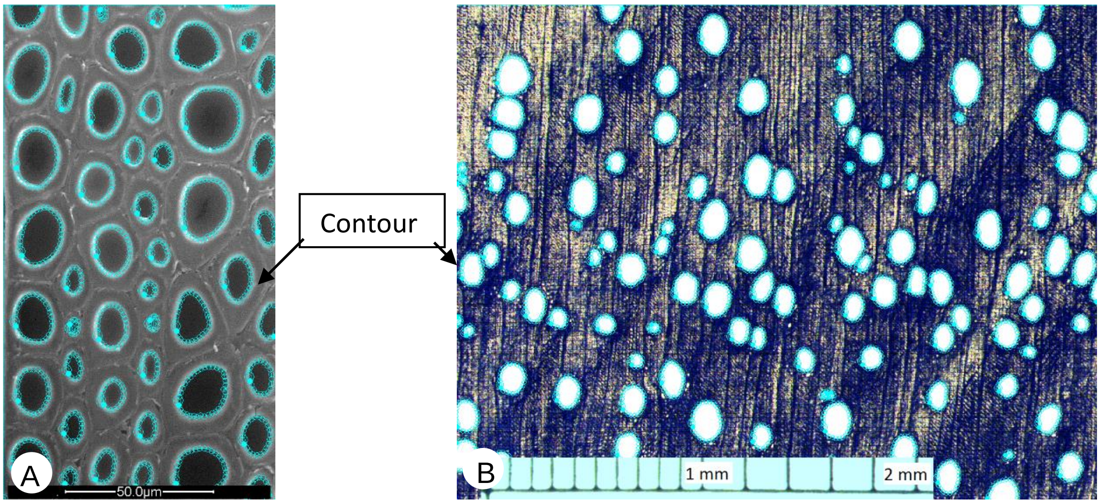

Figure 4.4 Example of automated MeshPore contours generated for E. pilularis fibres (A). and vessels (B)

The average fibre cell wall thickness (µm) was calculated by *MeshPore* using equation 4-1:

$$t_f = \frac{A_i - \sum_{j=1}^{n} A_j}{t\sum_{j=1}^{n} l_j} \qquad (4\text{-}1)$$

where t_f is the average fibre thickness, A_i is the area of the fibre image (m^2), A_j is the fibre void area (m^2) of void number j, n is the number of voids in the image and l_j is the fibre void circumference of void number j.

Equation 4-1assumes that the surface fraction of the solid phase is equal to the averaged cell wall thickness multiplied by the total contour length. As the cell walls have a closed contour rather than being flat, the exact formula should use an averaged contour, somewhere between the lumen contour and the contour of the middle lamella. Using the lumen contour is simpler and more reproducible. However, we have to keep in mind that the error due to this simple formula is negligible only when the cell wall thickness is small compared to the lumen diameter.

The fibre or vessel porosities (%) were calculated by *MeshPore* using equation 4-2:

$$\varphi_x = \frac{\sum_{j=1}^{n} A_{jx}}{A_i} \times 100 \qquad (4\text{-}2)$$

where $x$represents either fibres (f) or vessels (v), φ_x is the porosity (%). For such a dual-scale porous structure, the total porosity is calculated as the vessel porosity plus the fibre porosity inside the remaining volume using equation 4-3.

$$\varphi_t = \varphi_f + (1 - \varphi_f)\varphi_v \qquad (4\text{-}3)$$

The density was calculated using total porosity to determine if density can be predicted using only this parameter. The formula uses the oven dried density of wood tissue, suggested to be constant for all wood species, the value of which is reported to be approximately 1500 kg/m3 [21]. We use equation 4-4 to calculate density:

$$\rho_{calc} = \rho_{wt}(1 - \phi_t)_v \qquad (4\text{-}4)$$

where ρ_{calc} is the calculated density, ρ_{wt} is the density of wood tissue (1500 kg/m^3).

4.2.2 Wood-water relations

Wood water relationship tests were carried out on 2 mm, 1 mm and 0.5 mm longitudinally thick micro-samples of messmate using specialised precision apparatus [123]. We prepared such thin samples, using a precision diamond wire saw, producing a relatively uniform MC field, thus minimising the stress field so as not to produce checks or cracks during testing. Such small thicknesses are also needed to avoid or at least reduce collapse.

During testing, the dimensions of micro-samples were measured using a non-contact laser system while continuously measuring the MC of samples using a highly sensitive electronic microbalance (MC2, Sartorius) with a capacity of 2 g and typical sensitivity of 0.1 μg. Two high-speed laser micrometers (Keyence, LS-5000 series) were incorporated to measure changes in the width and height of samples without contact (2 μm accuracy and 0.3 μm reproducibility).

The measurement system was placed in a climatic chamber where the dry bulb temperature is held constant at 30°C. Relative humidity inside the chamber is controlled using a water bath maintained at the desired dew point temperature. A small fan ensured even temperature and humidity conditions throughout the chamber. Using a dew point analyser, the actual dew point of the chamber was checked to correspond to the water temperature to an accuracy of 0.1°C [123].

We prepared a small block of unseasoned material with the approximate dimensions: 13 mm in the tangential (T) direction, 10 mm in the radial (R) direction and 40 mm in the longitudinal direction (L). The block was sliced in the longitudinal direction using a diamond wire saw to accurately obtain radial/tangential cross-sectional samples of the required thickness.

Prior to testing, we inserted samples into a sample support specifically designed so (refer to [123] for further detail):

- it does not interfere with the laser beams,
- shrinkage measurements are made at the same material locations, and
- the sample is sufficiently restrained to avoid flexure while maintaining freedom to shrink (Figure 4.5).

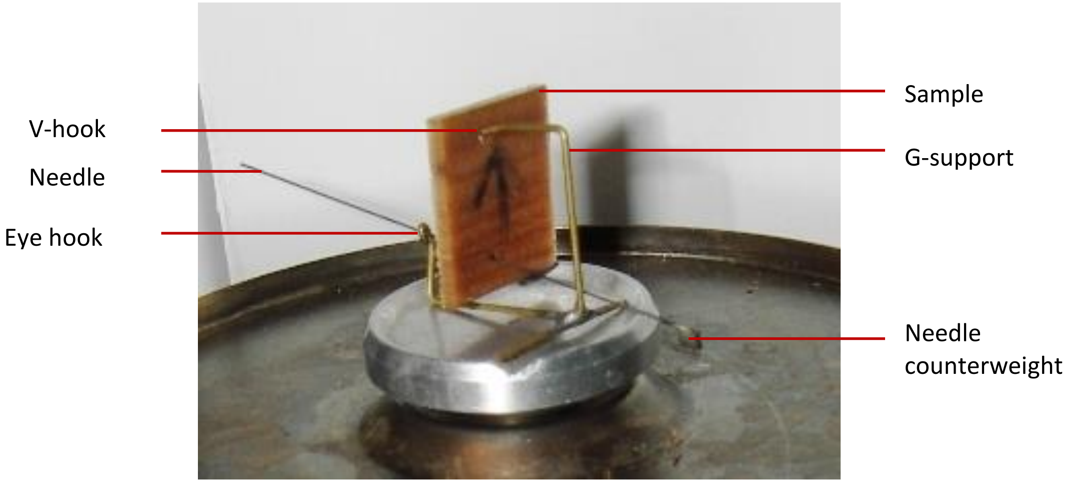

Figure 4.5 Sample in support resting on microbalance

We measured radial and tangential shrinkage on two samples for each sample thickness (2 mm, 1 mm and 0.5 mm). For each test, the temperature in the chamber was held constant at 30°C and the dew point temperature and relative humidity was cycled as shown in Figure 4.6. The corresponding relative humidity in the chamber isalso depicted in this graph.

During each test, shrinkage, temperature and sample weight measurements were recorded at regular intervals and stored. At the end of the experiment, we oven dried the sample to determine its final MC and previous MC evolution during the test.

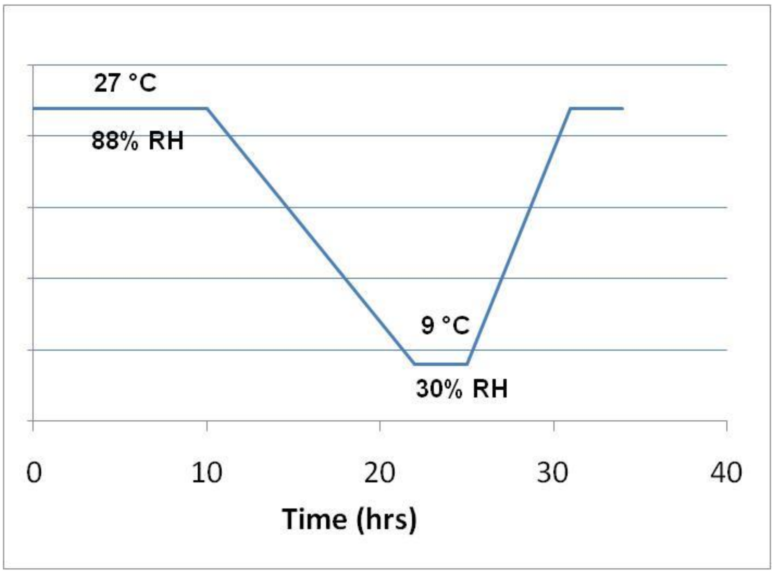

Figure 4.6 Climatic schedule used for shrinkage tests

We made investigations of sample MC versus surrounding relative humidity (RH) to observe the sorption/desorption characteristics and hysteresis for each species. Based on previous work conducted by Perré [123], the tests reported here are considered to be quasi-static in the desorption and adsorption phases. The length of time between each test set point (Figure 4.6) combined with the thin sample sections, is sufficient for the system to remain close to internal equilibrium to provide an approximation of a true desorption/sorption isotherm. Then equation 4-5 is fitted to the desorption/sorption data in the least squares sense by solving for c_1 and c_2 as reported by Perré and Turner [74]:

$$\frac{P_v}{P_{vs}} = 1 - \exp(-c_1 A - c_2 A^2) \qquad (4\text{-}5)$$

where $A = X_b / X_{fsp}$, c_1 and c_2 are constants, P_v is the vapour pressure of air (Pa), P_{vs} is the saturated vapour pressure of air, X_b is the wood MC (%), X_{fsp} is the MC (%) at fibre saturation point (FSP). FSP is calculated by the shrinkage intersection point (SIP). As the desorption phase is more applicable to wood drying, desorption RH and MC data were used to obtain the constants c_1 and c_2 for 0.5mm thick messmate samples and 1 mm thick samples for the other species. Thinner messmate samples were used to minimise error caused by collapse shrinkage. The values c_1 and $c_2$are essential species dependent constant properties for the development of an accurate wood drying model.

4.3 Results and discussion

4.3.1 Morphological characterisation

Table 4.1 contains the number of fibres and vessels measured, average fibre cell wall thickness, fibre, vessel and calculated total porosity, and measured and calculated density for each species. As the calculated cell wall thickness using *MeshPore* is based on the global sum of contours and tissue area, individual values are not calculated which prevents standard deviations to be determined.

Table 4.1 Average cell wall thickness (using MeshPore), fibre, vessel and total porosity, and measured and calculated density for each species in the unseasoned condition (n=1).

Species	No. fibres	No. vessels	Fibre cell-wall thickness (µm)	Fibre porosity (%)	Vessel porosity (%)	Total porosity (%)	Measured basic density (kg/m³)	Calculated density (kg/m³)
Spotted gum	56	125	6.1	7	16	22	921	1172
Jarrah	82	80	3.9	26	17	38	636	927
Blackbutt	113	113	4.1	28	14	38	674	927
Messmate	95	59	3.6	37	19	49	489	765

Distinct fibre and vessel porosity and fibre cell wall thickness differences between species were measured, as visually observed from ESEM images. Fibre cell wall thickness results (from 3.6 to 6.1 µm depending on species) are consistent with published data [136] suggesting that the average fibre cell wall thickness for wood generally ranges from around 3 µm to 8 µm.

Spotted gum has the lowest fibre, vessel and hence total calculated porosity and messmate the highest.

The calculated species density decreases with fibre cell wall thickness and increasing total porosity. Although fibre cell wall thickness and porosity play important roles in the overall density of wood, the frequency and cell wall thickness of ray parenchyma cells, and the frequency and size of hardwood vessels also contribute [136].

Calculated density values are always higher than the basic density measured on the samples used to grab ESEM images. The major reason for this systematic bias is that basic density, the oven-dry mass divided by the saturated volume, is the smallest value we can obtain, whereas the calculated values use the published oven dry density of wood tissue and the cell geometry determined on the sample in the ESEM chamber, at an equilibrium moisture content close to dry state. Another reason for this differenceis that our image analysis study focused on fibres and vessels. Other tissues of smaller density were not taken into consideration such as axial and ray parenchyma, which make up approximately 25% of wood tissue volume [131]. Additionally, intra-wall voids could also contribute to a lesser extent. However, a strong correlation was observed between measured and calculated density ($R^2 = 0.99$) as shown in Figure 4.7.

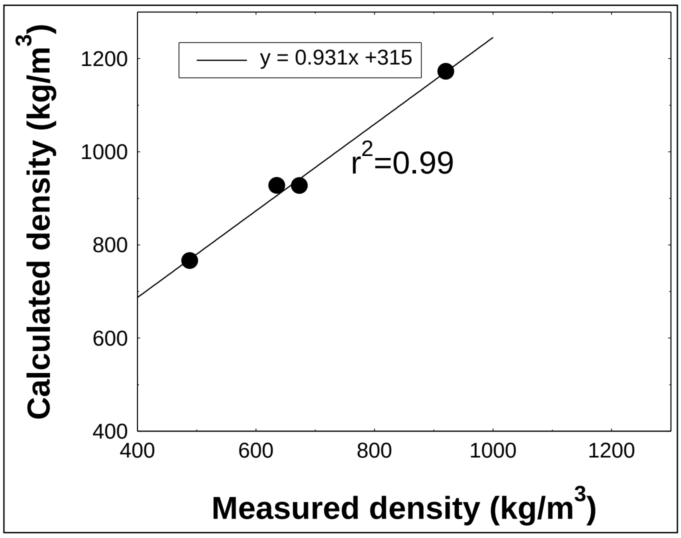

Figure 4.7 Measured versus calculated basic density correlation

4.3.2 Wood-water relations

For messmate samples having a thickness of 2, 1 and 0.5 mm, tangential and radial shrinkage versus MC curves were plotted as illustrated inFigure 4.8a and b. Note that the data defines a very accurate curve during the test period as the adsorption/desorption shrinkage closely follows the same curve (low MC tail of the graph). This feature was already observed and previously reported (Almeida *et al*. 2009; Perré 2007): depending on the moisture history, the sorption hysteresis changes the equilibrium content for a given relative humidity, but the sample dimensions depends only on the sample moisture content. The curves include two different phases:

- the removal of free water with minimal shrinkage, and
- a noticeable shrinkage phase, denoting the removal of bound water with a linear relationship with MC.

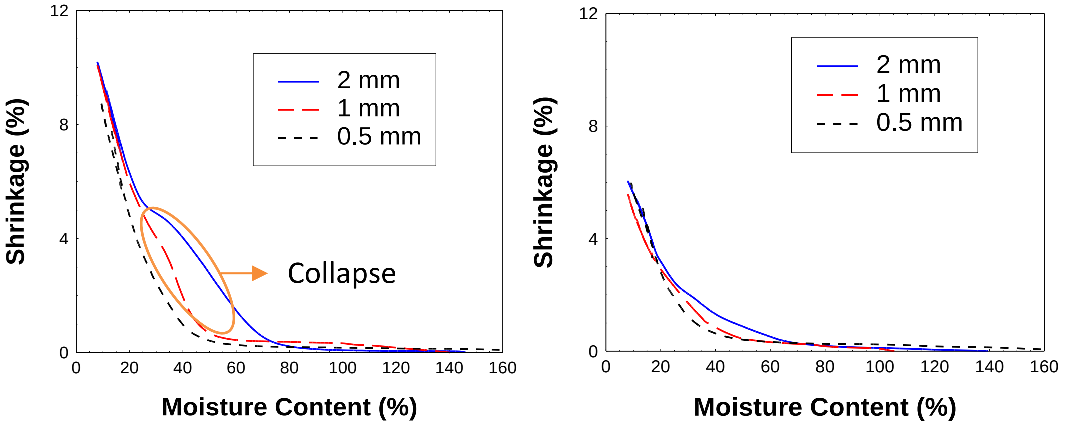

(a) (b)

Figure 4.8 Messmate tangential shrinkage curves showing collapse (a) and radial shrinkage curves (b) for 2, 1 and 0.5 mm thick samples

However, for 2 and 1 mm thick samples, abnormal shrinkage is present, occurring at high MC due to cell collapse during free water removal. This is more evident in the tangential direction is shown in Figure 4.8a. It appears that collapse shrinkage is eliminated by testing using 0.5 mm thick samples. Dadswell [134] measured the fibre length of 20 messmate specimens, the results ranging from a length of 1.04 to 1.27 mm. Thus, by reducing the dimension of the samples to less than 1 mm thickness, the majority of wood fibres should be severed. As tension of water inside the lumen is due to the huge percolation pressure required for air to go through the pits, a cut fibre will not collapse [30].

The fibre saturation point (FSP) is in many applications assumed as the MC below which specific wood properties begin to change as a function of MC. Several methods exist to measure FSP. In the work presented here, FSP is calculated by the shrinkage intersection point (SIP). This method assumes that no collapse occurs during the removal of liquid water. As this method is valid only in the absence of shrinkage, the thinner (0.5 mm thick) samples were used for this purpose. This is simply done from the shrinkage versus MC curves by subtending the linear portion of the curve, in the bound water/shrinkage phase, until it intersects the x and y-axis (Figure 4.9). The shrinkage at 12 %, a common published quantification of shrinkage, was calculated from the equation of the subtended line. Table 4.2 provides the total shrinkage, FSP, shrinkage at 12 %, and the radial/tangential (R/T) shrinkage ratios of the 0.5 mm thick messmate samples along with previously published data for jarrah, blackbutt and spotted gumfor comparison [30]. Published 12% MC shrinkage values [117] are also included

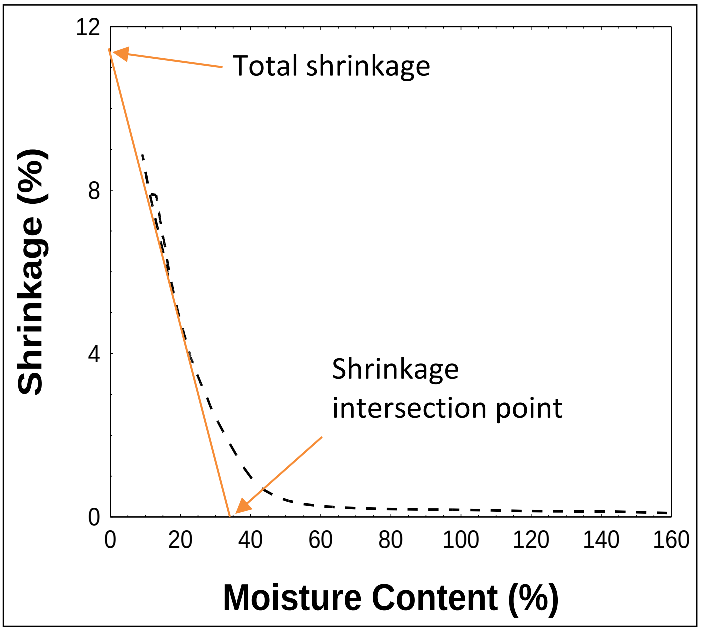

Figure 4.9 Example of total shrinkage and shrinkage intersection point (FSP) determination

Table 4.2 Shrinkage data measured for 0.5 mm thick messmate samples compared with previously measured data (Redman et al. 2011)

		Intersection point (FSP)MC (%)		Total shrinkage (%)		Shrinkage at 12 % MC					
						Measured			Bootle (2005)		
Sample #	Species	R	T	R	T	R	T	R/T	R	T	R/T
1	Messmate	28.0	31.3	9.0	12.3	5.0	7.6	0.66	3.5	6.5	0.54
3		28.1	33.5	8.0	11.7	4.7	7.5	0.63			
1	Jarrah	29.0	34.7	8.2	11.9	4.8	7.8	0.62	5.0	7.5	0.67
2		26.0	34.6	8.4	13.4	4.7	8.9	0.53			
1	Blackbutt	24.5	31.8	8.5	12.6	4.5	7.9	0.57	4.0	7.0	0.57
2		25.2	30.6	8.4	12.1	4.4	7.3	0.60			
1	Spotted gum	23.6	25.9	8.6	8.8	4.4	4.9	0.90	4.5	6.0	0.75
3		24.5	23.0	8.3	8.6	4.5	5.2	0.87			

Published FSP and 12% MC shrinkage values are consistent with measured data. It is interesting to note that the trend of increasing FSP values recorded aligns with increasing drying difficulty per species. That is, in this case, species with a higher FSP are more prone to checking collapse and splitting during drying. Shrinkage values and R/T ratios vary greatly between the tangential and radial directions except for spotted gum where the ratio is closer to 1:1. This may contribute to this species relative resistance to drying related mechanical defect in conjunction with low FSP values, compared to the other species.

By observing the MC versus RH sorption/desorption curves for each species, the hysteresis phenomenon is evident (Figure 4.10). The curves differ for each species due to different anatomical and chemical composition. In particular, extractive content levels and composition heavily influence sorption/desorption behaviour, where the removal of extractives leads to higher equilibrium moisture content at a given relative humidity [137]. The reducing RH/MC part of the curve (top part) is the desorption curve and is more applicable to wood drying which is a desorption process. Using data from this part of the curve, the constants c_1 and c_2 were calculated in the least squares sense using4-5for each species and are presented in Table 4.3. The values presented are generally consistent between species except for messmate constant c_2 whose value is more than double that for other species. Further investigation reveals that an increase in constant c_2 results in higher isotherm MC for a given RH. This is evident in the sorption/desorption curve. A higher isotherm MC for a given RH also results from a higher shrinkage intersection MC. This is evident for the isotherm curves of species messmate and jarrah, which recorded the highest intersection MC values.

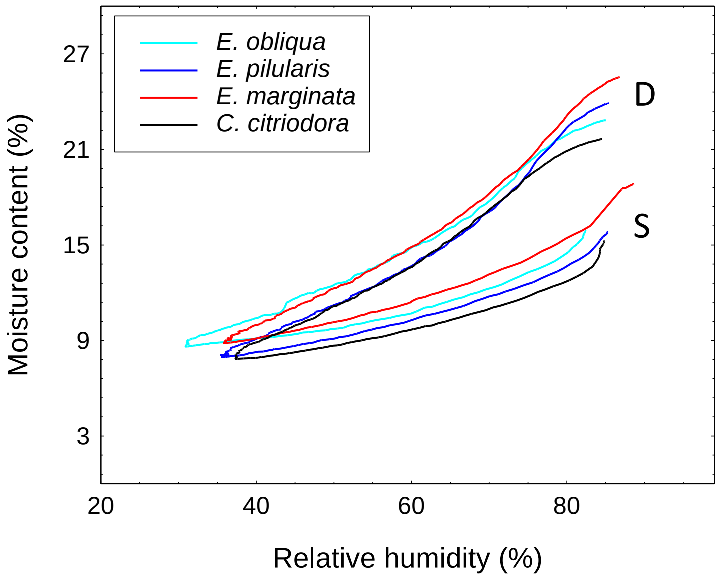

Figure 4.10 Desorption (D)/sorption (S) curves for each species

Table 4.3 Desorption isotherm solutions for constants c_1 and c_2

Species	c_1	c_2
Messmate	0.808	2.2800
Jarrah	0.972	0.840
Blackbutt	1.185	0.721
Spotted gum	1.005	0.908

4.3.3 From anatomical and physical properties to drying degrade

As stated in this introduction, this work aims at a comprehensive study of some Australia species for drying application purposes. It is therefore very interesting to check whether data collected at a microscopic scale (anatomical observations and measurements on minute samples) can help the understanding and the control of industrial drying. A further analysis of the whole dataset is proposed here and compared to drying trials performed in a 2 m^3 laboratory kiln.

Wood species susceptibility to different types of drying degrade can be attributed to a number of physical, mechanical and environmental properties. Wood fibre collapse has been found to be increase with temperature [108, 133]be affected by species, age, climate [133, 138], density [139], tree position [140, 141], growth rings [142], chemical and cell structure [133]. Kaumann [133] states that collapse depends on the cell pore size, thickness and strength where small variations in either can cause large variations on collapse intensity. He declares that correlation of collapse with any anatomical feature will be at least partly obscured by random statistical variations of these properties.

The propensity for stress related drying degrade, such as end splitting, and surface and internal checking can be exacerbated by low diffusion rates and high shrinkage [143]. Additionally, collapse degrade has also been shown to intensify and/or initiate internal checking [108]. Drying stress related splitting and checking (external and internal) can be reduced by the presence of interlocked grain [144].

Qualitative and quantitative data used to investigate the drying behaviour is provided in Table 4.4. They include the fibre lumen diameter, fibre cell-wall thickness and their ratio, the ratio of total radial to tangential shrinkage (calculated from Table 4.2), and the ratio of transverse total shrinkage to diffusion coefficient. Diffusion coefficient values were previously published by Redman *et al.* [30].

Table 4.4 Quantitative and qualitative data for comparison between drying degrade propensity

Species	Fibre lumen diam. (μm)	Fibre cell-wall thick. (μm)	Fibre cell-wall diam.: thick. ratio	Total shrink. R:T ratio	Trans. shrink.: diffusion coefficient ratio	Collapse shrinkage observed	Split/ check	Grain type
Spotted gum	4.0	6.1	0.66	0.98	6.09E+11	no	low	interlocked
Jarrah	12.0	3.9	3.08	0.65	4.92E+11	no	low	interlocked
Blackbutt	9.3	4.1	2.27	0.69	4.64E+11	no	high	straight/slightly interlocked
Messmate	11.7	3.6	3.26	0.71	2.10E+11	yes	high	straight

Drying degrade, observed from a series of drying trials [20], includes the species propensity to collapse, split and check, and the species grain type; interlocked, straight or a combination. Quantitatively, the percentage of collapse, surface check, internal check and end split of 100 boards dried in industrial drying trials [20] are provided in Table 4.5.

Table 4.5 Example of drying degrade results from industry drying trials

Species	Percentage of boards affected*			
	Collapse	Surface check	Internal check	End split
Spotted gum	0	17	0	11
Jarrah	0	16	12	6
Blackbutt	0	83	0	64
Messmate	100	29	4	77

Instead of trying multifactorial analysis of all these parameters, we derived some synthetic indicators, built from our data base, that are likely to explain the drying behaviour:

1. **The propensity to collapse**: as it is almost impossible to get reliable information regarding the percolation pressure, we limited our analysis to the ability of cells to withstand negative pressure. A simple analysis of stress in a cylinder tells us that the ratio of lumen diameter over cell wall thickness is a relevant parameter.

2. **The propensity for deformation**: the shrinkage ratio is well known to be involved in the deformation of sections due to bound water removal. A very anisotropic shrinkage may also induce drying stresses due to incompatible strain fields.

3. **The propensity to induce drying stress**: drying stresses are produced during drying due to the non-uniform strain field generated by shrinkage. This strain heterogeneity obviously increases with the shrinkage value and the extent of the moisture gradient profile. Therefore, the shrinkage value along the board surface divided by the mass diffusivity along the normal is a good candidate.

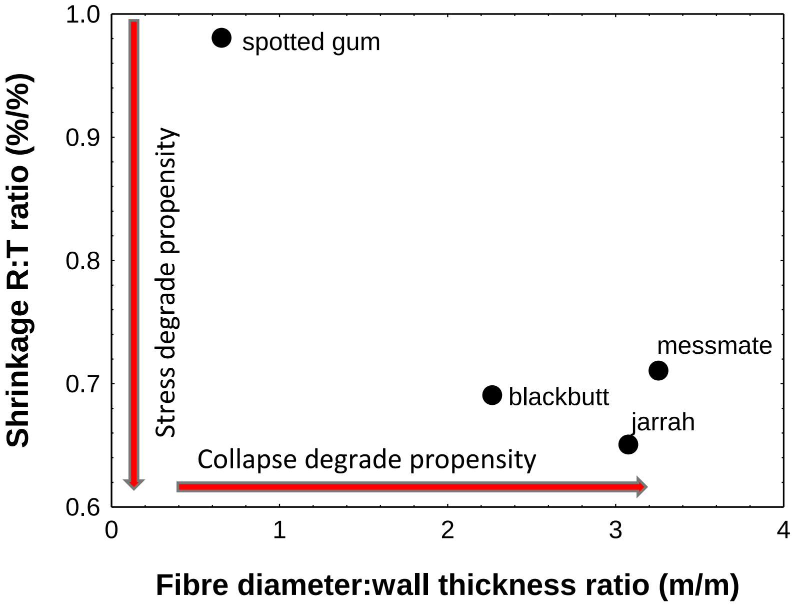

Figure 4.11 Species propensity to deform and stress drying degrade based on fibre geometry ratio and transverse shrinkage ratio

Figure 4.11 plots the ratio of fibre lumen to cell-wall thickness versus indicator 2 (total radial/tangential shrinkage ratio) for each species. The plot shows messmate, exhibits the highest tendency to collapse compared with other species; a fact backed up by experimental data (Table 4.5). The plot also indicates jarrah and blackbutt may be prone to collapse. Although not observed in experimental data, published data confirms that Blackbuttat least is prone to collapse [145]. In terms of both fibre properties and its almost 1:1 radial/tangential shrinkage ratio, spotted gum exhibits low collapse and drying stress degrade propensity compared with the other species. The other species are shown to be collectively more prone to deformation related degrade (Figure 4.11 and Table 4.5).

Figure 4.12 provides another observation of the relationship between species: the propensity to drying stress (indicator 3) versus the collapse propensity (indicator 1). The same collapse propensity relationship is evident as for Figure 4.11, however these results indicate that spotted gum should be comparatively more prone to stress related degrade. This does not agree with the measured data (Table 4.5). This discrepancy is likely due to the very tight interlocked grain spotted gum, which can provide more resistance to drying stress wood tissue rupture compared with the straight grain of messmate. Additionally, messmate is possibly more prone to checking due to its propensity (100% for this species and 0% for others) to collapse (a factor not included in this analysis). Further research into the effect of interlocked grain on drying degrade is recommended.

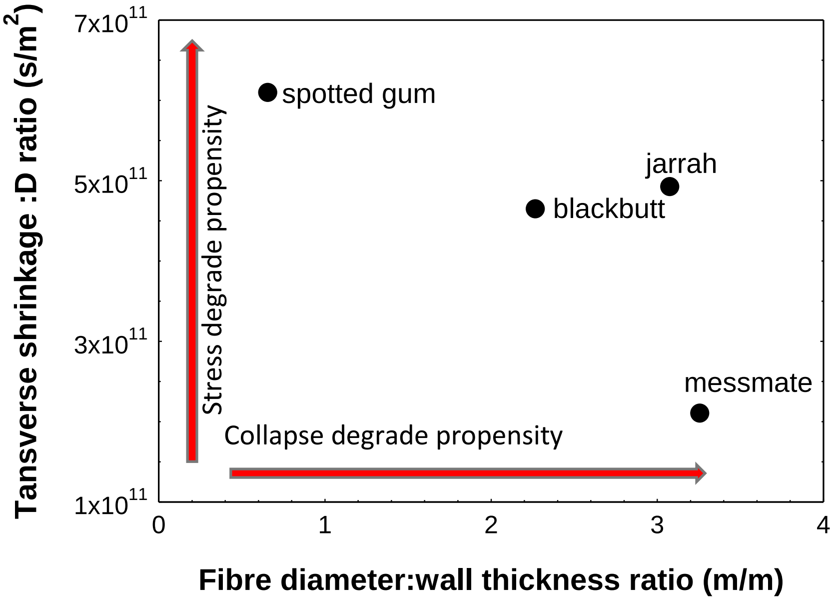

Figure 4.12 Species propensity to incur collapse and stress drying degrade based on fibre geometry ratio and transverse shrinkage to diffusion ratio

4.4 Conclusions

Cell wall thickness and wood porosity as a combination of fibre and vessel porosity, using a combination of ESEM and optical microscope scans, and image analysis using *MeshPore* were realised for each species. Clear differences in these values between species were evident. A strong correlation exists between measured and calculated wood density based on porosity measurements. Higher calculated values were evident as they do not take into account axial and ray parenchyma cell and intra-wall voids. Measurement of radial and tangential shrinkage for messmate using a highly accurate, dynamic method free of collapse shrinkage was achieved and was consistent with published data. This was not possible in a previous study by Redman *et al.*[30] which used relatively thick samples, but was accomplished using very thin 0.5 mm samples. We also tested thicker samples in this study to demonstrate their propensity to collapse. Data obtained from the shrinkage measurements of messmate from this study and spotted gum, blackbutt and jarrah from Redman *et al*. [30] previous study allowed the generation of sorption/desorption curves for each species. We used data to approximate desorption isotherms for each species where the messmate results substantially different to the other species. As previously reported, messmate exhibits properties that are generally extreme or do not follow the typical trend when compared with other species. Messmate is by far the hardest wood to dry in terms of collapse and checking and exhibits more extreme wood properties compared to easier to dry species.

Accurate determination of wood porosity, tangential and radial shrinkage, and desorption isotherms are parameters necessary for precise deterministic modelling of the drying process.

These results indicate, that by comparing certain data related to drying degrade, it is possible to explain the observed difficulty in drying relevant to different species. Fibre geometry can be used to provide an indication of collapse propensity and the ratio of total radial: tangential shrinkage may be linked to stress degrade propensity. Care must be taken however as other wood characteristics and properties may need to be considered such as the presence of interlocked grain.

Chapter 5
Heat and mass transfer drying model

This chapter features the bulk of the published journal article "*A relevant and robust vacuum drying model applied to hardwoods*" published online in Wood Science and Technology journal on 24 June, 2017, where some minor alterations have been made based on reviewers' comments.

Statement of Authorship. This work was divided as follows:

- *Mr. Adam Redman* (Candidate) wrote the majority of the article, created input meshes, produced model input data, wrote MATLAB functions to improve model functionality, performed the simulations and developed the sensitivity analysis method.
- *Dr. Henri Bailleres* assisted in the methodology and proposed the collaboration with Professors Turner and Perré to perform modelling simulations.
- *Prof. Patrick Perr*é directed and guided the work, developed the original *TransPore* model for porous media and assisted in design of experimental methods and linkages between simulated output and drying degrade propensity.
- *Dr. Elliot Carr* assisted in developing model components applicable to hardwood drying, and improving convergence times and model functionality. He also developed the MATLAB version of *TransPore*, which was originally written in Fortran.

- *Prof. Ian Turner* also directed and guided this work and developed the original *TransPore* model for porous media. He was instrumental in guiding effective simulations and advising

SIGNED:

DATE:

19/8/2017

5.1 Introduction

The successful control of wood defects during drying consists in maintaining a balance between the rate of evaporation of moisture from the surface and the rate of outward movement of moisture from the interior of the wood. One of the most successful ways of controlled wood drying is by kiln drying.

Conventional kiln drying with controlled heating, humidity and air-flow under atmospheric pressure conditions is the primary method for drying timber in Australia [1]. In recent years, with emerging technological advancements in construction, design, computer control and less expensive materials, vacuum drying of hardwood timber(particularly in Europe and USA) has proven in many applications to be a more economical alternative to drying using conventional methods, with similar or better quality outcomes [4]. For this reason, in 2007 the Queensland Government Department of Agriculture and Fisheries (DAF) purchased a 2 m^3 research vacuum kiln.

Preliminary results generated much interest from the Australian hardwood timber industry. In response, DAF invested in a project to establish the viability of vacuum technology for drying four high volume commercial Australian hardwood species with respect to drying quality, time and cost. Moreover, it was recognised that a better knowledge of the material and associated drying behaviour is required to fully optimise the vacuum and conventional drying processes in the future [3].

In the past, substantial modelling work has been conducted for softwood species due to its commercial importance and relative homogeneity between species [6-9]. The most accurate deterministic model to date encompasses multiscale and multiphysics descriptions of drying phenomena for softwoods [17, 18]. This paper utilises an existing drying model known as *TransPore* [7, 16], which has been successfully used to predict the drying behaviour of softwoods and drying of other porous media, such as concrete, and applies it to hardwood species. We note here that recent enhancements of *TransPore* developed by Carr et. al., which include novel strategies such as variable-stepsize Jacobian-free exponential time stepping [71] and a dual-scale modelling approach [72], are not included in this work.

The complexity of the wood structure of hardwoods together with the huge variation within and between species, have resulted in limited deterministic modelling work being performed to date on these species. Additionally, limited data are currently available for vacuum drying Australian hardwood species.

The aim of this work is to develop an accurate, deterministic heat and mass transfer model for four commercially important native hardwood species, with extreme diversity between their drying characteristics. We chose species with highly diverse drying characteristics to a) ensure the model is robust enough to work for a large range of species and b) investigate the effect of the external drying boundary conditions on the wood behaviour and overall rate of vacuum drying compared with conventional schedules. Two versions of the model were developed; one modelling heat and mass transfer in the wood cross-sectional transverse or radial (R)-tangential (T) plane and the other in the transverse (R or T)-longitudinal (L) plane (Figure 5.2). This allows us to investigate the effect of vacuum pressure on longitudinal migration and the associated internal pressures generated in the timber section during vacuum drying as compared to conventional drying. The R and T wood directions are interchangeable and depend on the predominant cutting pattern of the board.

This model is validated by comparing the drying rate to vacuum drying trials conducted for each species as described by Redman [29]. Previous research [3, 25] has shown that a number of essential wood properties must be measured to provide the necessary information for developing an accurate heat and mass transfer drying model. The other wood properties can be inferred from either existing data or empirical formulae. This model uses boundary conditions generated by these trials and the experimentally measured wood properties previously reported by Redman *et al*. [30], Redman *et al*. [146] and Redman *et al*. [75]. The wood properties measured include initial wood moisture content (MC), fibre saturation point, basic density, porosity, gas permeability, bound water diffusion, shrinkage and desorption isotherms.

We complement this work by conducting a sensitivity analysis to investigate which of the wood properties (input variables) has the most impact on the model MC output. This allows us to rank these wood properties in order of sensitivity (see Section: *Sensitivity analysis*).

This work contributes to the establishment of a vacuum and conventional hardwood drying model, whose accuracy relies on the use of measured input data rather than relying on empirical formulae, which due to the varying nature of wood properties between species, are not always reliable. The work presented has the potential to optimise drying, in terms of drying time and degrade, for hardwood species.

In the following section, we begin by outlining the mathematical model used for simulating the drying of hardwood species and associated sensitivity analysis, before presenting the results of this analysis and model simulations in subsequent sections.

5.2 Materials and methods

The following describes the mathematical model used, species investigated and input variables for analysis.

5.2.1 Conservation equations

As the anatomical configuration of wood is complex, one must use volume averaged transport equations at the macroscopic scale. This leads to the definition of macroscopic laws of conservation that are averaged over representative volumes [3]. By using this approach, we can write most fluxes as the product of an effective coefficient multiplied by the relevant driving force. The conservation of liquid, water vapour, air and enthalpy enable a set of equations governing transfer in porous media to be derived [73]. These equations have subsequently been used to model the softwood drying process [3, 16], where their ability to describe several different drying configurations has been proven [17, 69, 74].

Liquid conservation is described by:

$$\begin{aligned}
&\frac{\partial}{\partial t}\left(\varepsilon_w \rho_w + \varepsilon_g \rho_v + \overline{\rho}_b\right) \\
&+\nabla \cdot \left(\rho_w \overline{\boldsymbol{v}}_w + \rho_v \overline{\mathbf{v}}_g + \overline{\rho_b \mathbf{v}_b}\right) \qquad (5\text{-}1) \\
&= \nabla \cdot (\rho_g \overline{\overline{D}}_{eff} \nabla \omega_v)
\end{aligned}$$

energy conservation by:

$$\begin{aligned}
&\frac{\partial}{\partial t}(\varepsilon_w \rho_w h_w + \varepsilon_g (\rho_v h_v + \rho_a h_a) + \overline{\rho}_b \overline{h}_b + \rho_s h_s - \varepsilon_g P_g) \\
&+\nabla \cdot (\rho_w h_w \overline{\mathbf{v}}_w + (\rho_v h_v + \rho_a h_a) \overline{\mathbf{v}}_g + h_b \overline{\rho_b \mathbf{v}_b}) \qquad (5\text{-}2) \\
&= \nabla \cdot (\rho_g \overline{\overline{D}}_{eff} (h_v \nabla \omega_v + h_a \nabla \omega_a) + \overline{\lambda}_{eff} \nabla T)
\end{aligned}$$

and, air conservation by:

$$\frac{\partial}{\partial t}(\varepsilon_g \rho_a) + \nabla \cdot (\rho_a \overline{\mathbf{v}}_g) = \nabla \cdot (\rho_g \overline{\overline{D}}_{eff} \nabla \omega_a) \tag{5-3}$$

The gas and liquid phase velocities are given by the Generalised Darcy's Law:

$$\overline{\mathbf{v}}_l = -\frac{\overline{\overline{K}}_l \overline{\overline{k}}_l}{\mu_l} \nabla P_l \tag{5-4}$$

where $l = w, g$.

This formulation accounts for the evolution of internal pressure through the air balance equation (5-3) and is thus able to deal with high temperature convective drying and vacuum drying.

5.2.2 Closure conditions

Wood is a highly hygroscopic porous medium; therefore, bound water must be separated from free water as defined by:

$$X = X_w + X_b \equiv \frac{\varepsilon_w \rho_w}{\rho_o} + \min(X_{fsp}, X). \tag{5-5}$$

The volume fractions of the liquid and gaseous phases are defined as: $\varepsilon_w = \phi S_w$, $\varepsilon_g = \phi(1 - S_w)$, $\varepsilon_w + \varepsilon_g = \phi$, where ϕ is the porosity. The average air density is defined as $\overline{\rho}_a = \varepsilon_g \rho_a$ and the gaseous phase is a mixture of air and vapour, which is assumed to behave like an ideal gas. The saturation variable involved in the relative permeability functions is calculated according to the free water content only:

$$S_w = \frac{X_w}{X_{w\max}}. \tag{5-6}$$

Both liquid and gaseous water phases are present during the drying of wood. Because of the curvature of the interface that exists between the liquid and gas phases within the wood pores, the liquid pressure is less than the gas pressure. The difference is represented by the capillary pressure:

$$P_w = P_g - P_c, \tag{5-7}$$

where the gas pressure (P_g) is the sum of the air (P_a) and vapour (P_v) partial pressures:

$$P_g = P_a + P_v. \tag{5-8}$$

The values for fibre saturation point (X_{fsp}) is one of the essential wood properties necessary for the development of an accurate wood drying model. The measurement of fibre saturation point is detailed by Redman et al. [30] and Redman et al. [75] by observing the shrinkage behaviour of thin wood sections during desorption. The fibre saturation point values measured for each species are provided in Appendix A. Siau [21] demonstrates the dependency of X_{fsp} on temperature, such that at 25°C, with a measured wood X_{fsp} of 30%, the temperature dependent fibre saturation point X_{fspT} is expressed as:

$$X_{fspT} = 32.5 - 0.1T, \tag{5-9}$$

where T is the wood temperature in °C. As the measured X_{fsp} for each species varies and to keep the relative effect of T on X_{fsp} the same, equation (5-9) is modified to correct the slope using the following expression:

$$X_{fspT} = \frac{X_{fsp}}{32.5}\,(32.5 - 0.1T) = X_{fsp} - \frac{0.1\,X_{fsp}}{32.5}T. \tag{5-10}$$

5.2.3 Initial, boundary and drying conditions

The boundary conditions for the external drying surfaces are assumed to be of the following form [69]:

$$\mathbf{J}_w \cdot \hat{\mathbf{n}} = k_m c M_v \ln\left(\frac{1-x_\infty}{1-x_v}\right) \tag{5-11}$$

$$\mathbf{J}_e \cdot \hat{\mathbf{n}} = q(T - T_\infty) + h_v k_m c M_v \ln\left(\frac{1-x_\infty}{1-x_v}\right) \qquad (5\text{-}12)$$

$$P_g = P_\infty, \qquad (5\text{-}13)$$

where $\mathbf{J}_w$ and $\mathbf{J}_e$ represent the fluxes of total moisture and total enthalpy at the boundary, respectively. x_∞ and x_v represent the molar fraction of gas vapour in the kiln at the exchange surface, respectively. The pressure P_∞ and temperature T_∞ at the external drying surfaces are fixed at the kiln vacuum pressure and operating temperature. As one of the primary variables used for the computations is the average air density, the boundary pressure condition (5-13) is modified to form an appropriate nonlinear equation using the Ideal Gas Law:

$$\varepsilon_g(P_v - P_\infty) + \frac{\overline{\rho}_a RT}{M_a} = 0. \qquad (5\text{-}14)$$

Initially the board has some prescribed MC, with the pressure and temperature fixed throughout the board at the initial kiln pressure and temperature respectively.

The drying is assumed to occur on the top and bottom surfaces of the modelled board as the edges of boards placed in a kiln are butted up against each other. For this model, the airflow affects only the top and bottom surfaces of the board flowing in the direction parallel to the boards' surfaces.

The values for external pressure, temperature and air velocity, from the vacuum trials data, are essential boundary condition parameters for the development of an accurate deterministic wood drying model and were measured by Redman [29] and used in this study. A pressure gauge was used to record kiln pressure, thermocouples to measure kiln temperature and two *Schiltnecht MiniAir60* anemometers were inserted within the wood stack to record air velocity during drying. Several boards were weighed using *Scaime F60F* load cells during drying trials, which were used to measure average MC. The core temperature of boards was measured using T-type thermocouples. Moisture content and core temperature measurements were used to validate the model. An example of recorded kiln boundary conditions and average board MC for messmate is provided in Figure 5.1.

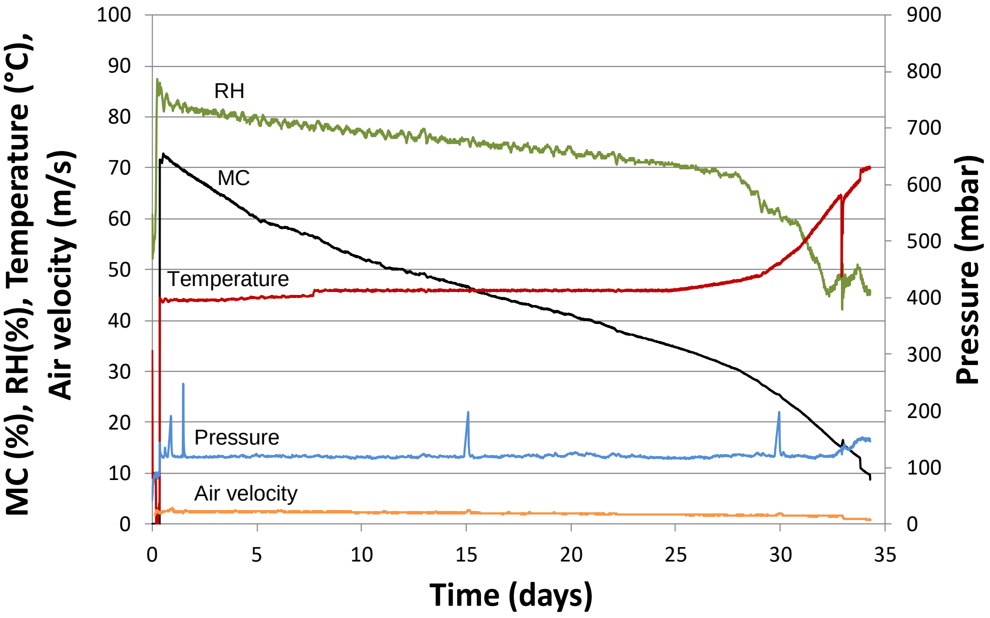

Figure 5.1 Example of measured kiln vacuum drying trial conditions for messmate, showing kiln relative humidity (RH), temperature, pressure and air velocity as well as average wood moisture content (MC).

As boundary condition and MC data were recorded at discrete time intervals, the data was converted into time-based functions using the *TableCurve2D* software (https://systatsoftware.com/). The sigmoid transition function equation (5-15) was used to fit the measured data due to its accuracy of fit and stability outside the measurement range:

$$y = a + \frac{b}{\left(1+\exp\left(-\frac{x-c}{d}\right)\right)} \tag{5-15}$$

where a, b, c and d are curve fit constants.

We use these functions within the drying model program to change boundary conditions with time.

5.2.4 Numerical solution procedure

The numerical procedure employed to resolve the drying model in this work has been extensively published, and the reader is referred to the most relevant literature for the finer details [7, 16, 71, 72]. Equation (5-14) must be resolved, along with the conservation laws, during the nonlinear iterations for every external boundary control volume within the computational domain. The finite volume method is implemented on a triangular mesh within a rectangular domain, to discretise the conservation laws [71]. Meshes were generated over board transverse and longitudinal cross-sections. Thereafter, an efficient inexact Newton method is used to resolve in time the nonlinear system that describes the drying process. Upwinding is used to determine the spatial weighting schemes for all advection/convection terms in the equations and the introduction of the fixed phase ensures that full saturation $S_w = 1$ is never reached at the surface of the medium[77]. This enhances convergence of the model and ensures accurate resolution of the drying fronts on relatively coarse meshes and are particularly useful for simulating the vacuum drying process [69].

The radial-tangential mesh used for the simulations reported here consisted of 7428 triangular elements and the transverse-longitudinal mesh consisted of 6404. For each species, we used the actual board dimensions to generate mesh geometry. The approximate board width and thickness were 100 x 30 mm, respectively. The board length was 1900 mm (Figure 5.2).

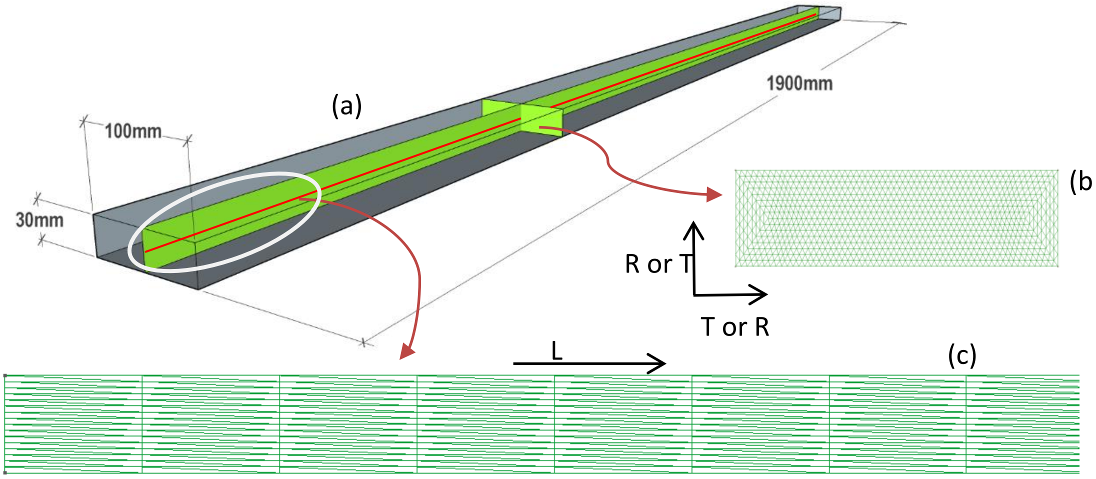

Figure 5.2 Schematic of board (a) showing the position of the radial (R)-tangential (T) mesh (b) and magnified transverse (R or T)-longitudinal (L) mesh (c)

5.2.5 Wood species

The species under investigation are mature native forest spotted gum (*Corymbia citriodora* Hook), blackbutt (*Eucalyptus pilularis* Sm.), jarrah (*Eucalyptus marginata* D.Don ex Sm.) and messmate (*Eucalyptus obliqua* L'Herit). The wood species chosen for this study were based on their large commercial volume, value and range of drying characteristics and wood properties. For example *C. citriodora* is the easiest species to dry in terms of resistance to drying degrade and has the highest basic density (BD) of 921 kg/m^3 [29] followed by *E. pilularis* (674 kg/m^3 BD) and *E. marginata* (636 kg/m^3 BD) which are mildly susceptible to surface checking. Finally, despite its lowest BD of 489 kg/m^3, *E. obliqua* is one of Australia's hardest species to dry due to its propensity to collapse, internal and surface check.

The measured wood properties used for simulations are described in detail by Redman *et al.* [30], Redman *et al.* [146] and Redman *et al.* [75]. These, along with the formulated physical properties are provided in *Appendix A*. Our preliminary simulations for spotted gum using the tabulated model parameters produced unrealistically high internal gaseous pressures. This was not the case for any of the other specifies investigated. An important observation is that the permeability of spotted gum is in the order of a factor of 100 to 10,000 times less than the other species (refer Table A1). We believe that as a direct consequence of this low permeability value, the high overpressure generated does not induce an outwards air flux that decreases the pressure. In fact, our numerical experimentation highlighted that the quite large value of gaseous diffusion in comparison to the bulk gas flow, which is proportional to permeability via Darcy's law, allows an inward directed air diffusion phenomenon without any substantial outward directed advective flux. Therefore, in order to have an effective diffusivity value D_{eff} that is consistent with such a low value of gas permeability, we decided to reduce the value of the air diffusivity (not the vapor diffusivity) by a factor of 100 (see eq. A-6) for the spotted gum species simulations. In making this modification a much more realistic value of internal overpressure was observed and these results are exhibited in figures 5.8a-b.

5.2.6 Sensitivity analysis

We conducted a study to determine which of the measured inputs contribute most to the sensitivity of the model determination of final MC over a fixed time. Such a study can be used to investigate which parameters are most significant for model accuracy.

A number of techniques exist for model sensitivity analysis with varying degrees of complexity depending on the model type and desired outcome [147]. For this study, we used the one-at-a-time (OAT) technique. This is a technique, where one input parameter is changed at a time while the others remain fixed [148, 149]. Hamby [147] suggests that the most powerful sensitivity test examines the change in output as each input parameter is individually increased or decreased by a factor of its standard deviation.

For this study, the data from each measured input parameter, for each species, was combined to build a representative data set. For each input parameter of this combined data set, the mean and standard deviation values were calculated. The mean value for each input variable was used for the 'base' sensitivity analysis model. As one input variable was incrementally changed, the remaining variables were fixed at their mean values.

The sensitivity analysis was conducted by running the model and changing one input variable between a range of ±2 standard deviations of its mean value at 7 equidistant discrete points. This ±2 standard deviation range was used as it approximates to 5 to 95 % of the population data for each variable, while removing population outliers. For each simulation, the model was run for a drying period of 520 hours and the final MC was recorded. The 520 hour drying period, when all input parameters were set to their mean values, resulted in a final MC of 13%.

5.2.7 Simulations

Simulations were conducted using an Intel QuadCore i7860 processor using Matlab version 2011a. Convergence times varied depending on wood species and simulation plane. The average convergence time was 4.5 minutes.

Model accuracy was determined for each species by calculating the error between simulated and measured drying trial MC and temperature output data. As the drying time between species was different, we calculated the error using the root-mean square error (RMSE). The RMSE, expressed in the units of y in equation 15, is defined as:

$$\mathrm{RMSE} = \sqrt{\frac{\sum_{t=1}^{n}(\hat{y}_t - y_t)^2}{n}} \tag{5-16}$$

where n is the number of discrete data points, $\hat{y}_t$ are the simulated model output values at time t, y_t are the corresponding trial output values.

The conventional drying schedules used (temperature, humidity and air velocity) are recommended by Rosza and Mills [150] and are presented as MC, temperature, humidity and air velocity set points in Table 5.1. Table 5.1 also contains the vacuum drying schedules used for simulations, including kiln pressure.

The accuracy for the model to predict the final drying time at a final MC of 10% was calculated using:

$$E_{dt} = \frac{|t_e - t_s|}{t_e} \times 100, \tag{5-17}$$

where E_{dt} is the drying time error (%), t_e is the experimental drying time and t_s is the simulation drying time.

Table 5.1 Conventional and vacuum drying schedules used for spotted gum and messmate simulations

Moisture content change point (%)	spotted gum					messmate				
	Conventional		Vacuum			Conventional		Vacuum		
	Temp. (°C)	RH (%)	Temp. (°C)	RH (%)	Pressure (mbar)	Temp. (°C)	RH (%)	Temp. (°C)	RH (%)	Pressure (mbar)
>70	45	83	64	78	200	25	77	44	85	130
70 - 60	45	83	65	76	200	25	77	44	85	130
60 - 50	45	78	66	75	200	25	77	45	82	130
50 - 40	45	78	66	73	200	30	73	45	75	130
40 – 35	45	78	67	70	200	30	73	45	73	130
35 – 30	50	79	67	70	200	35	75	45	73	130
30 – 25	55	64	69	66	200	40	71	58	65	130
25 – 20	60	58	71	55	200	45	60	64	65	130
20 – 15	70	47	75	40	250	50	54	72	35	150
15 - final	70	35	80	55	380	55	40	80	55	160

5.3 Results and discussion

5.3.1 Sensitivity analysis

The sensitivity analysis results are presented in Table *5.2*, in order of most to least sensitive. The results are expressed as the range of final MC resulting from sensitivity simulations, for each input variable. Parameters with the largest range of final MC after 520 hours of simulated drying were deemed most sensitive. We conclude that basic density is the most sensitive input variable, followed by radial bound water diffusion coefficient and radial gas permeability. Desorption isotherm constant c_2 and fibre saturation point follow in order of reducing sensitivity. It seems that accurate measurement of desorption characteristics, as previously suggested by [54], wood density and bound and free water movement, represented by diffusion coefficient and permeability, in the direction of board thickness (radial in this case) are most sensitive compared to the other input variables. The least sensitive input variables are wood porosity, longitudinal direction bound-water diffusion coefficient and longitudinal permeability. Transport properties in the transverse wood direction are more sensitive than in the longitudinal direction. This is the direct effect of low longitudinal permeability and mass diffusivity of these Australian hardwood species, at least in relation with the low dimensional ratio of board thickness to length. This trend could eventually change as the length of the board is reduced.

Table 5.2 Sensitivity analysis final MC range results in order of most to least sensitive

Input variable	Final MC range (%)
Basic density	3.76
Radial bound-water diffusion coefficient	3.56
Radial gas absolute permeability	2.51
Desorption parameter c2	2.31
Fibre saturation point	1.80
Tangential gas absolute permeability	1.78
Initial moisture content	1.72
Desorption parameter c1	1.03
Longitudinal gas absolute permeability	0.26
Tangential bound-water diffusion coefficient	0.26
Longitudinal bound-water diffusion coefficient	0.15
Porosity	0.07

5.3.2 Simulations

Simulation output consists of a series of two-dimensional MC, internal pressure and wood temperature fields that depend on the drying time and external boundary conditions. An example of the MC field after 0, 145, 475 and 840 hrs of drying for messmate are shown in Figure 5.3. As permeability values measured for each species are very low, drying is predominantly driven by diffusion, hence the steep moisture gradients set-up during drying. Simulated outputs include the average board MC, and core temperature and gas pressure (P_g) values and are used in the following investigations.

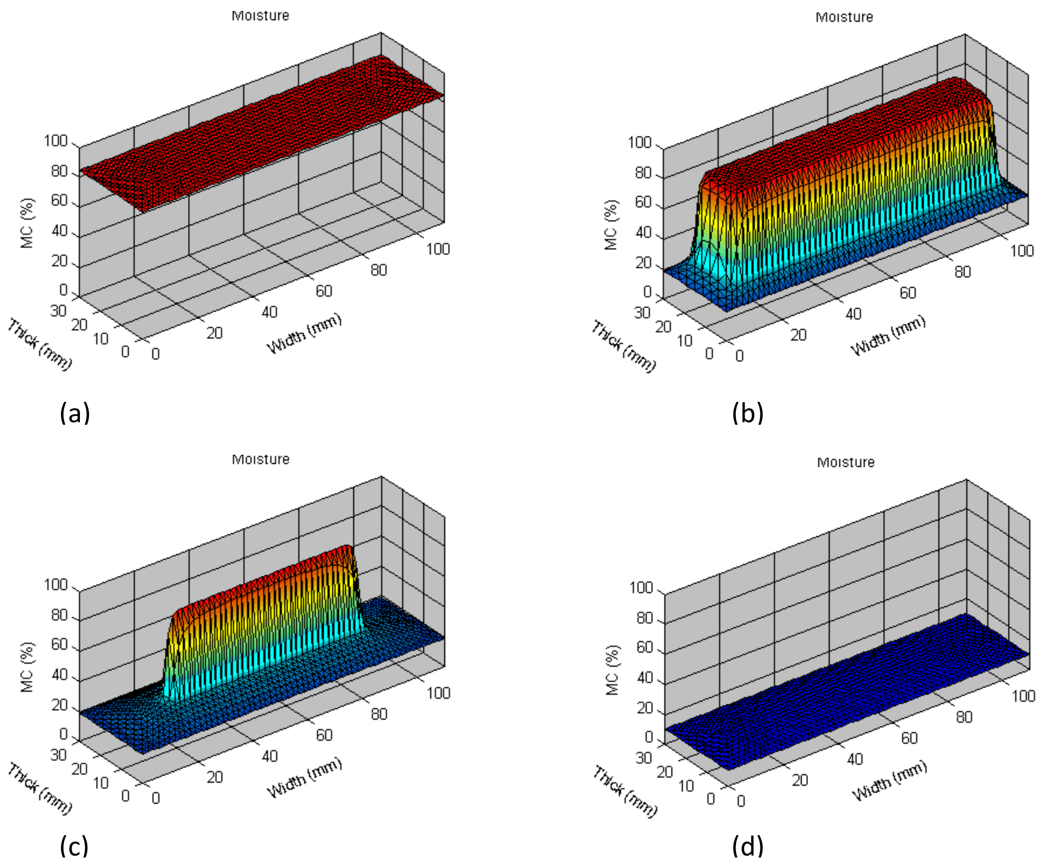

(a) (b)

(c) (d)

Figure 5.3 Example of simulation MC visualisation of vacuum drying messmate in the radial-tangential cross-section at time/average MC of 0 hrs/85% (a), 145 hrs/60% (b), 475 hrs/30% (c) and 840 hrs/12% (d)

Prior to bound-water diffusion coefficient measurements, as described by Redman *et al*. [146], vacuum simulations were conducted using empirical bound-water diffusion coefficient values for each species. When comparing the average MC results, between model simulations and experimental drying trials for each species in the radial-tangential and longitudinal-transverse planes, simulated output produced vastly faster drying rates than experimental observation. An example for spotted gum is shown in Figure 5.4.

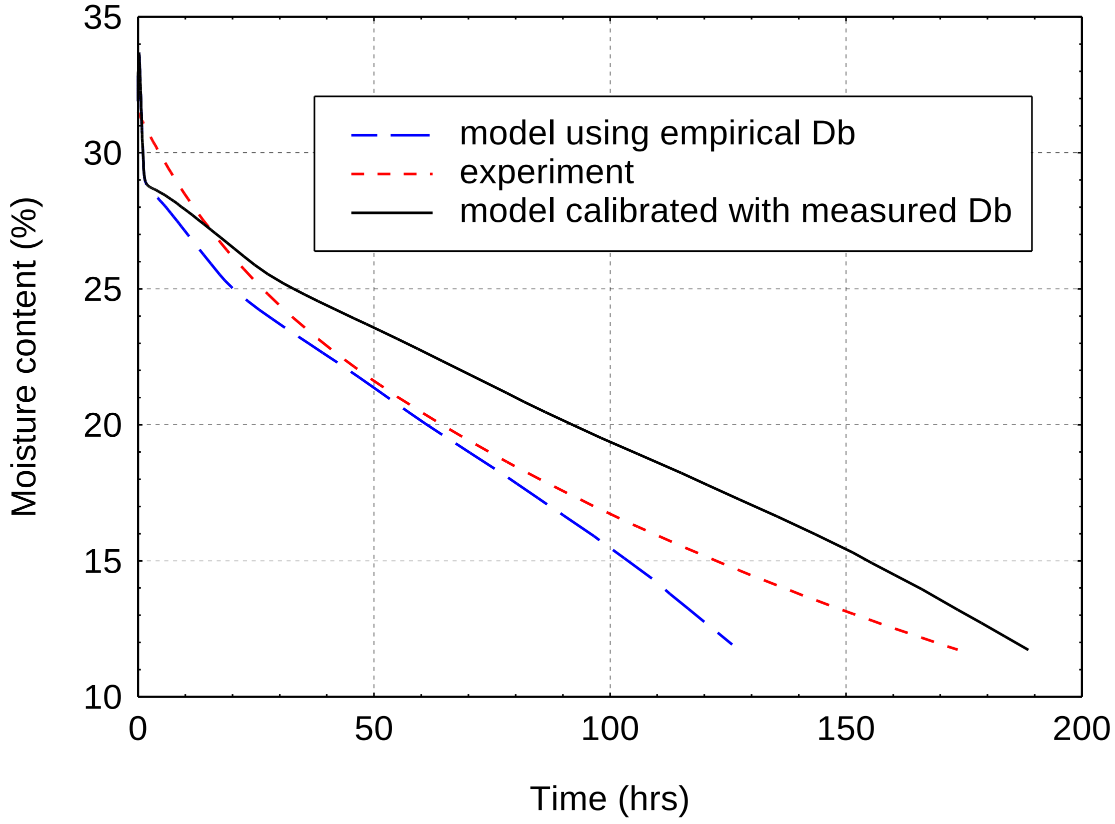

Figure 5.4 Simulated average MC of vacuum dried spotted gum in the radial-tangential plane, empirically calculated bound-water diffusion coefficient (Db) values and calibrated values using measured data, including experimental MC output results

Bound-water coefficient measurements were subsequently compared with empirical values. This was done by calculating the transverse and longitudinal diffusion coefficients under the same measured temperature and humidity conditions; 35°C and 40% relative humidity, respectively. The ratio of measured to calculated bound-water diffusion coefficient, at those temperature and humidity conditions, for each species and wood direction are provided in Table 5.3. The results indicate that a discrepancy exists between the measured and empirical values, where measured values are substantial lower, particularly in the longitudinal direction. The reason for this discrepancy requires further investigation, however wood extractives are suspected to be a significant factor.

Table 5.3 Measured and empirical bound-water diffusion coefficient ratios in the radial, tangential, and longitudinal wood directions for each species at 35°C and 40% relative humidity

Species	Radial	Tangential	Longitudinal
Messmate	0.76	0.59	0.21
Jarrah	0.62	0.36	0.07
Blackbutt	0.63	0.39	0.07
Spotted gum	0.54	0.31	0.02

We calibrated the empirical diffusion coefficient by multiplying the empirical formulae (*Appendix A*) with the ratios shown in Table 5.3, with the assumption that the ratio of measured to empirical diffusion coefficient does not change with temperature and humidity. The result was that the simulated and experimental average MC outputs matched more closely for each species as shown in Figure 5.4. The main conclusion of this figure is that the experimental characterisation has to be focused first on mass diffusion, a quite poorly known and sensitive parameter. The following simulation results use the calibrated bound-water diffusion coefficient due to this improved accuracy.

A comparison between the simulated and experimental average MC and temperature during vacuum drying each species in the radial-tangential plane is shown in Fig. 5. The results are provided to illustrate the accuracy of the model compared with semi-industrial scale vacuum drying. Depending on species, the model can accurately predict the average MC during drying within an RMSE error of 1.5 %MC (spotted gum) to 10.4 %MC (jarrah). The model is shown to predict temperature with an error ranging from 5.6 °C (jarrah) to 8 °C (spotted gum). Note that the predictions are excellent for both the averaged moisture content and the temperature, which is generally not obvious. Such good results over a large range of wood species with contrasted behaviour are rather unique.

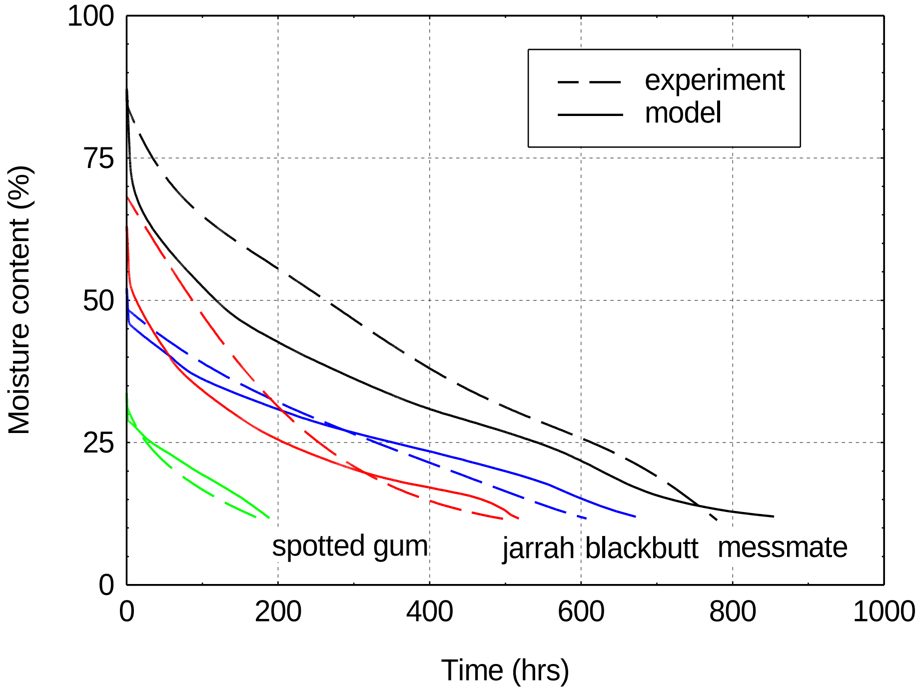

(a)

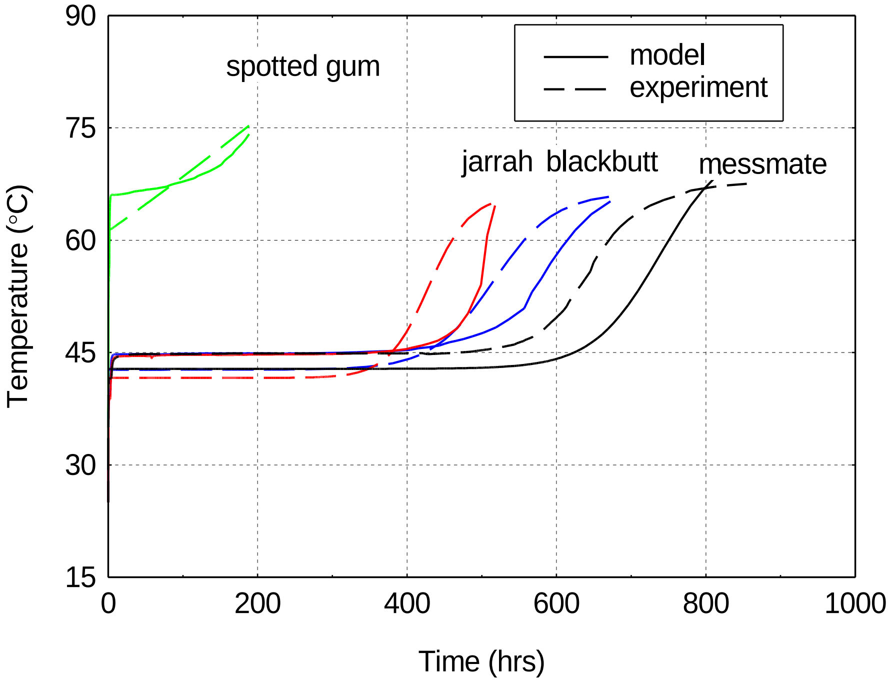

(b)

Figure 5.5 Comparison between simulated and experimental average MC (a) and temperature (b) of vacuum drying each species in the radial-tangential plane

Simulations results comparing the average MC output of vacuum drying in the radial-tangential plane versus vacuum drying in the longitudinal-transverse plane, for messmate and spotted gum, are shown in Figure 5.6. Little difference was observed between average MC curves of the two planes, for both species. This indicates that the measured wood permeability and diffusion coefficient in the longitudinal direction are small enough to limit the effect of longitudinal migration even with the internal overpressure generated by the vacuum-drying configuration.

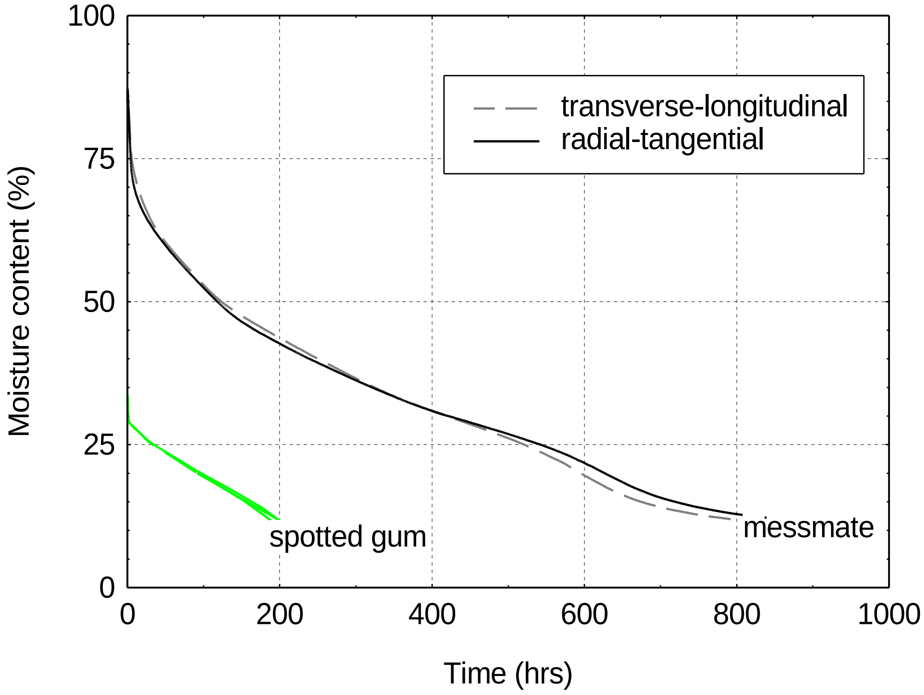

Figure 5.6 Comparison between vacuum drying average MC output simulations for messmate and spotted gum in the radial-tangential (width and thickness) and longitudinal-transverse (length and thickness) planes

A comparison between vacuum and conventional MC gradient drying curves, at different board average MC values, in the longitudinal direction for messmate is shown in Figure 5.7a, and in the board thickness direction in Figure 5.7b. Observation of the MC gradient curves, along the board length, when the average board MC is 65%, 30% and 25% shows higher gradients (range between maximum and minimum values) for conventional drying than for vacuum drying. This may explain why conventionally dried boards of this species were observed to be more prone to end-splitting than vacuum dried boards. It is thought that the greater overpressure between the core of the boards and surrounding conditions allows, partly, to enhance longitudinal water movement and, probably as a main effect, to induce diffusion/convection along the thickness (term $\rho_g\overline{\mathbf{v}}_g$ of equation 5-1) thus reducing drying gradients and associated stress related degrade at the board ends during vacuum drying.

This is a topic for further investigation and stress-strain related modelling. Observation of the MC gradient curves in the longitudinal and thickness directions reveals much more drying occurring in the board thickness direction. This implies that the drying of these species is predominantly by convection and diffusion in the thickness direction, which is also why transverse diffusion was shown to be the second most sensitive parameter.

The accelerated drying rate of vacuum drying compared with conventional drying is mainly due to thermal activation of bound water migration, as the temperature levels are quite significantly higher in the case of vacuum drying, in combination with improved water vapour convection under vacuum.

Using equation 5-14, the model is able to predict the end-point drying time, for both conventional and vacuum drying, within an error of 4 to 11 %, depending on species.

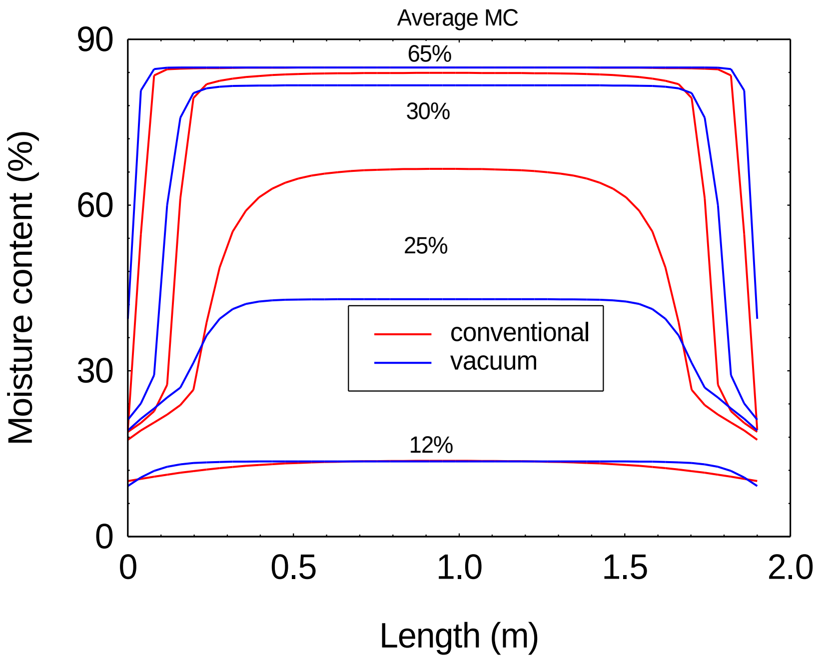

(a)

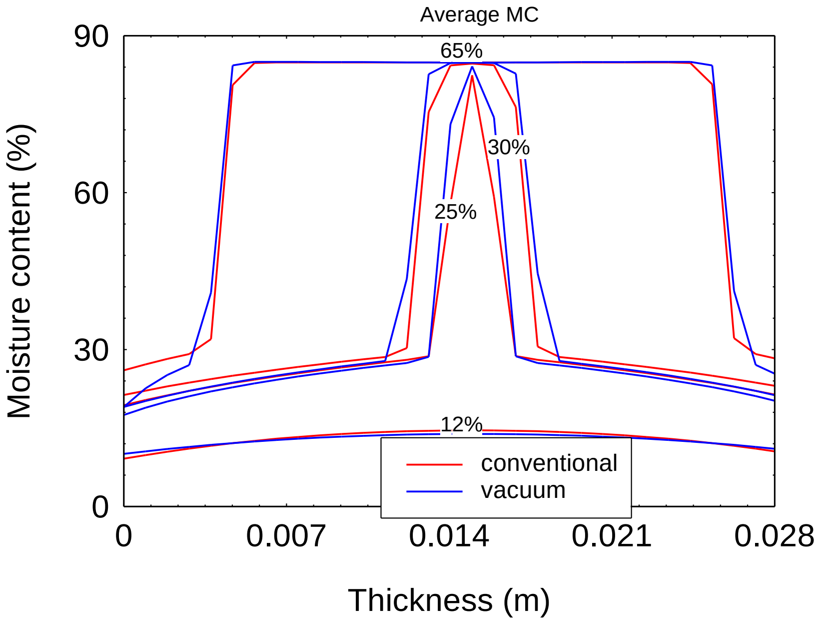

(b)

Figure 5.7 Comparison between vacuum and conventional MC gradient drying curves, at different board average MC values, in the longitudinal (a) and thickness (b) directions and at mid width and thickness, for messmate.

It is stated in Perré [3] that, to reduce wood drying time without decreasing dried quality, the drying conditions must be such that the temperature of the wood is above the boiling point of water. These conditions ensure that an overpressure exists within the wood, creating a pressure gradient that drives moisture from the wood at a faster rate than drying below the boiling point. This is the aim of high temperature convective drying and vacuum drying. Due to the low pressure during our vacuum drying trials and subsequent simulations ($P_{chamber}$ = 0.1 to 0.2 P_{atm}) the boiling point is reduced to around 45 ºC. Drying over the boiling point of water is not the only requirement to develop an overpressure induced accelerated drying rate, free water must also be present meaning that the wood MC must be greater than the fibre saturation point (FSP) [3].

Figure 5.8a&b show the comparison between vacuum and conventional over-pressure (the difference between core gas pressure and pressure at the boundary), generated from model simulations for messmate and spotted gum in the radial-tangential plane. The core MC output, the temperature dependent FSP values (equation 5-10), and the core vapour pressure for each species, are included in the figures. When the MC is above the FSP we expect accelerated drying if sufficient overpressure is present. The point when the core MC and FSP lines meet indicates where FSP is reached on the pressure curve. The results show, for messmate, a substantial overpressure is present during the majority of vacuum drying above the FSP (from approximately 0 to 600 hrs drying), but not for conventional drying where the overpressure is close to zero until the latter part of drying. The stepped overpressure shown at the end of the conventional drying simulations is a result of the ‘stepped’ conventional drying schedules used (The accuracy for the model to predict the final drying time at a final MC of 10% was calculated using:

$$E_{dt} = \frac{|t_e - t_s|}{t_e} \times 100, \qquad (5\text{-}17)$$

where E_{dt} is the drying time error (%), t_e is the experimental drying time and t_s is the simulation drying time.

Table 5.1). The same profile did not occur for the vacuum drying simulations as the drying schedule is ramped gradually with decreasing core MC. The results for messmate show that, when drying above the FSP more overpressure occurs during vacuum drying than conventional drying which contributes to the faster vacuum drying rate observed in experimental trials.

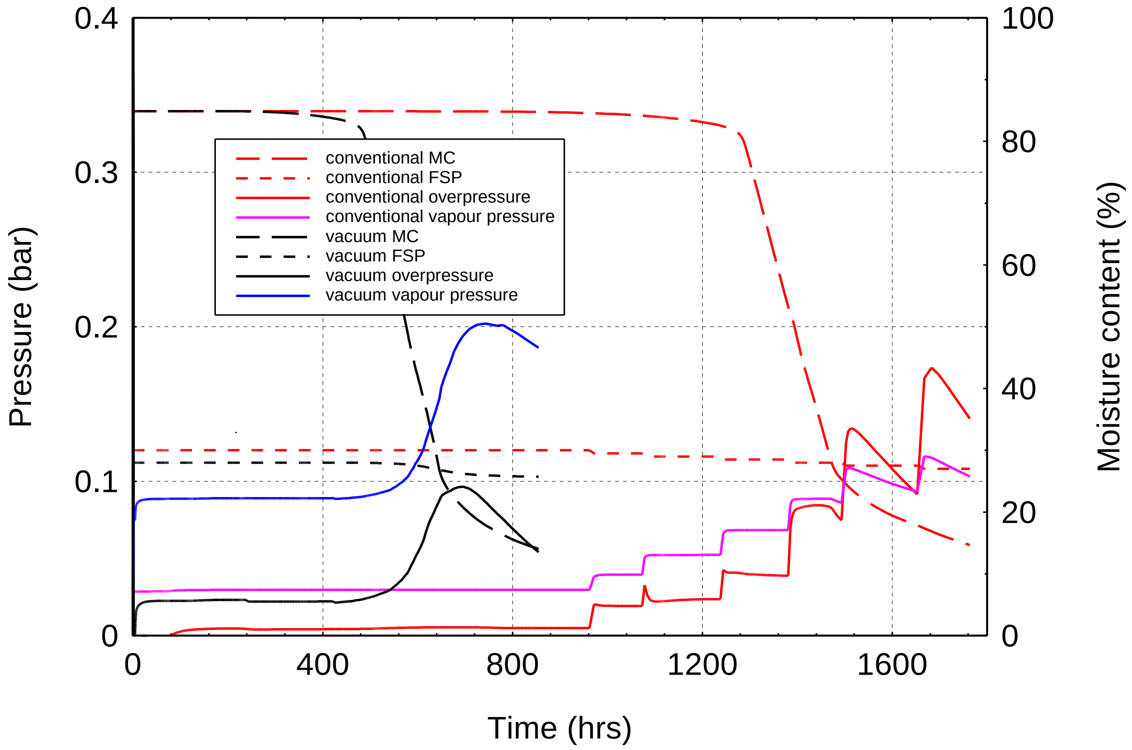

(a)

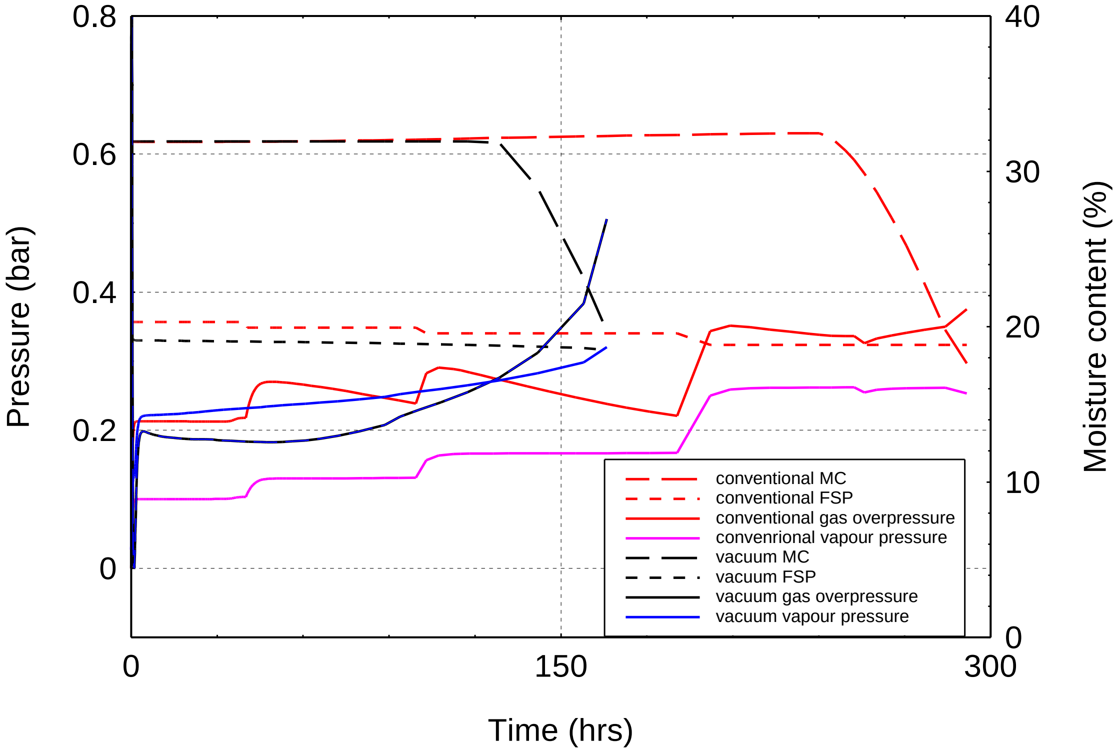

(b)

Figure 5.8 Comparison between vacuum and conventional drying internal-overpressure-output simulations for messmate (a) and spotted gum (b) in the radial-tangential plane, showing MC drying curves and FSP

5.4 Conclusions

A comprehensive heat and mass transfer model was applied to vacuum-drying Australian hardwood species. A highlight of the work was that by using measured diffusion coefficient values to calibrate empirical formula the accuracy of the model was greatly improved.

A sensitivity analysis was performed that focussed on the experimental characterisation on key model parameters, such as the transverse mass diffusivity. The results of the sensitivity study indicated that by using measured values of these key parameters, the model outputs provide excellent agreement with experimental observation despite the large range of species behaviour and variation in wood properties.

In terms of the heat and mass transfer phenomena evident throughout the vacuum drying process, this study confirms that the drying rate is significantly improved as a direct result of the enhanced convective and diffusive transfer along the board thickness. Contrary to softwood, it appears that longitudinal migration provides only a secondary effect.

An important contribution of the modelling work presented here is that not only can the model predict the heat and mass transfer behaviour of a range of hardwood species, it is also flexible enough to predict the behaviour for different types of drying scenarios.

Outcomes of this research provide the hardwood industry with a tool that can accurately determine the vacuum drying rate of spotted gum, messmate, jarrah and blackbutt species. Subsequently, the time required to perform applied drying research can be reduced by measuring a number of key wood properties to provide confidence in simulated outputs.

Chapter 6
Drying stress FEA model

This chapter features the bulk of the published journal article *"Finite element analysis of stress-related degrade during drying of Corymbia citriodora and Eucalyptus obliqua"* submitted for publication after review in the Wood Science and Technology journal on 22 July 2017, where some minor alterations have been made based on reviewers' comments.

Statement of Authorship. This work was divided as follows:

- *Mr. Adam Redman* (Candidate) wrote the majority of the article, built the *Strand7* model, generated measured and empirical input data and conducted simulations.
- *Dr. Henri Bailleres* was involved in providing the methods to input moisture field data into a 3D stress model and failure criteria. His knowledge of the necessary wood mechanics required for the stress model was instrumental.
- *Prof. Benoit Gilbert* whose knowledge of FEA model development and associated software was indispensable. He guided the majority of the modelling work and programed the Python code necessary for the time-dependent simulations.
- *Prof. Ian Turner* guided the work, developed the original *TransPore* model for porous media and assisted in the computational methodology.
- *Dr. Elliot Carr* assisted with developing the refined transverse-longitudinal mesh required to investigate stress at the ends of boards.

- *Prof. Patrick Perr*é guided the work, developed the original *TransPore* model for porous media and assisted in the design of experimental methods.

SIGNED:

DATE:

19/8/2017

6.1 Introduction

Wood drying consists of the removal of water from the wood structure before its intended end use. When freshly sawn, wood contains a large quantity of water, with initial moisture contents of Australian hardwoods ranging from approximately 30 to 120% [117]. If the wood surfaces are left exposed to the atmosphere the board will naturally dry until it reaches an equilibrium moisture content, which is dependent upon the ambient conditions governed by temperature and relative humidity. The equilibrium moisture content generally varies from between 6 to 16% depending on the geographic location and the season. Among other properties, dried wood has the advantage over freshly sawn or ‘green’ wood, of having improved strength properties (i.e. hardness, stiffness, strength), is easier to transport, handle and machine, and in terms of shrinkage and swelling is more stable for end use [151]. This improved stability comes from the moisture content of the wood equalising to its ambient conditions and subsequently undergoing less fluctuation, which is the cause of wood shrinkage and swelling.

Drying wood outdoors under ambient conditions can be a very slow process, particularly for many hardwood species, taking anywhere up to a year or more, depending on the wood species and/or board thickness. Wood drying kilns are employed to accelerate drying by improving and controlling airflow, temperature, humidity and atmospheric pressure properties. Although the types of kiln used to accelerate wood drying are many and varied, they all have the same objective; to dry wood in the fastest and most economical way possible with minimal drying induced degrade relevant to the product end use. However, due to the complexity of wood drying, these three aims influence each other and one must find a balance to optimize the drying process. Drying time is usually restricted by the desired level of acceptable dried quality [3].

Dried quality includes the variation in final moisture content within single and between multiple wood members and degrade, including residual drying stress, distortion, wood cell collapse deformation (where wood cells actually collapse), and external or internal tearing of wood tissue in the form of splits at the board ends (Figure 6.1a) or at the surfaces [152], commonly referred to as ‘surface checks’ (Figure 6.1b). Many eucalypt species, particularly those of low density, are prone to collapse deformation, splitting and checking [108]. Assuming the absence of collapse, no deformation occurs when removing liquid water and dying stresses start doe to shrinkage occurring in the hygroscopic domain. When wood dries, its exterior dries more rapidly than the interior to form a moisture content gradient. Once the outer layers dry below the fibre saturation point (FSP), below which wood starts to shrink, and while the interior is still saturated, stresses are generated because the shrinkage of the outer layers is restricted by the wet interior. Wood material is strongly orthotropic and inhomogeneous, and stresses and cracks that occur during drying are predominantly caused by orthotropic shrinkage [3]. For most species, the shrinkage in the tangential wood direction is generally double that in the radial direction, and the transverse shrinkage is approximately 100 times greater than in the wood longitudinal direction [151]. Rupture of the wood in the form of splits and checks occur if these stresses across the grain exceed the tensile strength. Checks can also occur internally due to stress reversal. Some species are more prone to certain forms of drying induced degrade than others. Degrade depends on a number of factors that are mostly related to wood structure and composition. The factors influencing these characteristics include growing conditions, plantation stands and presence of reaction wood [75].

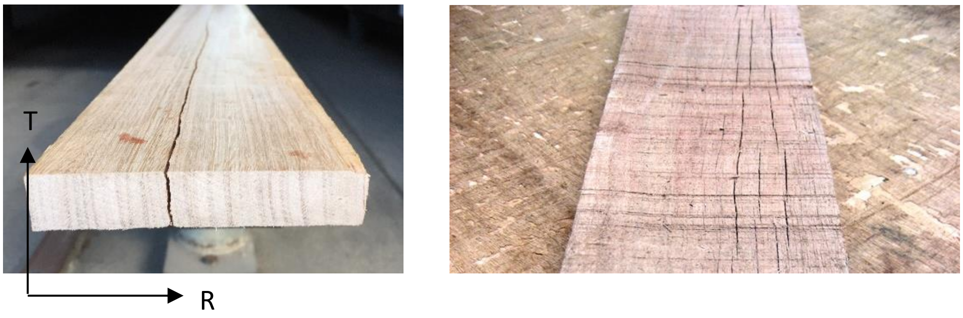

(a) (b)

Figure 6.1 Examples of end split (a) and surface checking (b) stress-induced drying-degrade of messmate boards

The successful control of drying defects in a drying process consists of maintaining a balance between the rate of evaporation of moisture from the surface and the rate of outward movement of moisture from the interior of the wood [3]; therefore controlling the moisture content (MC) gradient will in turn control the magnitude of drying stresses and subsequent susceptibility to surface check and end-split degrade.

Conventional kiln drying with controlled heating, humidity and air-flow under atmospheric pressure conditions is the primary method for drying timber in Australia [1]. In recent years, vacuum drying of hardwood timber (particularly in Europe and the USA) has proven in many applications to be a more economical alternative to conventional kiln drying methods, with similar or better quality outcomes [4, 153, 154]. For this reason, the Australian hardwood timber industry invested in a project to establish the viability of vacuum drying technology for drying four high volume commercial Australian hardwood species with respect to drying quality, time and cost. Moreover, it was recognised that a better knowledge of the material and associated drying behaviour is required to fully optimize the vacuum drying process in the future [3].

A component of the project was to develop a hardwood vacuum drying model [155] based on previous work conducted for softwood species [156]. A two-dimensional, diffusion and permeability based multiphysics heat and mass transfer model was developed by adapting the *TransPore* model used to predict the drying behaviour of softwoods and applying the drying model to Australian hardwood species [157]. *TransPore* was originally developed by Perré and Turner [7, 16] and recently had its accuracy and numerical efficiency enhanced by Carr *et al*. (2013a; 2013b) [71, 72] to include novel strategies such as a variable-stepsize Jacobian-free exponential integer and a dual-scale modelling approach.

As described by Redman [155], a series of vacuum and conventional drying trials was preformed to generate data to validate the heat and mass transfer model using four Australian hardwood species; mature native forest spotted gum (*Corymbia citriodora* Hook), blackbutt (*Eucalyptus pilularis* Sm), jarrah (*Eucalyptus marginata* D.Don ex Sm.), and messmate (*Eucalyptus obliqua* L'Herit.). The species were specifically chosen based on their large commercial volume, and contrasting drying characteristics and wood properties. For example, spotted gum is known to be the most unproblematic species to dry in terms of resistance to drying degrade and has the highest basic density (BD) of 1000 kg/m^3[117]. Alternatively, messmate is one of Australia's most difficult species to dry due to its propensity to collapse, internal and surface check, and has the lowest BD of 630 kg/m^3 [117].

The experimental method used connected vacuum drying trials to conventional drying trials by using long boards that were sawn in half, where one half was used for vacuum drying trials while the other half was used for conventional drying trials. To select a representative subset of the population,100 randomly selected boards were chosen to measure wood properties and quality after drying. Dried quality was quantified by measurements of distribution of average MC and MC gradient, and stress related degrade, including surface checking, end splitting, internal checking and collapse. In the current paper we are only interested in stress-related degrade, and the data produced by Redman *et. al.* [155], expressed as a percentage of degrade existence, from the 100 randomly selected boards, are provided in Table 6.1. This data highlights that:

- messmate is prone to all forms of stress related degrade,
- messmate is the only species exhibiting collapse degrade,
- spotted gum has the lowest overall susceptibility to all the combined forms of degrade, and
- vacuum drying, on average across all tested species, induces only about 60% less surface checking and 80% less end split type degrade than conventional drying.

Table 6.1 Percentage of boards exhibiting drying stress-induced degrade for different species and drying types as reported by Redman et. al. [155]

Species	Drying type	Collapse (%)	Surface check (%)	Internal check (%)	End split (%)
spotted gum	vacuum	0	15	0	7
	conventional	0	17	0	11
jarrah	vacuum	0	7	8	6
	conventional	0	16	12	6
blackbutt	vacuum	0	30	0	4
	conventional	0	83	0	64
messmate	vacuum	100	6	11	10
	conventional	100	29	4	77

n = 100

The development of the heat and mass transfer model presented by Redman *et al.* [30, 75, 146] described the measurement of a number of wood properties deemed essential for accurate modelling, (Perré [17], Salin [25]), for the *TransPore* model input data. The properties measured to achieve accurate modelling results were: wood density, initial MC, fibre saturation point, fibre and vessel porosity, shrinkage, mass diffusivities, desorption isotherm characteristics and gas permeability.

By using the moisture content gradient outputs derived from the heat and mass transfer model described by Redman *et al*. [155], the basis of this study is to simulate and understand stresses that cause the substantial differences in end splitting and surface check degrade observed between conventional and vacuum drying of messmate and spotted gum species. The two-dimensional time-dependent moisture gradient outputs are used as input data to create a three-dimensional stress/strain model in the *Strand7* software [158], using finite element analysis, a method used previously by Ekevad *et. al*. [101, 159] to simulate distortion and shrinkage in boards during drying. As three-dimensional moisture gradient fields were not available for this model, some assumptions were made to extend the two-dimensional field into three-dimensions. Additionally, a simplified drying mechanical model is assumed which includes elastic deformation and moisture induced shrinkage and excludes viscoelastic and mechano-sorptive creep. This assumption forces us to focus on the primary phase of drying, when surface checking and end splitting occurs, which is what we want to achieve. Indeed, it is impossible to model stress reversal with this assumption and to subsequently predict stress induced degrade at the end of drying, such as internal checking. With these assumptions in mind, this work is considered as a feasibility study to investigate the concept of simulating stress-related drying degrade and to stimulate further research in this area.

Investigating the hygro-mechanical effects on the behaviour of wood drying, and associated stress related failure, is the primary objective of this research. More specifically, with the use of experimental wood properties and input moisture content field data we aim to develop a predictive 3D stress-strain finite element analysis (FEA) model allowing prediction of the development of stress related end splitting and surface checking degrade during conventional and vacuum wood drying. Two Australian hardwood species were targeted, messmate (*Eucalyptus obliqua*) and spotted gum (*Corymbia citriodora*) as these species contrast, in terms of wood properties, drying rates and stress degrade susceptibility.

6.2 Materials and methods

A flow chart of the modelling approach used for this study is provided in Figure 6.2. It consists of a four stage sequential process. The first stage involves the use of the *TransPore* model to generate moisture content field data in the Tangential (T)-Longitudinal(L) plane (thickness x length), which is then extruded across the radial (R) direction of the board (width) to create 3D moisture content fields during drying.

The second, third and fourth stages involve the use of the *Strand7* model for predicting the elastic and moisture induced shrinkage strains, describing the geometric configuration, running the model and analysing the failure criteria. The modelling approach is described in more detail in the following sections.

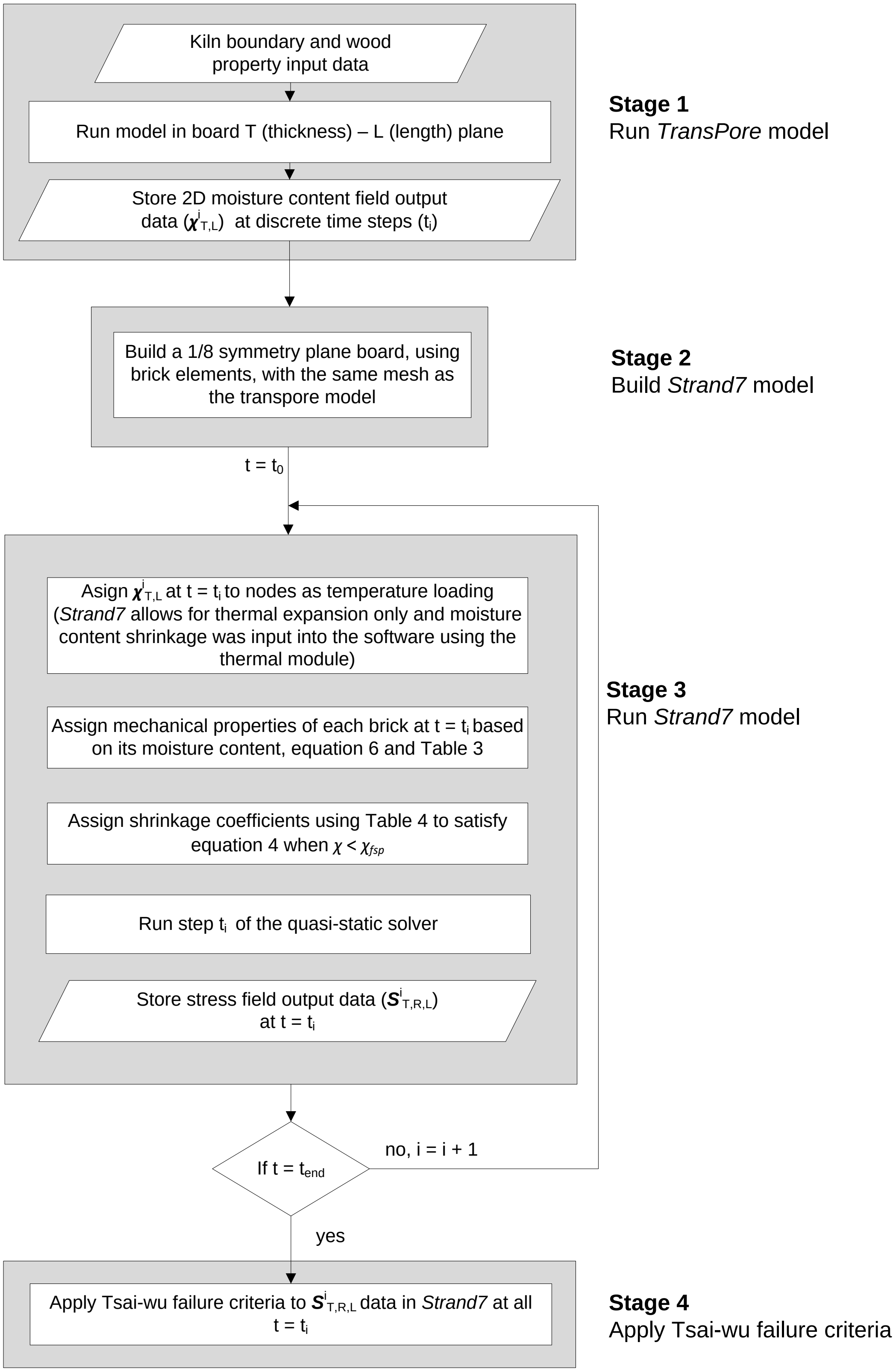

Figure 6.2 Flow chart of TransPore and Strand7 FEA modelling approach used

6.2.1 Heat and mass transfer formulation

Heat and mass transfer modelling, using *TransPore* is described in detail by Redman *et al*. [155]. For vacuum drying, the external conditions supplied to *TransPore* were measured directly using kiln conditions from drying trials. At any point in time, the external conditions were vacuum pressure, temperature and relative humidity.

For conventional kiln drying simulations, the external conditions used in the *TransPore* model were temperature and relative humidity, and the kiln pressure was held constant at atmospheric pressure. The conditions were based on the recommended industry drying schedules for these species in accordance with those outlined in Rosza and Mills [150].

The kiln drying schedules used are shown in Table 6.2 and are represented as temperature and relative humidity (RH) change points based on average board moisture content. For the vacuum drying simulations, the vacuum pressure fluctuated between 100 and 200 mbar (as measured during experiments), and for conventional drying simulations, it was held at a constant 1000 mbar. It should be noted that for conventional drying schedules, the temperature and RH set points were instantaneously stepped when the average moisture content change point is reached. This is not the case for vacuum drying schedules where the temperature and RH were 'ramped' between set points, based on the continuous reduction of average moisture content as drying progresses. Redman *et. al*. [155] provided more details on these methods including the wood property input data used for spotted gum and messmate species.

Table 6.2 Conventional and vacuum drying schedules used for spotted gum and messmate simulations expressed as temperature (Temp.) and relative humidity (RH)

Moisture content change point (%)	spotted gum				messmate			
	Conventional		Vacuum		Conventional		Vacuum	
	Temp. (°C)	RH (%)	Temp. (°C)	RH (%)	Temp. (°C)	RH (%)	Temp. (°C)	RH (%)
>70	45	83	64	78	25	77	44	85
70 - 60	45	83	65	76	25	77	44	85
60 - 50	45	78	66	75	25	77	45	82
50 - 40	45	78	66	73	30	73	45	75
40 – 35	45	78	67	70	30	73	45	73
35 – 30	50	79	67	70	35	75	45	73
30 – 25	55	64	69	66	40	71	58	65
25 – 20	60	58	71	55	45	60	64	65
20 – 15	70	47	75	40	50	54	72	35
15 - final	70	35	80	55	55	40	80	55

Wood is an orthotropic material with three directions: radial (R), tangential (T) and longitudinal (L) (Figure 6.3a). For all simulations presented in this study (*TransPore* and *Strand7*), the board thickness is in the T direction, width the R direction and length the L direction, where thickness < width < length. The *TransPore* model used in this study is limited to two-dimensions and was used to simulate drying in the board tangential (T) and longitudinal (L) directions. This plane was used, as it allows investigation of the evolution of moisture gradients over time at the board ends and wide surfaces, the areas of interest for end splitting and surface checking investigations, and the board thickness is the direction that most drying takes place. Furthermore, during industrial drying, boards are placed in rows such that their sides are touching, substantially limiting drying on the board width direction, and a limited moisture gradient is therefore assumed along the R direction in this study. A schematic of the *TransPore* board model and location of the T-L plane are shown in Figure 6.3a.

A triangular structured mesh was constructed. A magnified section of the mesh is shown in Figure 6.3b. The T-L plane dimension used was 1900 mm long x 30 mm thick, the same dimension of boards used in drying trials described by Redman *et. al.* [155].

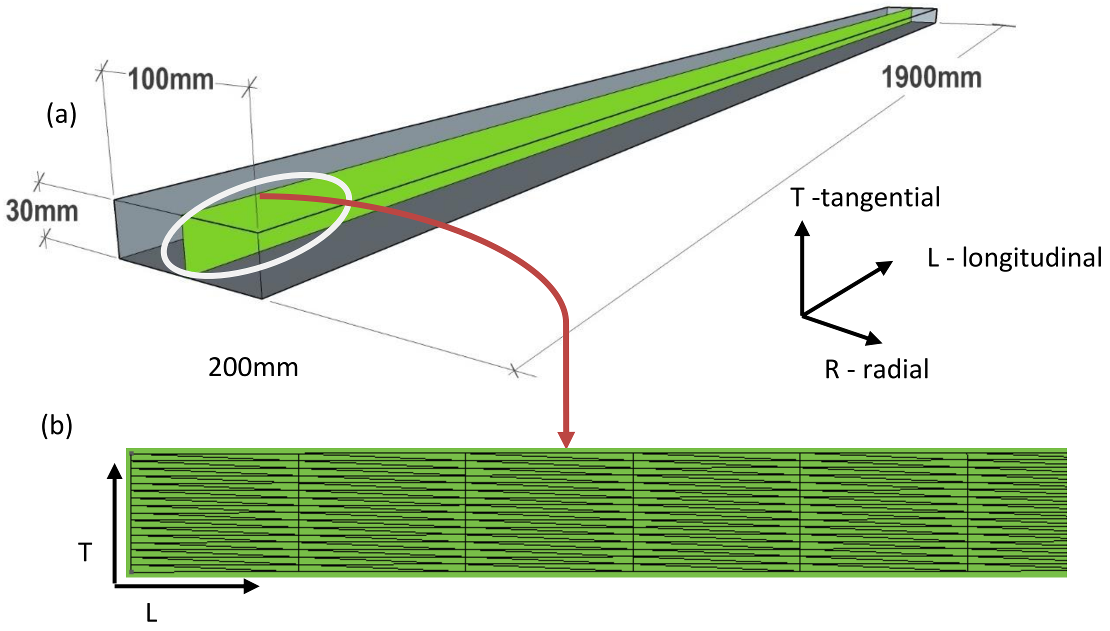

Figure 6.3 Schematic of board (a) showing the position of the tangential (T)-longitudinal (L) mesh and magnified section of the mesh (b) used for the TransPore model.

TransPore was used to generate moisture content field data $\mathcal{X}_{T,L}^{i}$ in the T-L plane starting at time $t_1 = 0$ iterating by time steps t_i (determined by the *TransPore* numerical solution procedure) until the final average moisture content of the board reached 12% at which point the simulation is terminated. The result is a stored series of seventy $\mathcal{X}_{T,L}^{i}$ field data at discrete time intervals t_i. Data was generated for spotted gum and messmate for both vacuum and conventional drying regimes. The initial average MC of spotted gum and messmate measured from drying trials was 32 and 85% respectively. These are typical initial moisture content values for these species [160].

An example of he *TransPore* model moisture content field visualisation, generated for vacuum drying of messmate is provided in Redman *et. al.* [155].

6.2.2 Geometric configuration

As stress induced drying degrade occurs in three dimensions (at the board surface, ends and internally) we desired to build a three-dimensional stress/strain FEA model using the two-dimensional *TransPore* data. To achieve this, the moisture content field $\mathcal{X}^{i}_{T,L}$ generated by *TransPore* was extruded in the board width direction to form a series of triangular brick elements. More specifically, this quasi three-dimensional model consists of a series of the same T-L moisture content fields ($\mathcal{X}^{i}_{T,L}$) using the mesh shown in Figure 6.4b, extruded in the R direction to form the moisture content field ($\mathcal{X}^{i}_{T,L,R}$) within the three dimensional mesh shown in Fig. 4b. To reduce computational time, the *Strand7* FEA model was built as a 1/8 board symmetry model of the board as shown in Figure 6.4a. The T, R, L direction fixed boundary conditions are shown for the three symmetry surfaces. A magnified view of the structure of the three-dimensional *Strand7* model used, is shown in Figure 6.4b.

The *Strand7* FEA model requires three sets of input data: the moisture content field data from *TransPore*, wood material and mechanical property data, and shrinkage coefficient data. Before explaining the procedure used to run the *Strand7* FEA program the mechanical and physical formulations must be defined.

6.2.3 Mechanical formulation

As mentioned earlier, when wood dries it loses water initially from its surface. The surface shrinks first but is restrained by the bulk of the wood that is still saturated. Therefore, the strain field generated by moisture content profiles is not geometrically compatible, resulting in the superposition of a strain field related to a stress field. Mårtensson and Svensson [92] describe the total strain tensor $\boldsymbol{\varepsilon}$ in a board as being comprised of four components:

$$\boldsymbol{\varepsilon} = \boldsymbol{\varepsilon}^{e} + \boldsymbol{\varepsilon}^{\mathcal{X}} + \boldsymbol{\varepsilon}^{ms} + \boldsymbol{\varepsilon}^{c}, \qquad (6\text{-}1)$$

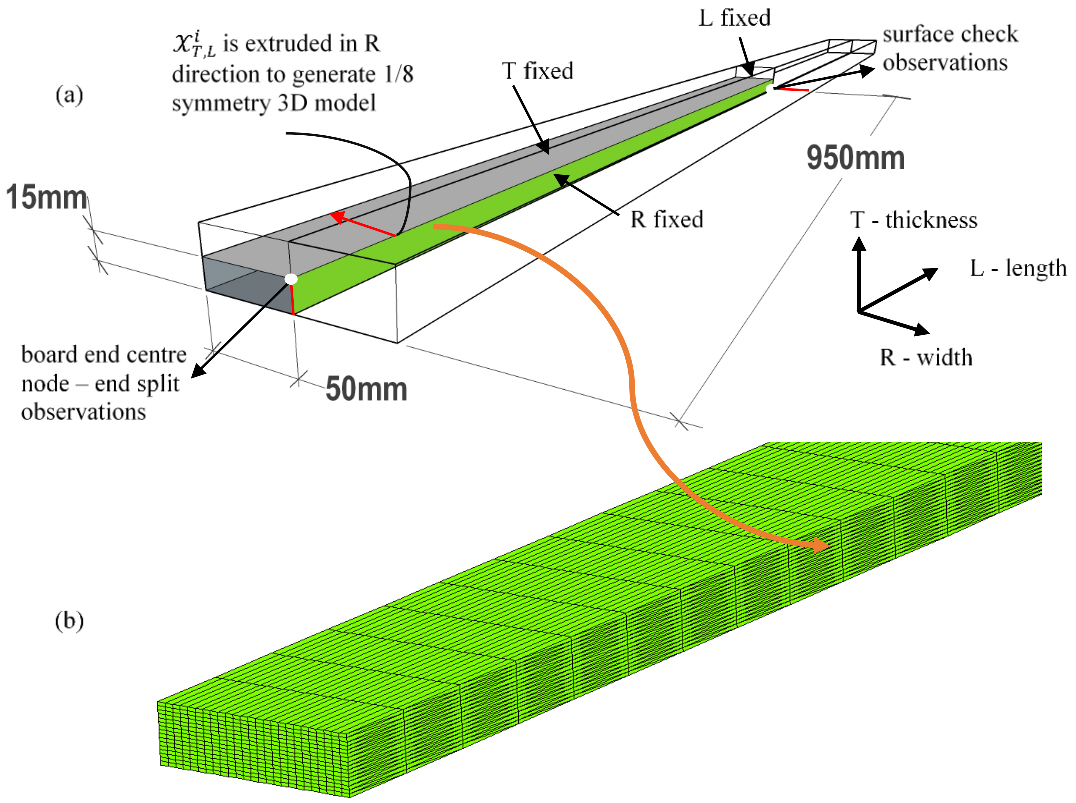

Figure 6.4 Strand7 FEA model structure build, showing the TransPore moisture field $\mathcal{X}^{i}_{T,L}$(a) which is extruded in the width direction and reduced to a 1/8 symmetry model to produce a 3D model of triangular brick elements as shown in the magnified section (b). The T, R, L fixed boundary conditions are shown for the three symmetry surfaces (a).The points od observation for end splitting and surface checking are shown also.

where $\boldsymbol{\varepsilon}^{e}$ is the elastic strain, $\boldsymbol{\varepsilon}^{\mathcal{X}}$ is the strain associated with moisture induced free shrinkage, $\boldsymbol{\varepsilon}^{\boldsymbol{ms}}$ is the mechano-sorptive strain (the effect due to the interaction between the change in volume due to a change in moisture content and that due to an applied stress) and $\boldsymbol{\varepsilon}^{\boldsymbol{c}}$ is the time dependent (viscoelastic) creep strain under load, independent of moisture content but strongly dependent on temperature.

Previous research shows that the non-elastic, stress relieving components of drying stresses, namely viscoelastic and mechano-sorptive creep, are responsible for stress reversal to occur in the latter part of drying, when the average board moisture content is around the FSP (20-30 %) [26, 82, 161]. After stress reversal through a board cross-section, compressive stresses then occur in the outer layers of a board and tensile stresses in the core layers, effectively eliminating the possibility of end splitting and surface checking to occur under these conditions. For this reason, this model includes just the elastic drying stresses and the subsequent stress and failure formation results are analysed between the board initial moisture content and board average FSP conditions (i.e. 24.5% for spotted gum and 30% for messmate) when end and surface splitting have occurred. As the analysis ends when the board reaches average FSP, the outer board layers are below FSP which generates the elastic stresses observed.

Consequently, the focus of this work was to observe simulated end split and surface checking failure occurring during the primary phase of drying and considering only the elastic and moisture induced shrinkage strains (i.e. equation 6-1 becomes $\boldsymbol{\varepsilon} = \boldsymbol{\varepsilon}^{\boldsymbol{e}} + \boldsymbol{\varepsilon}^{\boldsymbol{X}}$). By doing so, this work is considered as a feasibility study to investigate the concept of simulating stress-related drying degrade for further research. The effects of excluding the $\boldsymbol{\varepsilon}^{\boldsymbol{ms}}$ and $\boldsymbol{\varepsilon}^{\boldsymbol{c}}$ strain components on the results is further discussed at the end of the paper.

In the wood orthotropic radial (R), tangential (T) and longitudinal (L) directions with reference to its anatomy, material elastic stress is related to the elastic strain by the generalised Hooke's law [98], described by:

$$\boldsymbol{\varepsilon}^{\boldsymbol{e}} = \boldsymbol{C\sigma}, \qquad (6\text{-}2)$$

where

$\boldsymbol{\sigma}$ = stress vector $\boldsymbol{\sigma} = [\sigma_L \quad \sigma_T \quad \sigma_R \quad \tau_{RT} \quad \tau_{LT} \quad \tau_{LR}]^T$

$\boldsymbol{\varepsilon}^{\boldsymbol{e}}$ = elastic strain vector $\boldsymbol{\varepsilon}^{\boldsymbol{e}} = [\varepsilon_L \quad \varepsilon_T \quad \varepsilon_R \quad \gamma_{RT} \quad \gamma_{LT} \quad \gamma_{LR}]$

$\boldsymbol{C}$ = compliance matrix.

The compliance matrix is given by

$$\mathbf{C} = \begin{bmatrix} \frac{1}{E_L} & \frac{-\upsilon_{RL}}{E_R} & \frac{-\upsilon_{TL}}{E_T} & 0 & 0 & 0 \\ \frac{-\upsilon_{LR}}{E_L} & \frac{1}{E_R} & \frac{-\upsilon_{TR}}{E_T} & 0 & 0 & 0 \\ \frac{-\upsilon_{LT}}{E_L} & \frac{-\upsilon_{RT}}{E_R} & \frac{1}{E_T} & 0 & 0 & 0 \\ 0 & 0 & 0 & \frac{1}{G_{RT}} & 0 & 0 \\ 0 & 0 & 0 & 0 & \frac{1}{G_{LT}} & 0 \\ 0 & 0 & 0 & 0 & 0 & \frac{1}{G_{LR}} \end{bmatrix}, \qquad (6\text{-}3)$$

where the material behaviour is described by the following parameters:

E_L, E_T, E_R = Young's moduli

G_{RT}, G_{LT}, G_{LR} = shear moduli

$\upsilon_{RT}, \upsilon_{LT,}\upsilon_{LR}, \upsilon_{RL}, \upsilon_{LT}, \upsilon_{LR}$ = Poisson's ratios;

with $\upsilon_{RT} = \upsilon_{TR} \times \frac{E_R}{E_T}$; $\upsilon_{RL} = \upsilon_{LR} \times \frac{E_R}{E_L}$; $\upsilon_{LT} = \upsilon_{LT} \times \frac{E_T}{E_L}$.

The moisture induced shrinkage strain is dependent on the rate of change of $\mathcal{X}_b$, where $\mathcal{X}_b$ represents the bound water content at a point in space and time and is given by:

$$\left| \begin{array}{ll} \boldsymbol{\varepsilon}^{\boldsymbol{\mathcal{X}}} = \boldsymbol{\alpha}(\mathcal{X}_b - \mathcal{X}_{fsp}), & \text{if } \mathcal{X}_b \leq \mathcal{X}_{fsp} \\ \boldsymbol{\varepsilon}^{\boldsymbol{\mathcal{X}}} = 0, & \text{if } \mathcal{X}_b > \mathcal{X}_{fsp} \end{array} \right. \qquad (6\text{-}$$

4)

where $\boldsymbol{\alpha}$ is defined as:

$$\boldsymbol{\alpha} = [\alpha_L \quad \alpha_R \quad \alpha_T \quad 0 \quad 0 \quad 0]^T, \tag{6-5}$$

and α_L, α_R and α_T are material shrinkage coefficients of moisture induced strain and $\mathcal{X}_{fsp}$ is the saturation point. The shrinkage occurs only with a change of bound water [46], i.e. when $\mathcal{X}_b \leq \mathcal{X}_{fsp}$. The coefficients and saturation points $\mathcal{X}_{fsp}$ used in this study are detailed further in the following section.

6.2.4 Physical formulation

Material properties were established from the literature for the messmate and spotted gum species and consisted of (i) the elastic and shear moduli, and Poisson's ratios required for the elastic strain compliance matrix (equation 6-3), (ii) the fibre saturation point ($\mathcal{X}_{fsp}$), and (iii) the shrinkage coefficients for moisture induced strain (equation 6-5).

The compliance matrix mechanical properties are updated in *Strand7* related to the moisture content of the element. Their value at 12% and $\mathcal{X}_{fsp}$ moisture content is calculated using the method developed by Guitard and El Amri [162]. Their method is based on a regression analysis of literature data regarding density and moisture content versus Young's/shear moduli and Poisson's ratios for 45 hardwood species. The air-dried density at 12% moisture content and $\mathcal{X}_{fsp}$ values for spotted gum and messmate measured by Redman *et al.* [30] were used as input parameters (see Table 6.3) into the Guitard and El Amri [162] hardwood regression equation. Above $\mathcal{X}_{fsp}$ the Young's and shear modulus values are assumed to be constant [163]. When $\mathcal{X}_b \leq \mathcal{X}_{fsp}$ the Young's and shear modulus values are calculated using the non-linear equation (6-6) from Kretschmann [164] incorporating the values at 12% moisture content and $\mathcal{X}_{fsp}$ calculated using the Guitard and El Amri [162] method:

$$P = P_{12}\left(\frac{P_{12}}{P_{fsp}}\right)^{\left(\frac{12-\mathcal{X}_b}{\mathcal{X}_{fsp}-12}\right)},\ when\ 0 \leq\ \mathcal{X}_b \leq \mathcal{X}_{fsp}, \qquad (6\text{-}6)$$

where P is the modulus value at moisture content $\mathcal{X}_b$, $P_{12}$is the same property at 12% moisture content, P_{fsp} the same property for green wood at the fibre saturation point $\mathcal{X}_{fsp}$.

Table 6.3 Fibre saturation moisture content $\mathcal{X}_{fsp}$, air-dry density and elastic strain compliance-matrix input values at moisture content $\mathcal{X}$: including Young's moduli E, shear moduli G and poison's ratios [30, 162]. Below$\mathcal{X}_{fsp}$the propertied are calculated according to equation (6-6).

Species	$\mathcal{X}_{fsp}$ (%)	Air-dry density (kg/m³)	X (%)	E (GPa)			G (GPa)			Poisson's ratios					
				E_R	E_T	E_L	G_{RT}	G_{LT}	G_{LR}	ν_{RT}	ν_{RL}	ν_{TR}	ν_{TL}	ν_{LR}	ν_{LT}
spotted gum	24.5	1010	≥24.5	2.1	1.4	19.9	0.5	1.3	1.6	0.64	0.06	0.44	0.04	0.41	0.45
			12	3.2	2.2	22.7	0.8	1.7	2.0						
messmate	30.0	700	≥30.0	1.0	0.6	13.7	0.2	0.7	1.0	0.66	0.06	0.44	0.04	0.39	0.45
			12	2.2	1.3	16.7	0..5	1.1	15						

The shrinkage values for each species (α_L, α_R and α_T)expressed as % strain per % change in $\mathcal{X}_b$, used for the moisture induced shrinkage strain calculation (equation 6-4), in each wood direction were derived from Redman *et al.* [30] The values for spotted gum are $\alpha_L = 0.001, \alpha_R = 0.374$ and $\alpha_T = 0.385$, and for messmate are $\alpha_L = 0.001, \alpha_R = 0.274$ and $\alpha_T = 0.395$.

6.2.5 Numerical solution

The following finite element formulation in*Strand7* refers to the model flow chart provided in Figure 6.2. The heat transfer model in *Strand7* is used to generate the moisture induced shrinkage as the physical equations between the two phenomenon are identical.

Starting at time t = 0 and iterating by time steps t$_i$ the following procedure was performed for each t$_i$:

- The *TransPore* moisture content field data $\mathcal{X}_{T,L}^{i}$ is inserted into the *Strand7* 1/8 symmetry plane model structure at the nodes in the T-L planes (see *Geometric configuration* above) as a temperature load at the nodes.
- The moisture content of each triangular brick (prism) element is calculated as the average of its nodal values (6 per brick). The material properties are assigned to each triangular brick element based on equations (6-6) and Table 6.3 and the calculated moisture content of the element.
- The shrinkage coefficients were assigned to each triangular brick element as thermal expansion coefficients. The coefficients are updated at each iteration so shrinkage only occurs following equation (6-4) when $\mathcal{X}_b \leq \mathcal{X}_{fsp}$.
- The*Strand7* quasi-static solver is run to follow the evolution of the stress related field during drying. The non-linearity is considered herein by updating the mechanical properties and occurrence of shrinkage below $\mathcal{X}_{fsp}$ in previous steps at each iteration of the quasi-static solver.
- The three-dimensional stress-field data $S_{R,T,L}^{i}$ are then stored at each iteration.

The iteration is completed when the last input moisture content field $\mathcal{X}_{T,L}^{end}$

has been processed.

6.2.6 Tsai-Wu criterion

Failure theory is a scientific tool for predicting failure of materials under certain loads or stresses. It is mathematically expressed as a failure criterion that varies for different materials. Previous studies by Cabrero *et al*. [109] and Mascia and Simoni [110], investigated a number of different failure criteria for wood and concluded that the Tsai Wu failure criterion is well suited to wood, thanks to its ability to deal with anisotropic media.

As our investigations are interested in board end splitting and surface checking, the Tsai-Wu criterion was applied to the stresses in the board thickness (T) and width (R) directions only.

The Tsai-Wu criteria is a quadratic, stress-based criterion where failure is deemed to occur when the following condition is satisfied:

$$A + B + C + D + E + F \geq 1 \tag{6-7}$$

where the equation (6-7) parameters are defined in the radial-tangential directions as [111]:

$$A = \frac{\sigma_{TT}^2}{\sigma_{TTt}^u \sigma_{TTc}^u} \ , \tag{6-8}$$

$$B = \frac{\sigma_{RR}^2}{\sigma_{RRt}^u \sigma_{RRc}^u} \ , \tag{6-9}$$

$$C = \frac{\tau_{TR}^2}{(\tau_{TR}^u)^2} \ , \tag{6-10}$$

$$D = \left(\frac{1}{\sigma_{TTt}^u} - \frac{1}{\sigma_{TTc}^u}\right) \sigma_{TT} \ , \tag{6-11}$$

$$E = \left(\frac{1}{\sigma_{RRt}^u} - \frac{1}{\sigma_{RRc}^u}\right) \sigma_{RR} \ , \tag{6-12}$$

$$F = \frac{2F^{*}_{TR}\sigma_{TT}\sigma_{RR}}{\sqrt{\sigma^{u}_{TTt}\sigma^{u}_{TTc}\sigma^{u}_{RRt}\sigma^{u}_{RRc}}}. \tag{6-13}$$

In equations (6-8) to (6-11), the terms σ_{TT} and σ_{RR} represent the calculated stress in the orthotropic directions T and R, respectively, and σ^{u}_{TTt}, σ^{u}_{TTc}, σ^{u}_{RRt} and σ^{u}_{RRc} represent the ultimate (u) tension (t) and compression (c) stress in the T and R directions. The shear strengths in the T-R plane are represented by τ^{u}_{TR}. The F^{*}_{TR} term in equation (6-13) is the *interaction coefficient* and is difficult to determine [109]. Tsai [112] proposed using the value $F^{*}_{TR} = -0.5$, which corresponds to the generalised Von Misses criterion [109]. This value is used for this analysis. Thus, in the wood T-R plane, using the proposed interaction coefficient, the Tsai-Wu failure criteria equations (6-7) to (6-13) can then be expressed as:

$$\frac{{\sigma_{TT}}^{2}}{\sigma^{u}_{TTt}\sigma^{u}_{TTc}} + \frac{{\sigma_{RR}}^{2}}{\sigma^{u}_{RRt}\sigma^{u}_{RRc}} + \frac{{\tau_{TR}}^{2}}{{\tau^{u}_{TR}}^{2}} + \left(\frac{1}{\sigma^{u}_{TTt}} - \frac{1}{\sigma^{u}_{TTc}}\right)\sigma_{TT}$$

$$+\left(\frac{1}{\sigma^{u}_{RRt}} - \frac{1}{\sigma^{u}_{RRc}}\right)\sigma_{RR} - \frac{\sigma_{TT}\sigma_{RR}}{\sqrt{\sigma^{u}_{TTt}\sigma^{u}_{TTc}\sigma^{u}_{RRt}\sigma^{u}_{RRc}}} \geq 1. \tag{6-14}$$

The ultimate radial and tangential tensile and compression stresses, and the ultimate radial/tangential shear stresses were calculated via regression analysis ($R^2 = 0.8$ to 0.9) of density versus ultimate stress data measured for 66 hardwood species from literature in Kretschmann [164], and are presented in Table 6.4.

Table 6.4 Tension, compression and shear ultimate failure values in MPa for failure criteria calculations[164]

Species	σ^{u}_{Tt}	σ^{u}_{Rt}	σ^{u}_{Lt}	σ^{u}_{Tc}	σ^{u}_{Rc}	σ^{u}_{Lc}	τ^{u}_{TR}	τ^{u}_{LT}	τ^{u}_{LR}
spotted gum	11.9	11.9	152.0	29.5	29.5	49.6	6.5	26.2	26.2
messmate	9.1	9.1	122.5	15.3	15.3	35.6	4.57	18.3	18.3

6.2.7 Simulations

The simulated evolution of the Tsai-Wu failure criteria over time was only investigated at the areas where we experimentally observed end splitting and surface checking in the boards. For end splitting this is at the end of the board and for surface checking this is on the board surface. For end splitting, peak failure was investigated at the end of the modelled board both at the central element and the line of elements through the board thickness, as shown in Figure 6.4a. Similarly, the evolution of failure criteria related to surface checking was investigated at the central surface brick of the board and across the width of the board's surface as shown in Figure 6.4b.

All of the Tsai-Wu failure criteria results presented, use the centroid values of the *Strand7*brick elements. The *Strand7* software calculates the Tsai-Wu data (equation 6-14) at time t = t_i using the two-dimensional stress-field data $S_{R,T}^{i}$ (i = 1 to n) generated previously and allows it to be visualised.

6.3 Results and discussion

An example of the evolution of the Tsai-Wu failure criteria for conventionally dried messmate, focusing on the internal central location of the board end, at various stages of reducing moisture content during drying, is shown in Figure 6.5. Figure 6.5a a shows a schematic of the board symmetry plane and indicates the location of the observed failure in subsequent images. In this example, the initial average moisture content was 85%. Figures 6.5b-f show the evolution of the Tsai-Wu failure at the average board moisture contents of 85%, 40%, 38%, 36% and 33%.The maximum failure criteria is found to occur first along the centre of the board end, in the width direction, and intensifies as drying progresses, with the centre-face of the board-end peak failure (position of white dot in Figure 6.5) occurring when the average board moisture content reaches 38% (Figure 6.5d). The location of the simulated failure criteria indicates that end split failure is likely to occur anywhere along the width of the board but experimental observations showed that end splitting occurred mainly at mid-width of the board end as shown in Figure 6.1a.

The difference between the locations of simulated versus observed end split failure is likely an effect of using the same two-dimensional T-L cross-sectional moisture content profiles along the board width direction (R). Similarly, the large red failure zone at the board edge is also likely due to the expansion of the 2-dimensional MC field to 3 dimensions. Excluding the moisture gradient in this direction reduces the simulated anisotropic stress field at the corners and edges of the board, which may result in an under prediction of the location of end split at the board end.

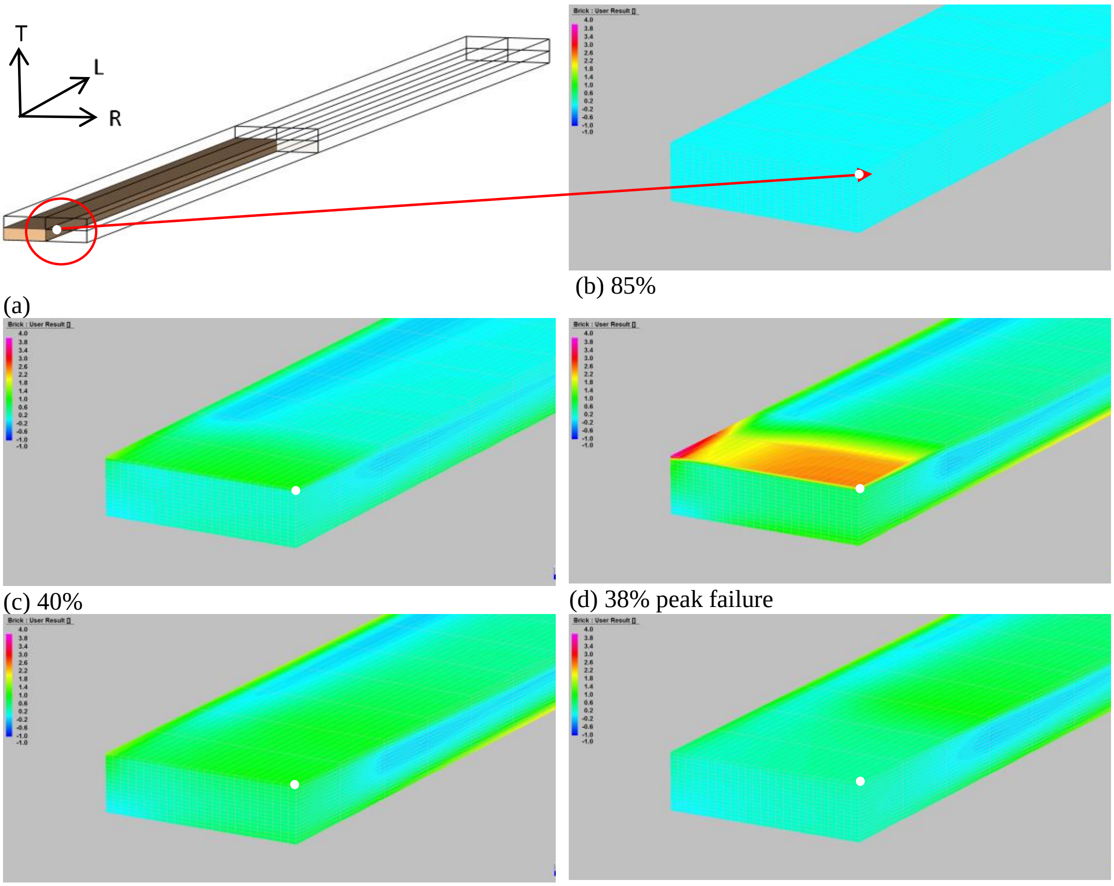

(a)

(b) 85%

(c) 40%

(d) 38% peak failure

(e)36%

(f) 32%

Figure 6.5 Evolution of Tsai-Wu failure at the board end 1/8th symmetry model (a), for conventionally dried messmate, at average board moisture contents 85% (b), 40% (c), 38% peak failure (d), 36% (e) and 32%. The white dot represents the centre of the board end-face.

The Tsai-Wu failure criteria, plotted against the reduction of average moisture content during drying, at the board-end centre-node (white dot Figure 6.5a), for conventional and vacuum dried messmate and spotted gum, is shown in Figure 6.6a. The vacuum and conventional drying temperatures for messmate are also shown. The results indicate that the maximum Tsai-Wu failure for messmate conventional drying (4.5) is approximately 4 times higher than messmate vacuum drying (1.3), 4 times higher than spotted gum conventional drying (1.2) and 4 times higher than spotted gum vacuum drying (1.1). These results appear to be consistent with the magnitude of end splitting observed in drying trials reported by Redman [29]. The observed percentage of end split failure (Table 6.1) for messmate conventional drying (77%) was comparably 8 times higher than messmate vacuum drying (10%), 7 times higher than spotted gum conventional drying (11%) and 10 times higher than spotted gum vacuum drying (7%). The high susceptibility for conventionally dried messmate to end-split during drying compared to vacuum drying and both forms of spotted gum drying, was both predicted by the model and observed during the trials.

The extent of end splitting and surface checking may be exacerbated by the drying schedule itself. Observation of the Tsai-Wu failure plot for conventional drying of messmate shows a sharp step in the curve. This is directly related to the first temperature step in the drying schedule as shown by the corresponding conventional drying temperature plot (Figure 6.6a). These sharp step is not present on the messmate vacuum drying curve, which corresponds to the constant vacuum drying temperature plot. In this case, the temporal evolution of the Tsai criterion is much smoother, with a maximum value at ca. 55% of averaged MC: this evolution is therefore likely to be due to internal transfer in the board rather than to an artefact produced by a sudden evolution of the kiln conditions. An important observation is that using a similar ramped approach for conventional drying schedules should be considered by industry.

Figure 6.6b shows the Tsai-Wu failure in the board thickness direction, at the centre of the board-end (line as shown in Figure 6.5b), when maximum failure occurs. For messmate, maximum failure occurred when the average board moisture content reached 38% for conventional drying, and 56% for vacuum drying. For spotted gum, maximum failure occurred when the average board moisture content reached 24.5% for vacuum drying and 26% for conventional drying from initial average moisture content to FSP (24.5%). The results are mirrored to show the full board thickness and display a substantially steeper gradient of Tsai-Wu failure for messmate conventional drying compared to the other drying scenarios. As drying stress gradients align with moisture content gradients it seems that the overpressure produced by vacuum drying [155] contributes to a flatter moisture content/stress gradient at the end of the board with less susceptibility to end splitting.

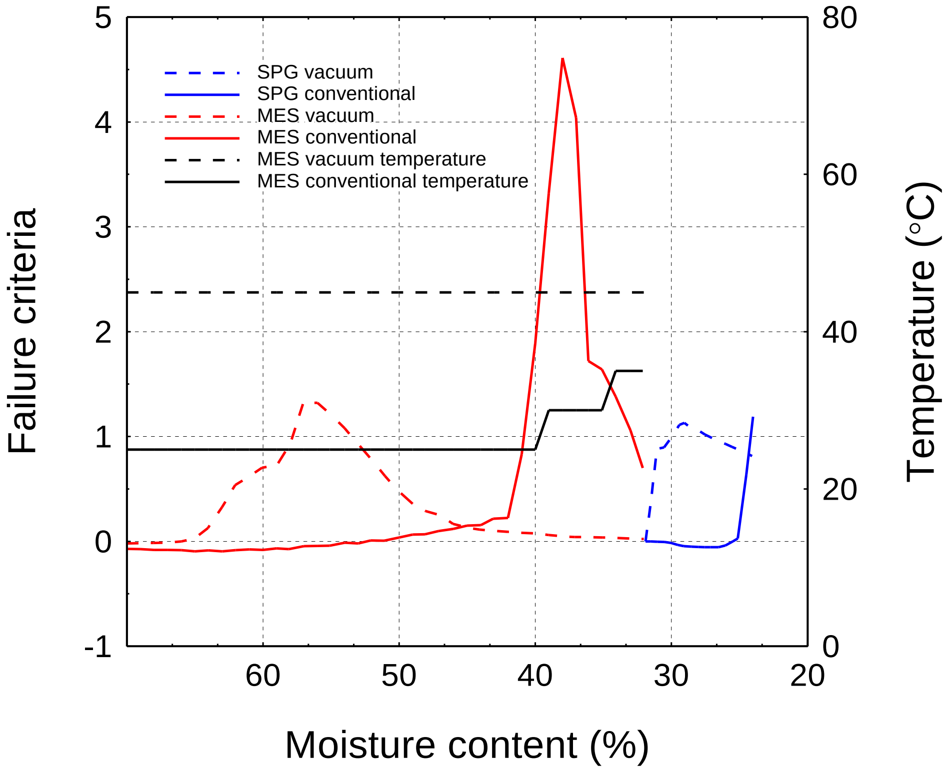

(a)

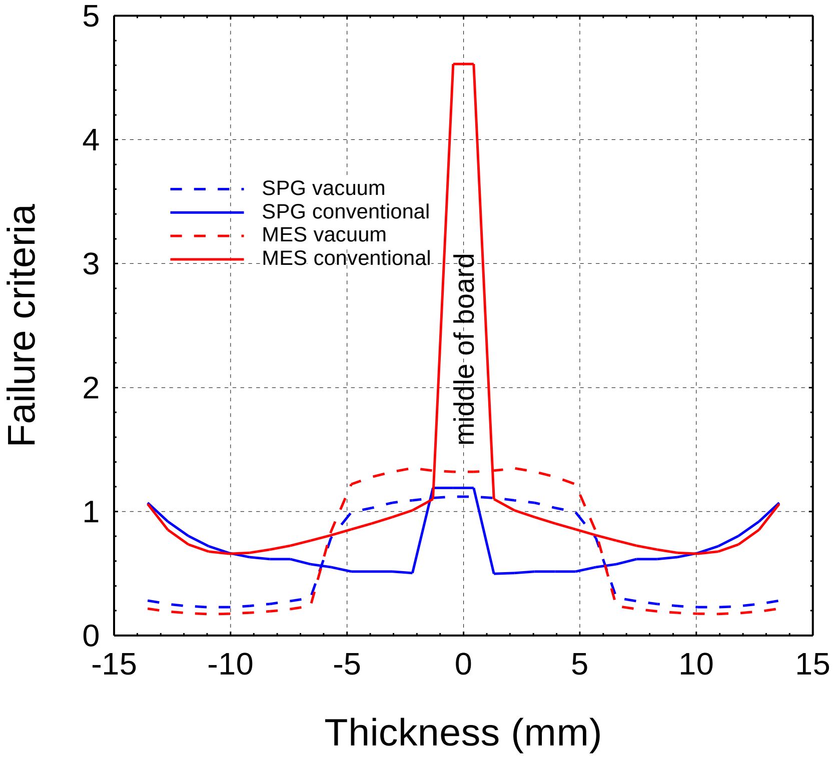

(b)

Figure 6.6 Tsai-Wu board end-split failure criteria versus moisture content during conventional and vacuum drying spotted gum and messmate, showing drying temperature for messmate (a). Tsai-Wu board end-split failure criteria profile in the thickness direction at peak failure (b). MES = messmate, SPG = spotted gum species

The evolution of the Tsai-Wu failure criteria for conventionally dried messmate, viewed from the centre of the board surface, at various stages of reducing moisture content during drying is shown in Figure 6.7. Figure 6.7a shows a schematic of the board symmetry plane and indicates the location of observed failure in subsequent images. Figures 6.7b-f show the evolution of Tsai-Wu failure at average board moisture contents of 85%, 69%, 39%, 34% and 32%. Tensile failure is shown to begin across most of the board surface (except the outer edge) and then intensify as drying progresses. The peak failure occurs at the board surface when the moisture content reaches 39% (Figure 6.7d). The magnitude of failure is similar across the board surface indicating that surface checking is likely to occur anywhere across the surface, as drying progresses. Indeed, for a wide board the presence of one single check is not able to relax the stress field over the entire width. Several checks will therefore form along the width, except very close to the edge, when the stress field is smaller for geometrical reasons. This matches the positions of surface checking failure observed from drying trials where surface checking occurred at various locations across the full surface of the board as shown in Figure 6.1b.

The Tsai-Wu failure, plotted against the reduction of average moisture content during drying, at the centre of the surface of the board, for conventional and vacuum dried messmate and spotted gum, is shown in Figure 6.8a. The results indicate that the maximum Tsai-Wu failure for messmate conventional drying (2.5) is 2.5 times higher than messmate vacuum drying (1.0), 4 times higher than spotted gum conventional drying (0.6), and 3 times higher than spotted gum vacuum drying (0.9). The observed percentage of surface checking failure (Table 1) for messmate conventional drying (29%) was 5 times higher than messmate vacuum drying (10%), 2 times higher than spotted gum conventional drying (11%) and 2 times higher than spotted gum vacuum drying (7%). The high susceptibility for conventionally dried messmate to surface checking during drying compared to the other drying regimes was both predicted by the model and observed during the trials. The Tsai-Wu failure curve for messmate conventional drying depicts an earlier lower magnitude peak that appears when the average moisture content reaches 69%. The second failure peak aligns with the sharp step in temperature and could potentially be reduced by implementing ramped changes in scheduled temperature.

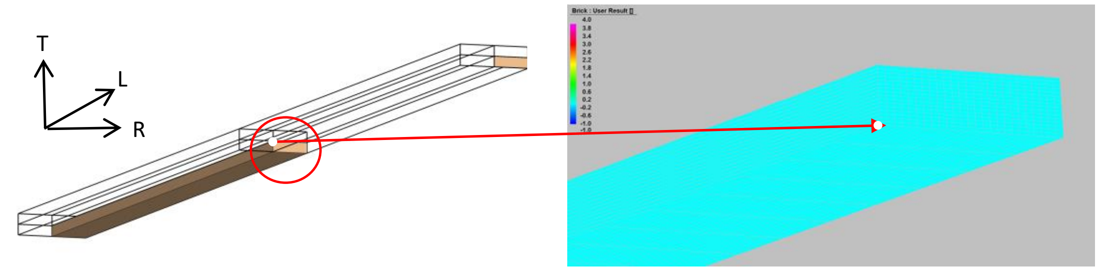

(a) (b) 85%

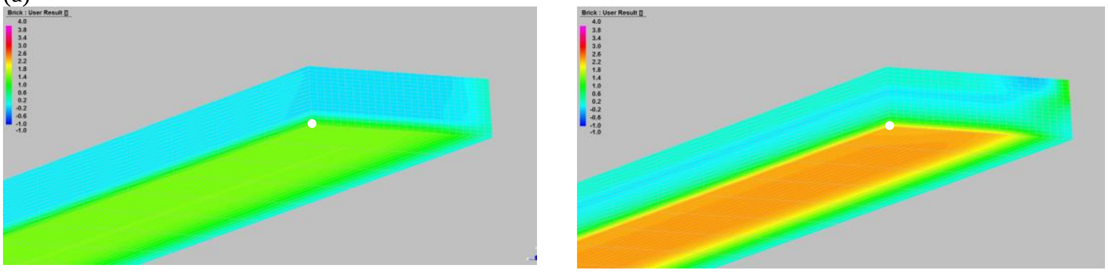

(c) 69% (d) 39% peak failure

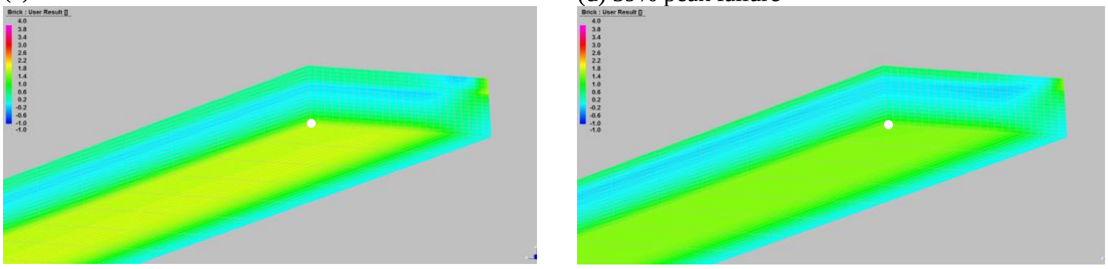

(e) 34% (f) 32%

Figure 6.7 Evolution of Tsai-Wu failure at the board surface, 1/8th symmetry model looking at the board-midsection (a), for conventionally dried messmate, at average board moisture contents 85% (b), 69% (c), 39% peak failure 1 (d), 34% (e), 32% (f). The white dot represents the centre of the board surface.

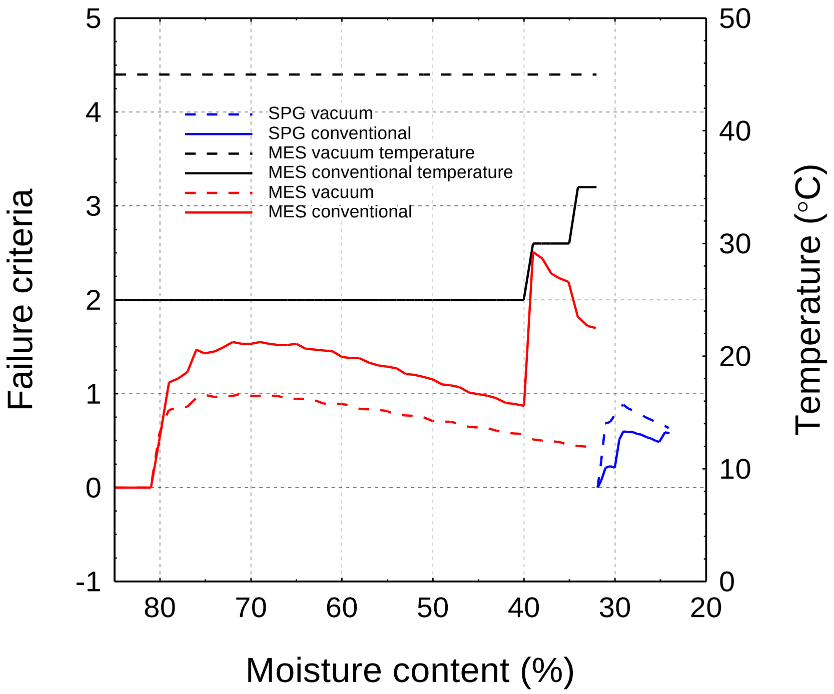

(a)

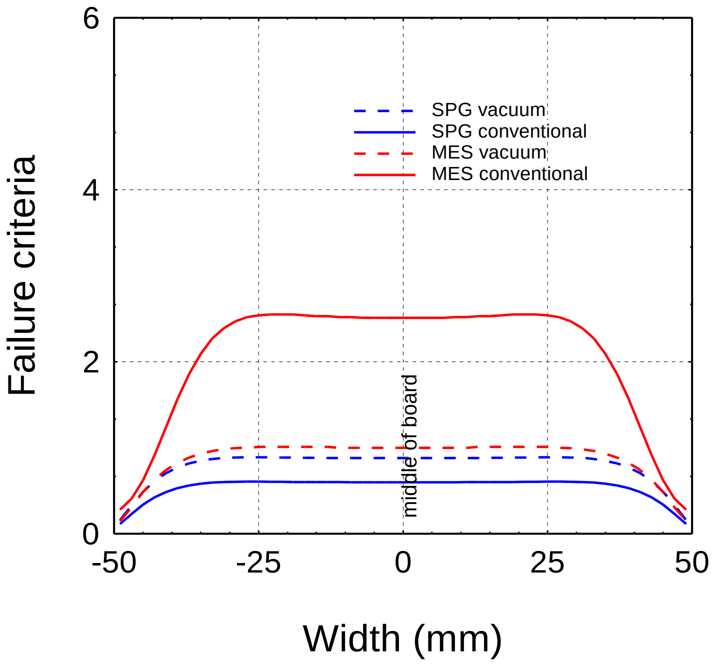

(b)

Figure 6.8 Tsai-Wu board surface check failure criteria versus moisture content during conventional and vacuum drying spotted gum and messmate (a). Tsai-Wu board surface check failure criteria profile in the width direction (board surface) at peak failure (b). MES = messmate, SPG = spotted gum species.

Figure 6.8b shows the Tsai-Wu failure in the board width direction, at the centre-surface of the board (red line as shown in Figure 6.5a), at the point in time when maximum failure occurs. The results display a similar failure profile for each species and drying regime, but with different magnitudes as described above. Simulations predicted the high chance of surface checking occurring for conventionally dried messmate, but not for vacuum dried messmate or conventional and vacuum dried spotted gum, as observed from the drying trials presented in Table 6.1.

An example of normal stresses in the board width (σ_{RR}) and thickness (σ_{TT}) directions and shear stress in the width/thickness (τ_{TR}) direction versus average board MC, for conventionally dried messmate, is provided in Figure 6.9a at the board-end centre-node (white dot Figure 6.5a) and Figure 6.9b viewed from the centre of the board surface. These stresses are used to determine the Tsai-Wu failure (equation 6-14) and the associated Tsai-Wu failure plots are also shown; the same as those plotted in Figure 6.6a and Figure 6.8a. In addition, the grey lines represent the ultimate tensile failure (as presented in Table 6.4) in the tangential direction (σ_{TTt}^{u}) at the board end (a), and radial direction (σ_{RRt}^{u}) at the board surface (b). Figure 6.9a indicates that stress in the thickness direction (σ_{TT}) is the predominant cause of end splitting as it is the only stress that exceeds the ultimate tensile stress in that direction σ_{TTt}^{u}, and also coincides with the Tsai-wu failure plot. This material direction mode of failure was not observed during drying trials where boards tend to split in the board width (R) direction as shown in Figure 6.1a. Again, the difference between the locations of simulated versus observed end split failure is a consequence of using the same two-dimensional T-L cross-sectional moisture content profiles along the board width direction (R) as previously mentioned from the observed Tsai-Wu failure trends.

Figure 6.9b shows the stress in the board width direction (σ_{RR}) is the predominant cause of surface checking, exceeding the untlimate tensile stress σ_{RRt}^{u} during the early, high moisture content, drying phase. This coincides with the Tsai-Wu failure results and the material direction mode of failure observed during drying trials (Figure 6.1b).

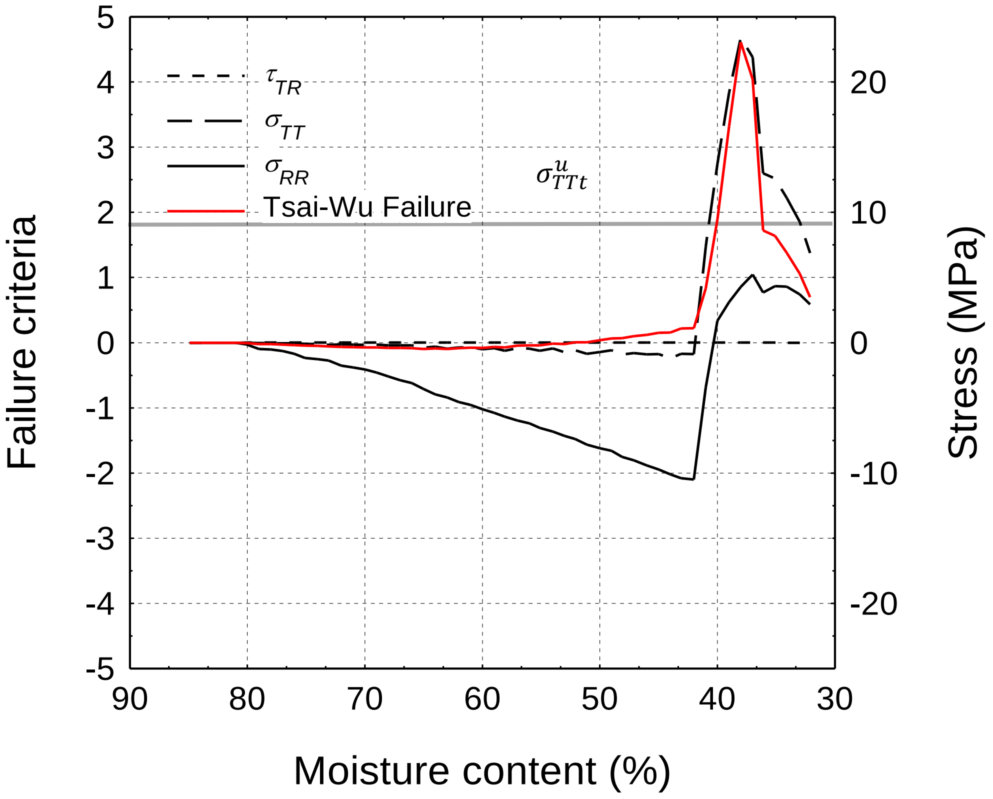

(a)

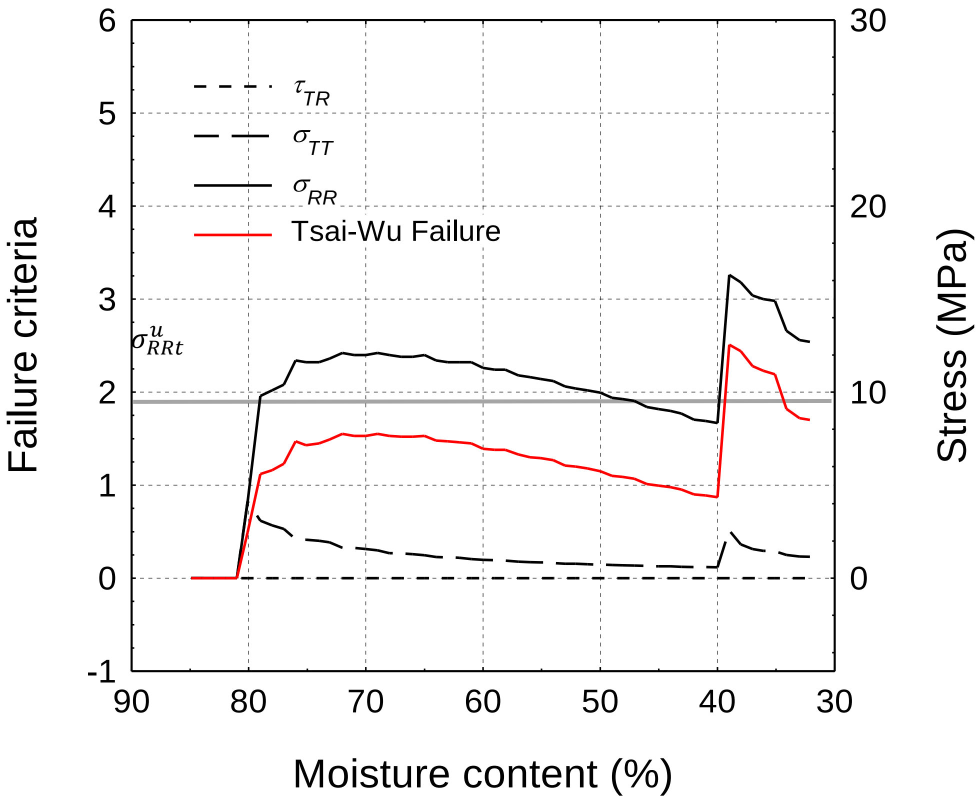

(b)

Figure 6.9 Tsai-Wu failure and normal stresses $(\sigma_{TT}, \sigma_{RR})$ *and shear stress* (τ_{TR}) *versus moisture content at the board end (a) and surface (b) for conventionally dried messmate. The grey line represents the ultimate tensile failure in the tangential direction* (σ^{u}_{TTt}) *at the board end (a) and radial direction* (σ^{u}_{RRt}) *at the board surface (b).*

As a final comment, inclusion of the viscoelastic creep and mechano-sorptive stress components in the FEA model is likely to contribute to an enhanced model and could explain why, for some drying scenarios, the failure criteria was significantly greater than the value of 1; the Tsai-Wu failure criteria threshold. By not including the mechano-sorptive strain in this model, simulations are likely to overestimate the stresses on the wood because the mechano-sorptive creep relax, or reduce, the stresses during drying by up to 40% or more of the total stress [106]. This effect, together with the viscoelastic creep, is also the main phenomenon able to explain stress reversal at the end of drying [116, 165]. The work presented here is relevant in that it demonstrates the potential of the approach to understand observed trends to further optimise the drying process while providing a platform for further refinement.

6.4 Conclusions

A predictive three-dimensional stress-strain FEA drying model, using measured and empirical wood properties combined with moisture gradient input data, was presented.

The model was able to reproduce the observed surface checking failure magnitude and location trends for vacuum and conventional drying of the two selected species, spotted gum and messmate. The model predicted that conventionally dried messmate was more susceptible to end splitting and surface checking than vacuum dried messmate. Maximum surface checking failure was predicted to occur across most of the surface of the board; a position of failure commonly observed in the drying trials.

The Tsai-Wu failure criteria was unable to precisely predict the localised position of end splitting observed in drying trials, which may be a result of using two-dimensional T-L cross-sectional moisture content profile input data to build a three dimensional FEA model.

The sharp changes in temperature and humidity set points used during conventional drying also translated into sharp spikes in stresses during drying. The same result was not observed for the smoother ramped schedules used in vacuum drying.

The FEA model shows the potential to predict the onset, location (at least for surface checking) and magnitude of stress-related drying degrade. We recommend further work to refine the model using a completely three-dimensional heat and mass transfer model to facilitate a more representative three-dimensional stress FEA drying model, including viscoelastic creep and mechano-sorptive strain.

This work contributes to a greater understanding of stress degrade formation in hardwoods during drying and may be used in future work to optimise wood drying by reducing drying times and limiting degrade. If one can accurately predict degrade during drying, then it is possible to simulate optimal drying schedules based on degrade limitations.

Chapter 7
Conclusions

This thesis was presented by publication. The original contribution to the literature was given in the form of four published journal articles and one submitted manuscript. The first objective of this research was to develop a robust and accurate hardwood-drying model, able to predict both vacuum and conventional drying behaviour. This was achieved by characterising the necessary wood properties and using deterministic psychrometric data derived from a series of drying trials as input parameters for the *TransPore* heat and mass transfer model. The second objective was to develop a stress/strain model able to predict surface checking and end split failure trends observed during drying trials. This was realised by using two-dimensional moisture content field profiles computed using the *TransPore* 2D model in the board thickness-length plane and, in conjunction with empirically generated mechanical wood properties, creating a three-dimensional FEA model in *Strand7*. Tsai-Wu failure criteria was used to investigate simulated end split failure at the board end and end check failure on the board surface. The magnitude and position of simulated end split and surface check failure was compared with drying trial observations.

In this final chapter of the thesis, we explain, in more detail, how both of these objectives were achieved. The chapter concludes by providing some possible directions for future research.

7.1 Summary and discussion

The objectives of this research were outlined in Chapter 1.3. In this final chapter we reiterate these objectives and demonstrate how they were achieved as a result of the work presented in the previous chapters of the thesis.

Objective 1. Develop a robust and precise hardwood heat and mass transfer drying model, able to predict both vacuum and conventional drying behaviour.

A review of the literature concluded that accurate determination of the key wood parameters of density, initial moisture content, permeability, mass diffusivity, porosity, tangential and radial shrinkage, and desorption isotherms are parameters necessary for precise deterministic modelling of the drying process. In order to meet such requirements, key wood parameters were characterised for each of the Australian hardwood species: spotted gum, messmate, jarrah and blackbutt.

This work relevant to this objective was presentedin Chapter 2, where we characterise the mass transfer properties of permeability and mass diffusivity. To achieve this, we developed a custom system to measure very low (less than 10^{-18} m^2) gas permeability values. For the cases where the gas permeability was outside of the range of the flowmeter used in experiments, the custom system decreased the lower bound range of measurable permeability values by four orders of magnitude, from 10^{-18} to 10^{-22} m^2. We found spotted gum to be highly impermeable, particularly in the radial direction as, even after 24 hours, no noticeable measurement could be made. Comparison of permeability and diffusion coefficient values of the Australian hardwood species tested with published data from international mixed species, revealed markedly lower values for the Australian hardwood species, highlighting their comparatively slow drying rates.

In Chapter 3 we characterised the species viscoelastic, shrinkage, desorption isotherm and transverse anatomy properties. Viscoelastic properties of wood, in terms of stiffness, internal friction and glass transition temperature were considerably different in the radial and tangential directions within and between species. We found the viscoelastic properties measured at lower frequencies to be more representative of static material.

The highly accurate, dynamic method of determining shrinkage was unable to characterise radial and tangential shrinkage for messmate, due to the existence of collapse shrinkage. To characterise the wood-water relations of this species, free of collapse, we proposed that thinner sample sections (in the R-T plane) should be used. That is, thinner samples less than the reported fibre length were proposed to ensure that the sample contained only severed fibres. The notion was that severed fibres would allow liquid water to flow from the severed openings, rather than by diffusion through the cell walls. This should reduce the effects of internal pressure (vacuum) and liquid tension forces during water removal, thus eliminating collapse occurring in the samples. This idea was trialled in the work presented in Chapter 4 and was proved to be a valid method to characterise shrinkage and desorption isotherm properties of collapse prone species. Progressively thinner samples of messmate were used in shrinkage experiments proving that collapse shrinkage can be avoided for this species when using 0.5 mm thick samples. This was a significant finding of the work.

Wood transverse anatomy properties, fibre cell wall thickness and porosity were characterised in Chapter 3, via a combination of microscopy and image analysis, indicating clear differences between species. Results linking species wood density with porosity produced a weak correlation and we concluded that the entire cross-sectional cellular morphology, the inclusion of wood vessels enabled the wood porosity to be more accurately determined. Therefore, transverse anatomy was further characterised by including vessels in porosity measurements as reported in Chapter 4. Results of the more comprehensive porosity measurements showed porosity to be an accurate predictor of wood density.

The shrinkage, desorption isotherm and anatomical properties for each species were measured in Chapters 3 and 4 and the results were summarised. The results indicated, that by comparing certain data related to drying degrade, it is possible to explain the observed difficulty in drying relevant to different species. Fibre geometry can be used to provide an indication of collapse propensity, and the ratio of total radial: tangential shrinkage seems to be linked to stress degrade propensity. Care must be taken however as other wood characteristics and properties may need to be considered such as the presence of interlocked grain.

Using the recorded kiln operating conditions from the actual drying trials and the measured input parameters reported in Chapters 2 to 4, the two-dimensional *TransPore* drying model was used to simulate vacuum and conventional drying and validate them against the drying trials reported in Chapter 5. A highlight of the work presented in Chapter 5 was, that by using measured diffusion coefficient values to adjust empirical formulae, the accuracy of the model was greatly improved.

A range of simulations were conducted, investigating drying in the board thickness-width and thickness-length planes. Little difference was observed between average moisture content curves of the two planes, indicating that the measured wood permeability and diffusion coefficient in the longitudinal direction are small enough to limit the effect of longitudinal migration even with the internal overpressure generated by vacuum-drying. Observation of the moisture content gradient curves in the longitudinal and thickness directions revealed more drying occurring in the thickness direction. This indicates that the drying is mainly due to diffusion in the thickness direction. Comparisons of the average moisture content and board core temperature were made between species and drying regimes. Compared with drying trials, the ability of the *TransPore* model to simulate average moisture content and temperature was accurate with a calculated error of between 1.5-10.4% for moisture content and 5.6 - 8 °C for temperature, depending on species.

Model simulations showed that a substantial overpressure (the difference between board core and kiln pressure) was produced during vacuum drying, when the wood moisture content was above FSP. Such overpressure was not present for conventional drying simulations; this overpressure contributes to the more rapid drying rates observed during the vacuum drying trials.

A sensitivity analysis was performed that focussed on the experimental characterisation of key model parameters, reinforcing that density, shrinkage, as well as isothermal and transverse mass diffusivity and permeability parameters are most sensitive for predicting final moisture content over a fixed run time, and should be measured per species, for accurate modelling. The results of the sensitivity study indicated that by using measured values of these key parameters, the model outputs provide excellent agreement with experimental observation despite the large range of species behaviour and variation in wood properties. *TransPore* model simulations and results of the sensitivity analysis both confirmed that contrary to softwood, it appears that longitudinal migration of water provides only a secondary effect, and that the tested hardwoods dry predominantly by diffusion. An important contribution of the modelling work presented is that not only can the model precisely predict the heat and mass transfer behaviour of a range of hardwood species, it is also robust enough to predict the behaviour for different types of drying scenarios such as convective and vacuum drying over a wide range of drying schedules.

Objective 2. Develop a FEA stress/strain model that can predict stress-related drying degrade failure

Chapter 6 concludes this work through the development of a predictive three-dimensional stress-strain finite element analysis (FEA) drying model, using measured and empirical wood properties combined with moisture gradient input data generated from the heat and mass transfer model presented in Chapter 5. Messmate and spotted gum species were chosen as they were identified in previous chapters as having the most contrasting wood properties and degrade susceptibility. The two-dimensional time-dependent moisture gradient outputs were used as input data to create a three-dimensional stress/strain model in the *Strand7* software, using FEA. As three-dimensional moisture gradient fields were not available, some assumptions were made to extend the two-dimensional field into three-dimensions. Additionally, a simplified drying mechanical model was assumed which includes elastic deformation and moisture induced shrinkage and excludes viscoelastic and mechano-sorptive creep. This assumption forced us to focus on the primary phase of drying, when surface checking and end splitting occurs, which is what we wanted to achieve. With these assumptions in mind, this work was considered as a feasibility study to investigate the concept of simulating stress-related drying degrade and to stimulate further research in this area.

The *TransPore* moisture content field data was produced at discrete time steps. For each time step the moisture content field data was inserted into the *Strand7* FEA model, in conjunction with wood material and mechanical properties. Some of the mechanical properties, such as shrinkage coefficients and mechanical moduli change non-linearly with moisture content. At each time interval the *Strand7* model was solved using a quasi-static solver.

After running the *Strand7* model and using the Tsai-Wu failure criteria we were able to predict that vacuum dried messmate was more susceptible to end splitting and surface checking than conventionally dried messmate, and both vacuum and conventionally spotted gum. The same trends were observed in experimental drying trials. Maximum surface check failure was predicted to occur across the board surface; a position of failure commonly observed in the drying trials.

The Tsai-Wu failure criteria failed to predict the localised position of end splitting observed in drying trials, which is likely to be a result of using two-dimensional input data to build a three dimensional FEA model. Excluding the moisture gradient in this direction reduces the simulated anisotropic stress field at the corners and edges of the board resulting in an under prediction of the location of end split at the board end. By considering this limitation, we proposed that by using input data from a three dimensional heat and mass transfer model, the FEA model's predictive capacity could be improved in the future.

The increased susceptibility for messmate species to end splitting and surface checking degrade is most likely linked to the comparatively high initial moisture content of this species, the lower overall tensile failure values and lower anisotropic shrinkage ratio, compared with spotted gum.

The sharp changes in temperature and humidity setpoints used during conventional drying also translated into sharp spikes in stresses being generated during drying. The same result was not observed for the smoother ramped schedules used in vacuum drying. This provides us with the potential to optimise current conventional schedules used by industry. By replacing stepped schedules with ramped schedules we could potentially eliminate stress spikes during drying, thus reducing degrade and improving current drying times.

The outcomes of this research are important in that they provide the hardwood industry with a tool that can accurately determine the drying rate of a wide range of hardwood species that is compliant across different types of drying. The key, sensitive wood parameters necessary to accurately model drying of Australian hardwood species have been identified. Without accurate measurement of the wood diffusivity, density, desorption isotherm and shrinkage characteristics, precise and robust modelling is not possible. This work also contributes to a greater understanding of stress degrade formation in hardwood during drying, and may be used in future work to optimise wood drying by reducing drying times and limiting degrade.

7.2 Directions for further research

The research presented in this thesis supports a number of opportunities for further research that would be worthy of engagement.

Regarding the heat and mass transfer model the following research activities could be useful.

- *Simulations using different board thicknesses*. As the thickness of boards increases, so too does the time required to dry. Testing the model precision for drying thicker boards, and comparing the ratio of vacuum to conventional drying time related to thickness would be useful for industry, particularly for making drying equipment investment decisions.

- *Simulations using circular cross-sectional dimensions*. Simulating drying of circular cross-sectional dimensions to replicate log drying would be beneficial for the power pole industry in order to predict the drying rate of different species and determine the optimal time to perform preservative treatment of logs.

- *Studying the effect of board length on drying rate*. The simulation of the drying of boards with varying length would provide a species dependent indication of the length at which drying rate is significantly reduced. This is due to the effect of higher longitudinal permeability and diffusivity of most species compared to those in the transverse direction. This would provide industries that use short wood components for product manufacture, the potential to dry shorter length boards at a faster rate.

- *Simulating wood preservation*. Investigations of the ability of the model to simulate combined pressure/vacuum preservation treatment of wood of varying dimension is of great interest to the wood preservation industry. The model could be used to simulate penetration of different preservative types/properties in relation to species, dimension and wood type (sapwood and heartwood).

- *Predicting heat pre-treatment of veneer peeling logs.* The model has the potential to optimise heat treatment (hot water soaking or steaming) of logs for veneer peeling. This is common practice when peeling high density hardwoods, to soften wood tissue and assist in peeling with improved quality.

- *Predicting heat penetration during veneer-based panel manufacture for curing adhesives.* Veneer-based panel products that use hot-set adhesives, require a certain temperature to cure them. Thicker panels take longer for the heat to reach the centre glue lines during hot-press manufacture. The model has the potential to optimise pressing times by predicting the heat transfer during hot pressing.

Regarding the stress/strain FEA model the following research activities could be beneficial.

- *Upgrade the current model*. The model should first be upgraded to a coupled three dimensional version of *TransPore,* inclusive of viscoelastic creep and mechano-sorptive strain, with a three dimensional stress/predictive failure model. This requires the heat and mass transfer model to be extended to three dimensions. Including the viscoelastic creep and mechano-sorptive strain should improve the model accuracy as it acts as a stress reliever during drying and the current model seems to overestimate stress during drying. This requires a series of laboratory tests to characterise the viscoelastic creep and mechano-sorptive wood properties.

- *Investigate the effect of ramping versus stepped schedules on stress-related degrade*. This would be particularly useful for most current conventional drying operations that use stepped drying schedules. The data provided in this thesis suggests that the drying stress could be substantially reduced by using ramped instead of stepped drying schedules.

Appendix A
Measured and formulated values used in the simulation

A.1 Measured wood properties

The following wood properties were measured using methods described in detail by Redman *et al*. [30, 75, 146]: wood moisture content, fibre saturation point, basic density, porosity, intrinsic gas permeability, bound water diffusion coefficient, shrinkage and desorption isotherm constant values.

The scalar measured wood properties for each of the four species are presented in the following table:

Table A.1 Measured wood properties for model input parameters

Measured wood properties	spotted gum (*C. citriodora*)	jarrah (*E. marginata*)	Blackbutt (*E. pilularis*)	messmate (*E. obliqua*)
Initial moisture content (%)	31.9	62.1	51.1	84.9
Fibre saturation point (%)	24.0	27.5	24.8	32.4
Basic density (kg/m^3)	921	636	674	489
Porosity (%)	22	38	38	49
Desorption isotherm parameters (eqn. 13)	c1 = 1.0047 c2 = 0.9076	c1 = 9716 c2 = 8401	c1 = 1.1847 c2 = 0.7211	c1 = 0.8080 c2 = 2.2796
Radial direction properties				
Gas absolute permeability (m^2)	0.01×10^{-20}	4.68×10^{-20}	1.44×10^{-20}	860×10^{-20}
Liquid absolute permeability (m^2)	0.01×10^{-20}	4.68×10^{-20}	1.44×10^{-20}	860×10^{-20}
Bound-water diffusion coefficient (m^2/s)	0.14×10^{-10}	0.26×10^{-10}	0.27×10^{-10}	0.70×10^{-10}
Tangential direction properties				
Gas absolute permeability (m^2)	0.35×10^{-20}	4.41×10^{-20}	1.70×10^{-20}	29.5×10^{-20}
Liquid absolute permeability (m^2)	0.35×10^{-20}	44100×10^{-20}	1.70×10^{-20}	29.5×10^{-20}
Bound-water diffusion coefficient (m^2/s)	0.14×10^{-10}	0.38×10^{-10}	0.17×10^{-10}	0.40×10^{-10}
Longitudinal direction properties				
Gas absolute permeability (m^2)	0.08×10^{-15}	67.4×10^{-15}	35.0×10^{-15}	55.5×10^{-15}
Liquid absolute permeability (m^2)	0.08×10^{-15}	67.4×10^{-15}	35.0×10^{-15}	55.5×10^{-15}
Bound-water diffusion coefficient (m^2/s)	0.60×10^{-10}	2.71×10^{-10}	2.35×10^{-10}	10.3×10^{-10}

A.2 Formulated physical properties

The following physical properties provide necessary scalar or tensor input parameters calculated using empirical formulae. Some of the properties discussed are specific to wood direction.

The heat capacity is described by Ben Nasrallah and Perré [166] as:

$$\overline{\rho c_p} = \rho_w(1113 + 4.85T + 4185X), \tag{A-1}$$

where X is the moisture content and T is the temperature (K).

The desorption isotherm is described by Perré and Turner [74] as:

$$\frac{P_v}{P_{vs}} = 1 - \exp(-c_1 A - c_2 A^2), \tag{A-2}$$

where c_1 and c_2 are constants and $A = X_b / X_{fspT}$.

The c_1 and c_2 desorption isotherm constants are species dependent and were generated previously by Redman *et al.* [30] (Table B.1) and the X_{fspT} term is previously explained (equation 5-10).

The capillary pressure is described by Perré and Turner [74] as:

$$P_c = 1.24 \times 10^5 \sigma(T)(S_w + 1 \times 10^{-4})^{-0.61}, \tag{A-3}$$

where $\sigma(T) = (77.5 - 0.185T) \times 10^{-3}$.

The relative liquid permeability is described by Perré and Turner [74] respectively in the tangential, radial and longitudinal directions as:

$$\begin{aligned} k_{rl}^T &= (S_w)^3, \\ k_{rl}^R &= k_{rl}^T, \\ k_{rl}^L &= (S_w)^8. \end{aligned} \tag{A-4}$$

The relative gas permeability is described by Perré and Turner [74] respectively in the tangential, radial and longitudinal directions as:

$$\begin{aligned} k_{rg}^{T} &= 1 + (2S_w - 3)(S_w)^2, \\ k_{rg}^{R} &= k_{rg}^{T}, \\ k_{rg}^{L} &= 1 + (4S_w - 5)(S_w)^4. \end{aligned} \tag{A-5}$$

The gaseous diffusion is described by Perré and Turner [74] respectively in the tangential, radial and longitudinal directions as:

$$\begin{aligned} D_{eff}^{T} &= 10^{-3} \times k_{rg}^{T} \times D_v, \\ D_{eff}^{R} &= 2 \times D_{eff}^{T}, \\ D_{eff}^{L} &= 100 \times D_{eff}^{T}, \end{aligned} \tag{A-6}$$

where D_v is the mass diffusivity of vapour in the air phase. Equations (A6) are divided by 100 for the spotted gum species to account for its very low permeability.

The diffusivity of vapour in gas is described by Dymond [167] as:

$$D_v = 2.2 \times 10^{-5} \left(\frac{1.013\times10^5}{P}\right)\left(\frac{T}{273}\right)^{1.75}. \tag{A-7}$$

In Chapter 5, some simulations used theoretical bound liquid diffusivities, detailed by Perré and Turner [74] and these are summarized below. In this section, we assume the gradient of bound water is the driving force. This allows two pseudo-diffusivities to be defined (bound water in the cell wall and air in the pores):

$$\begin{aligned} \widehat{D}_b &= \rho_s D_b, \\ \widehat{D}_v &= \frac{M_v}{RT} D_v \frac{\partial P_v}{\partial X_b}, \\ \widehat{D}_b &= \rho_s \exp\left(-12.8183993 + 10.8951601\, X_b - \frac{4300}{T+273.15}\right). \end{aligned} \tag{A-8}$$

Using homogenisation results, Perré and Turner [168] proposed the following correlations:

$$\begin{aligned}\widetilde{D}_b^R &= A_{series}(1 + 1.6(\varepsilon_g))^{1.8},\\ \widetilde{D}_b^T &= 1.8 * A_{series},\end{aligned} \tag{A-9}$$

where $A_{series} = \frac{1}{\frac{\varepsilon_s}{\widehat{D}_b} + \frac{\varepsilon_g}{\widehat{D}_v}}$.

A small percentage of ray cells have to be in parallel to the cell arrangement giving the final form of the radial macroscopic diffusivity as:

$$\rho_0 D_b^R = (1 - \varepsilon_{ray})\widetilde{D}_b^R + \varepsilon_{ray} \times \widetilde{D}_{ray}^R. \tag{A-10}$$

Typical values for ε_{ray} and $\widetilde{D}_{ray}^R$ are 0.05 and 0.1 x $\widehat{D}_v$ respectively [74]. To be consistent, the same amount of ray cells is put in series with tracheids in the tangential direction:

$$\rho_0 D_b^T = \frac{1}{\frac{1-\varepsilon_{ray}}{\widetilde{D}_b^T} + \frac{\varepsilon_{ray}}{\widetilde{D}_{ray}^T}}. \tag{A-11}$$

Due to the considerable length of wood fibres, the longitudinal macroscopic diffusivity is described by Perré and Turner [169] using a parallel model of the form:

$$\rho_0 D_b^L = \varepsilon_s \widehat{D}_b + \varepsilon_g \widehat{D}_v. \tag{A-12}$$

The thermal conductivity is described by Perré and Turner [168] using homogenisation in the R-T plane and using a parallel flow model in the longitudinal direction:

$$\begin{aligned}\tilde{\lambda}_0^R &= 0.46 \times \lambda_{series} + 0.54 \times \lambda_{parallel},\\ \tilde{\lambda}_0^T &= \left(\varepsilon_g \lambda_{air}^n + \varepsilon_s \hat{\lambda}_{s\perp}^n\right)^{\frac{1}{n}},\\ \lambda_0^L &= \varepsilon_g \lambda_{air} + \varepsilon_s \hat{\lambda}_{s//}\end{aligned} \tag{A-13}$$

with n=0.6 and $\hat{\lambda}_{s//} \approx 2 \times \hat{\lambda}_{s\perp}$, where $\lambda_{series} = \frac{1}{\frac{\varepsilon_s}{\hat{\lambda}_{s\perp}} + \frac{\varepsilon_g}{\lambda_{air}}}$ and

$\lambda_{parallel} = \varepsilon_s \hat{\lambda}_{s\perp} + \varepsilon_g \lambda_{air}$.

Properties with a subscript of 0 denote thermal conductivities at a MC equal to the fibre saturation point. The constant values λ_{air} is 0.023 W m^{-1} K^{-1} and $\hat{\lambda}_{s\perp}$ is 0.5 W m^{-1} K^{-1}.

The effect of ray cells is taken into account such that:

$$\lambda_0^R = \left(1 - \varepsilon_{ray}\right)\tilde{\lambda}_0^R + \varepsilon_{ray} \times \tilde{\lambda}_{ray//},$$
$$\lambda_0^T = \frac{1}{\frac{1-\varepsilon_{ray}}{\tilde{\lambda}_0^T} + \frac{\varepsilon_{ray}}{\tilde{\lambda}_{ray\perp}}}$$

(A-14)

with n=0.6 and$\lambda_{ray\perp}$ and $\lambda_{ray//}$ are evaluated with a density of 500 kg m^{-3}.

For any value of MC, the final expressions for conductivity read as:

$$\begin{aligned}\lambda^T(\rho, X) &= \left((1 - S_w)(\lambda_0^T)^n + S_w\left(\phi\lambda_{air}^n + \varepsilon_s\hat{\lambda}_{s\perp}^n\right)\right)^{\frac{1}{n}},\\ \lambda^R(\rho, X) &= \left((1 - S_w)(\lambda_0^R)^n + S_w\left(\phi\lambda_{air}^n + \varepsilon_s\hat{\lambda}_{s\perp}^n\right)\right)^{\frac{1}{n}},\\ \lambda^L(\rho, X) &= \left((1 - S_w)(\lambda_0^L)^n + S_w\left(\phi\lambda_{air} + \varepsilon_s\lambda_{s//}\right)^n\right)^{\frac{1}{n}},\end{aligned} \quad \text{(A-15)}$$

with n=0.6.

The heat transfer coefficient is computed from classical empirical laws expressing the Nusselt number from the Reynolds and Prandtl numbers [170]:

$$h_h = 0.023\frac{\lambda_a}{L}\mathrm{Pr}^{1/3}\left(\frac{v_g X P}{\mu_g R T}\right)^{0.8}, \quad \text{(A-16)}$$

where the humid air viscosity is defined as:

$$\mu_g = \frac{P_a\mu_a\sqrt{M_a} + P_v\mu_v\sqrt{M_v}}{P_a\sqrt{M_a} + P_v\sqrt{M_v}}, \quad \text{(A-17)}$$

the dry air viscosity is:

$$\mu_a = A_0 + A_1 T, \quad \text{(A-18)}$$

where $A_0 = 0.59 \times 10^{-5}$ and $A_1 = 4.2 \times 10^{-8}$

the water vapour viscosity is:

$$\mu_v = A_0 + A_1 T + A_2 T^2, \tag{A-19}$$

where $A_0 = -3.189 \times 10^{-6}$, $A_1 = 4.145 \times 10^{-8}$, $A_2 = -8.272 \times 10^{-13}$, and the Prandtl number is defined as:

$$\mathrm{Pr} = \frac{c_p \mu}{k}. \tag{A-20}$$

The mass transfer coefficient is computed from classic boundary layer theory and is defined as [170]:

$$h_m = \frac{h_h}{\rho c_p}. \tag{A-21}$$

A.3 Nomenclature

Latin letters

2D	two-dimensional	
3D	three-dimensional	
A	area	m^2
Ag	green cross–sectional area	mm^2
A_i	image area	mm^2
A_k	activation energy	J
A_{vj}	lumen area	$\mu\mathrm{m}^2$
DMA	dynamic mechanical analysis	
AS	Australian Standard	
AS/NZS	Australian and New Zealand Standard	
c_p	specific heat	$\mathrm{J\ kg^{-1}\ K^{-1}}$
C_L	amount of liquid tension collapse	%
c	molar concentration	$\mathrm{mol\ m^{-3}}$
$\overline{\overline{\mathbf{D}}}$	diffusivity tensor	$\mathrm{m^2\ s^{-1}}$
DBT	dry bulb temperature	°C
D_{gap}	gap between concave or convex faces	mm
D_{stress}	degree of residual drying stress	
E	modulus of elasticity	Pa
E*	complex modulus	Pa
E′	storage modulus	Pa
E″	loss modulus	Pa
EMC	equilibrium moisture content	%
ENGREF	l’École Nationale du Génie Rural des Eaux des Forêts	
ESEM	environmental scanning electron microscope	
e	sample thickness	m
FSP	fibre saturation point	
FWPA	Forest and Wood Products Australia	
G	area of green cross section	m^3
g	gravitational acceleration	$\mathrm{m\ s^{-2}}$
HPC	High Performance Computing	
Hz	frequency	Hz
h	specific enthalpy	$\mathrm{J\ kg^{-1}}$
h	heat transfer coefficient	$(\mathrm{W\ m^{-2}\ K^{-1}})$
IP	intersection point	
l_{fi}	fibre lumen contour length	$\mu\mathrm{m}$

l_{lj}	manually drawn contour length	μm
L	sample length	m
J	flux expression	
K	intrinsic permeability	m^2
$\overline{\overline{\mathbf{K}}}$	absolute permeability tensor	m^2
$\overline{\overline{\mathbf{k}}}$	relative permeability tensor	
k	Boltzmann's constant	
k_a	air permeability	m^2
k_L	deformation constant	
k_m	mass transfer coefficient	$m\ s^{-1}$
k_r	relative permeability	
L	Longitudinal	
L	sample thickness	m
l	length	m
M	molecular weight	$kg\ mol^{-1}$
MC	moisture content	
m	mass vapour transferred	
$\hat{\mathbf{n}}$	unit normal	
ΔP	pressure difference	Pa
$\overline{P}$	average pressure	Pa
$\boldsymbol{P}$	pressure	Pa
P	total liquid tension	$N\ m^{-2}$
P_l	pressure of the metastable liquid phase	Pa
P_K	pressure inside bubble	Pa
Q	flux	$m^2\ s^{-1}$
Q	the limit of plastic flow	$N\ m^{-2}$
q	External heat transfer coefficient	$W\ m^{-2}\ ^{o}C^{-1}$
QUT	Queensland University of Technology	
r	principle radii of curved surface	m
R	gas constant	$J\ mol^{-1}\ K^{-1}$
R	radial	
S	volume saturation	
S_o	collapse free shrinkage	%
t	time	s
T	temperature	K
t_{ave}	average cell wall thickness	μm
T_d	board thickness dry	m

T_g	board thickness green	m
TG	glass transition temperature	°C
v	mass velocity vector	m s^{-1}
v	air velocity	m s^{-1}
ν	Poisson's ratio	
V_g	green volume	m^3
V_S	volumetric shrinkage	m^3 m^{-3}
VSD	variable speed drive	
VOC	volatile organic compounds	
W	board width	m
W_d	board width dry	m
W_g	board width green	m
x	rectangular coordinate	m
x	molar fraction	(mol/mol)
X	magnification	
X	moisture content (dry basis)	kg kg^{-1}
Z_1	molecules per cm^3	cm^{-3}

Greek symbols

ε	volume fraction	
ϵ	strain	m m^{-1}
δ	phase angle	
δ	amplitude of deformation	
λ	thermal conductivity	W m^{-1} K^{-1}
ρ	intrinsic averaged density	kg m^{-2}
ρ_0	wood density	kg m^{-2}
σ	surface tension	N m^{-1}
$\sigma(T)$	surface tension at temperature T	N m^{-1}
μ	dynamic viscosity of air	Pa. s
φ	phase potential	
ϕ	porosity	m^3 m^{-3}
χ	depth scalar	m
ω	mass fraction	

Superscripts and subscripts

a	air
b	bound water
c	capillary

$calc$	calculated
crit	critical
e	enthalpy
eff	effective property
f	fibres
fsp	fibre saturation point
g	gas phase
i,j	structural direction of wood
L	longitudinal direction
l	liquid
r	relative
R	radial direction
s	solid phase
t	top
T	tangential direction
v	vapour phase
v_∞	vapour phase at boundary
v	vessels
w	liquid phase
wt	wood tissue
∞	value outside the boundary layer in the free stream

Bibliography

1. Nolan, G., et al., *Australian hardwood drying best practice manual*. 2003, Forest and Wood Products Research and Development Corporation: www.fwpa.com.au.
2. Redman, A.L., *Charaterisation of wood properties and tranverse anatomy for vacuum drying modelling of commercially important Australian hardwood species*. 2008, Forest and Wood Products Australia: Melbourne. p. 1-82.
3. Perré, P., *Fundamentals of Wood Drying*. 2007, Nancy, France.: A.R.BO.LOR.
4. Savard, M., V. Lavoie, and C. Trembala. *Technical and Economical Assessment of Superheated Steam Vacuum Drying of Northern Red Oak*. in *N.A.G.R.E.F. COST E15 Conference*. 2004. Athens, Greece: Forintek Canada Corp.
5. Redman, A.L., *Accelerated seasoning of plantaion grown Eucalyptus cloeziana and Eucalyptus pellita sawn timber*. 2007, Forest and Wood Products Australia. p. 1-30.
6. Salin, J.G., *Modeling of wood drying: a bibliography*. Drying Technology, 1991(9): p. 775-193.
7. Perré, P. and I.W. Turner, *Transpore: A generic heat and mass transfer computational model for understanding and visualising the drying of porous media*. Drying Technology, 1999. **17**(7): p. 1273-1289.
8. Pang, S., *Mathematical Modeling of Kiln Drying of Softwood Timber: Model Development, Validation and Practical Application*. Drying Technology, 2007. **25**: p. 421-431.
9. Perré, P., I. Turner, and R. Remond, *Chapter 1 - Comprehensive Drying Models Based on Volume-Averaging: Background, Application and Perspective*, in *Modern Drying Technology: Volume 1: Computational tools at different Scales*, E. Tsotsas and A.S. Mujumdar, Editors. 2007.
10. Vermaas, H.F., *Drying Eucalypts for Quality: Material Characteristics, Pre-drying Treatments, Drying methods, Schedules and Optimisation of Drying Quality*. South African Forestry Journal, 1995. **174**: p. 41-49.
11. Illic, J., *Shrinkage-related degrade and its association with some physical properties in Eucalyptus regnans F. Muell*. Wood Science and Technology, 1999. **33**: p. 425-437.
12. Alexiou, P.N., J.F. Marchant, and K.W. Groves, *Effect of pre-steaming on moisture gradients, drying stresses and sets, and face checking in regrowth Eucalyptus pilularis Sm.* Wood Science and Technology, 1990. **24**: p. 201-209.

13. Chafe, S.C. and J.M. Carr, *Effect of board dimensions and grain orientation on internal checking in Eucalyptus regnans.* Holzforschung, 1998. **52**: p. 434-440.

14. Salin, J.-G., *Numerical prediction of checking during timber drying and a new mechano-sorptive creep model.* Holz als Roh -und Werkstoff, 1992. **50**: p. 195-200.

15. Mugabi, P., et al., *Correlation between drying defects, their parameters and moisture gradients in kiln-dried, south African grown Eucalyptus grandis poles.* Maderas. Ciencia y tecnologia, 2010. **12**(3): p. 199-208.

16. Perré, P. and I.W. Turner, *A 3-D version of TransPore: a comprehensive heat and mass transfer computational model for simulating the drying of porous media.* Int. J. of Heat and Mass Transfer, 1999. **42**: p. 4501-4521.

17. Perré, P., *Multiscale modeling of drying as a powerful extension of the macroscopic approach: Application to solid wood and biomass processing.* Drying Technology, 2010. **28**: p. 944-959.

18. Carr, E., I. Turner, and P. Perré, *A new control-volume finite-element scheme for heterogeneous porous media: Application to the drying of softwood.* Chemical Engineering Technology, 2011. **34**(7): p. 1143-1150.

19. Redman, A.L., *Computational modelling of the vacuum drying of Australian Hardwoods.* 2010, Queensland Cyber Infrastructure Foundation: Brisbane. p. 1-43.

20. Redman, A.L., *Evaluation of super-heated steam vacuum drying viability and development of a predictive drying model for Australian hardwood species* 2011, Queensland Government Department of Employment, Economic Development and Innovation report for Forestry and Wood Products Australia. : www.fwpa.com.au. p. 128.

21. Siau, J.F., *Transport processes in wood.* 1984, Germany: Springer-Verlag.

22. Ressel, J.B., *Wood anatomy - an introduction.*, in *Fundamentals of wood drying.*, P. Perre, Editor. 2008, A.R.BO.LOR ENGREF: France.

23. Bootle, K.R., *Wood in Australia - Types, properties and uses.* 2 ed, ed. C. Pike. 2004, Sydney: McGraw Hill. 452.

24. Butterfield, B.G. and B.A. Meylan, *Three dimensional structure of wood.*, ed. C.a. Hall. 1980, USA.

25. Salin, J.G., *Problems and solutions in wood drying modelling: history and future.* Wood Material Science and Engineering, 2010. **5**: p. 123-134.

26. Perré, P. *The Numerical Modelling of Physical and Mechanical Phenomena Involved in Wood Drying: an Excellent Tool for Assisting with the Study of New Processes.* in *5th Int. IUFRO Wood Drying Conference*. 1996. Quebec, Canada.

27. Standards Australia, *AS/NZS 1080.1: 1997 Timber-Methods of Test - Method 1:*

Moisture content 1997, Australian and New Zealand Standard, distributed by SAI Global Limited.

28. Standards Australia, *AS/NZS 1080.3:2000 Timber-Methods of test-Method 3: Density*. 2000, Australian and New Zealand Standard, distributed by SAI Global Limited.
29. Redman, A.L., *Evaluation of super-heated steam vacuum drying viability and development of a predictive drying model for four Australian hardwood species*. 2011, Report for Forest and Wood Products Australia: http://www.fwpa.com.au. p. 134.
30. Redman, A.L., H. Bailleres, and P. Perré, *Characterization of viscoelastic, shrinkage and transverse anatomy properties of four Australian hardwood species.* Wood Material Science & Engineering, 2011. **6**(3): p. 95-104.
31. Hansmann, C., W.G. Wimmer, and A. Teischinger, *Permeability of wood - A review.* Wood Research, 2002. **47**(4): p. 1-16.
32. Milota, M.R., et al., *Gas permeavility of plantation loblolly pine.* Wood and Fiber Science, 1995. **27**(1): p. 34-40.
33. Innes, T.C., *Improving seasoned hardwood timber quality with particular reference to collapse*, in *Engineering*. 1996, University of Tasmania: Hobart.
34. Blakemore, P.A. and A.G. Langrish, *Effect of collapse on fitted diffusion coefficients for Victorian ash eucalypts.* Wood Sci. Technol., 2008. **42**: p. 535-549.
35. Dullien, F.A.L., *Porous media: Fluid transport and pore structure*. 1992, New York: Academic Press Inc.
36. Perré, P., *Chapter 7 - Fluid Migration in Wood*, in *Fundamentals of Wood Drying*, P. Perré, Editor. 2007, A.R.BO.LOR: Nancy. p. 125-156.
37. Choong, E.T. and O.K. Kimbler, *A technique of measuring water flow in woods of low permeability.* Wood Science, 1971. **4**: p. 32-36.
38. Choong, E.T., F.O. Tesoro, and F.G. Manwiller, *Permeability of twenty-two small diameter hardwoods growing on southern pine sites.* Wood and Fiber, 1974. **6**: p. 91-101.
39. Chen, P., G. Zhang, and J. Sambeek, *Relationships among growth rate, vessel lumen area and wood permeability for three central hardwood species.* Forest Products Journal, 1998. **48**(3): p. 87-90.
40. Perré, P., *Mesurement of softwoods permeability to air: importance upon the drying model.* Heat and Mass Transfer, 1987. **14**: p. 519-529.
41. Perré, P., *Transferts couplés en millieux poreux non-saturés. Possibilités et limitations de la formulation macroscopique. Habilitation à Diriger des Recherches.* INPL, Nancy, 1992.
42. Perré, P. and A. Karimi, *Fluid migration in two species of beech (Fagus silvatica and Fagus orientalis): a percolation model able to account for macroscopic measurements and anatomical*

observations. . Maderas. Ciencia y tecnologia, 2002. **4**(1): p. 50-68.

43. Koumoutsakos, A. and S. Avramidis, *Mass Transfer Characteristics of Western Hemlock and Western Red Cedar.* Holzforschung, 2002. **56**: p. 185-190.
44. Avramidis, S., *Chapter 6 - Bound water migration in wood*, in *Fundamentals of wood drying*, P. Perré, Editor. 2007, A.R.BO.LOR: Nancy. p. 105-124.
45. Philibert, J., *One and a half century of diffusion: Fick, Einstein, before and beyond.* Diffusion Fundamentals, 2005. **2**: p. 1.1-1.10.
46. Skaar, C., *Wood-water relations.* 1988, Springer-Verlag: Berlin. p. 283.
47. Olek, W., P. Perré, and J. Weres, *Inverse analysis of the transient bound water diffusion in wood.* Holzforschung, 2005. **55**: p. 38-45.
48. Cai, L., *Determinarion of diffusion coefficient for sub-alpine fir.* Wood Science and Technology, 2005. **39**: p. 153-162.
49. Agoua, E., S. Zohoun, and P. Perré, *A double climatic chamber used to measure the diffusion coefficient of water in wood in unsteady-state conditions: determination of the best fitting method by numerical simulation.* International Journal of Heat and Mass Transfer, 2001. **44**: p. 3731-3744.
50. Mackay, J.F.G., *Some Factors Influencing Water Vapour Diffusion in Hardwood Species.* Wood Science, 1971. **4**: p. 62-64.
51. Fotsing, J.A.M. and C.W. Tchagang, *Experimantal determination of the diffusion coefficients of wood in isothernal conditions.* Heat Mass Transfer, 2005. **41**: p. 977-980.
52. McMillen, J.M., *Stresses in wood during drying.* 1958, U.S. Department of Agriculture, Forest Service, Forest Products Laboratory: Madison, WI.
53. AFRDI, *Australian Timber Seasoning Manual*, ed. A.F.R.a.D. Institue. 1997, Launceston: Australasian Furnishing Research and Development Institue Limited. 199.
54. Salin, J.G., *Inclusion of the sorption hysteresis phenomenon in future drying models. Some basic considerations.* Maderas. Ciencia y tecnologia, 2011. **13**(2): p. 173-182.
55. Liu, F., et al., *Sorption Isotherm of Southern Yellow Pine—High Density Polyethylene Composites.* Materials, 2015. **8**(1): p. 368.
56. Schaffner, R.D., *Fundamental aspects of timber seasoning*, in *Engineering.* 1981, University of Tasmania: Hobart.
57. Oliver, A.R., *A model of the behaviour of wood as it dries (with secific reference to eucalypt materials)*, U.o. Tasmania, Editor. 1991: Tasmania.
58. Doe, P.E., et al. *Optimal Lumber Seasoning Using Acoustic Emission Sensing and Real Time Strain Modelling.* in *5th Int. IUFRO Wood Drying Conference.* 1996. Quebec,

Canada.

59. Wu, Q., *A investigation of some problems in drying of Tasmanian eucalypt timbers*, in *Engineering*. 1989, University of Tasmania: Hobart.

60. Booker, J.D., *Internal checking and collapse - which comes first?* 1994, NZFRI: Rororua.

61. Redman, A.L., *Improving Quality of Seasoned Tasmanian Eucalypt Timbers*, in *Engineering*. 2000, University of Tasmania: Hobart.

62. Brooke, A.S., *Optimisation of Hardwood Timber Drying Schedules*, in *Engineering*. 1999, University of Sydney: Sydney.

63. Turner, J.W. and P. Perré, *A comparison of the drying simulation codes TransPore amd Wood2D which are used for the modelling of two-dimensional wood drying processes.* Drying Technology, Special issue: Mathematical Modeling and Numerical Techniques for the Solution of Drying Problems, 1995. **13**(3): p. 695-735.

64. Ilic, M. and J.W. Turner, *Convective drying of the consolidated slab of wet porous material.* Int. J. Heat and Mass Transfer, 1989. **32**(12): p. 2351-2362.

65. Stanish, M.A., G.S. Schajer, and F. Kayihan, *Mathematical modelling of wood drying from heat and mass transfer fundamentals.* In Drying, 1985. **85**: p. 360-367.

66. Moyne, D., Basilico, and C., *High temperature drying of softwood and hardwood: drying kinetics and product quality interactions.* In Drying, 1985. **85**: p. 376-381.

67. Perré, P., S.B. Nasrallah, and G. Arnaud, *A theoretical study of drying: Numerical simulations applied to clay-brick and softwood.* In Drying, 1986. **1**(86): p. 382-390.

68. Lartigue, C., J.R. Puiggali, and M. Quintard, *A simplified study of moisture transport and shrinkage in wood.* In Drying, 1989. **89**: p. 169-175.

69. Turner, I.W. and P. Perré, *Vacuum Drying of Wood with Radiative Heating: II. Comparison between Theory and Experiment.* AIChE Journal, 2004. **50**(1): p. 108-118.

70. Truscott, S.L. and J.W. Turner, *A heterogeneous three-dimensional computational model for wood drying.* Applied Mathematical Modelling, 2005. **29**: p. 381-410.

71. Carr, E.J., I.W. Turner, and P. Perre, *A variable-stepsize Jacobian-free exponential integrator for simulating transport in heterogeneous porous media: Application to wood drying.* Journal of Computational Physics, 2013. **233**: p. 66-82.

72. Carr, E.J., I.W. Turner, and P. Perre, *A Dual-Scale Modeling Approach for Drying Hygroscopic Porous Media.* Multiscale Modeling & Simulation, 2013. **11**(1): p. 362-384.

73. Whitaker, S., *Simultaneous heat, mass and momentum transfer in porous media: A theory of drying.* Advances in Heat Transfer, 1977. **13**: p. 119-203.

74. Perré, P. and J.W. Turner, *A mesoscopic drying model applied to the growth rings of softwood:*

Mesh generation and simulation results. Maderas, Ciencia y technologia, 2008. **10**(3): p. 251-274.

75. Redman, A.L., et al., *Characterisation of wood-water relationships and transverse anatomy and thier relationship to drying degrade*. Wood Science and Technology, 2016. **50**(4): p. 739-757.
76. McGavin, R., *Analysis of small-log processing to achieve structural veneer from juvenile hardwood plantations*, in *Faculty of Science, School of Ecosystem and Forest Sciences*. 2016, University of Melbourne: Melbourne, Australia. p. 140.
77. Perre, P. and C. Moyne, *PROCESSES RELATED TO DRYING: PART II USE OF THE SAME MODEL TO SOLVE TRANSFERS BOTH IN SATURATED AND UNSATURATED POROUS MEDIA*. Drying Technology, 1991. **9**(5): p. 1153-1179.
78. Dhatt, G. and G. Touzot, *The finite element method displayed*, ed. Wiley-Interscience. 1984, New York.
79. Patanker, S.V., *Numerical heat transfer and fluid flow*, ed. H.P. Corporation. 1980, New York.
80. Alexiou, P.N., *Optimisation of an accelerated drying schedule for regrowth Eucalyptus pilularis Sm*. Holz als Roh- und Werkstoff, 1991. **49**: p. 153-159.
81. Stumbo, D.A. *How and why stresses occur during wood drying*. in *Drying Softwood and Hardwood Lumber for Quality and Profit*. 1990. Charlotte, North Carolina: Forest Products Research Society.
82. Brandao, A. and P. Perré. *The "Flying Wood" - A quick test to characterise the drying behaviour of tropical woods*. in *5th International IUFRO Wood Drying Conference*. 1996. Quebec, Canada.
83. Diawanich, P., N. Matan, and B. Kyokong, *Evolution of internal stress during drying, cooling and conditioning of rubberwood lumber*. European Journal of Wood Products, 2010. **68**: p. 1-12.
84. Svensson, S., *Strain and shrinkage force in wood under kiln drying conditions, II. Strain, shrinkage and stress measurements under controlled climate conditions*. Holzforschung, 1996. **50**(5): p. 463-469.
85. Watanabe, K., et al., *Nondestructive evaluation of drying stress level on wood surface using near-infrared spectroscopy*. Wood Science and Technology, 2013. **47**(2): p. 299-315.
86. Dengyun, T., et al., *Modeling and On-line Measurement of Drying Stress of Pinus massoniana Boards*. Drying Technology, 2007. **25**: p. 441-448.
87. Alexiou, P.N. and J. Carson, *Fundamental seasoning research in Australia - An inter-*

disiplinary approach. 1988, NSW Timber Advisory Council: Sydney. p. 1-16.

88. Schaffner, R.D. and P.E. Doe. *Surface checking reduction in eucalypt timbers using semi-permeable cotings*. in *Proceedings 21st Forest Products Research Conference*. 1984. Melbourne, Australia: CSIRO.
89. Schaffner, R.D. and P.E. Doe. *The application of an orthotropic Fickian diffusion model to timber drying*. in *Proceedings 20th Forest Products Research Conference*. 1981. Melbourne, Australia: CSIRO.
90. Oliver, A.R. *Shrinkage and creep in drying timber*. in *Proceedings of 21st Forest Products Research Conference*. 1984. Melbourne, Australia: CSIRO.
91. Ganowicz, R. and L. Muszynski. *Simulation of drying stresses in wood*. in *4th IUFRO International wood drying conference*. 1994. Rororua, New Zealand.
92. Mårtensson, A. and S. Svensson, *Stress-strain relationship of drying wood. Part1: Development of a constitutive model.* Holzforschung, 1997. **51**: p. 472-478.
93. Mårtensson, A. and S. Svensson, *Stress- strain relationship of drying wood. Part 2: Verification of a one-dimensional model and development of a two-dimensional model.* Holzforschung, 1997. **51**: p. 565-570.
94. Salinas, C., et al., *Simulation of the drying stresses in wood.* Mecánica Computacional, 2010. **29**: p. 8347-8354.
95. Pang, S., *MODELLING OF STRESS DEVELOPMENT DURING DRYING AND RELIEF DURING STEAMING IN PINUS RADIATA LUMBER.* Drying Technology, 2000. **18**(8): p. 1677.
96. Calos, N.J., et al., *Softwood drying project.* 1999: Forest and Wood Products Research and Development Corporation. p. 143.
97. Calos, N.J., et al., *Softwood Drying Project*, F.a.W.P. Australia, Editor. 1999, Forest and Wood Products Australia: Melbourne, Austrlaia. p. 145.
98. Dahlblom, O., S. Ormarsson, and H. Petersson, *Simulation of wood deformation processes in drying and other types of environmental loading**. Ann. For. Sci., 1996. **53**(4): p. 857-866.
99. Perré, P. and J. Passard, *A control-volume procedure compared with the finite-element method for calculatinf stress and strain during drying.* Drying Technology, 1995. **13**(3): p. 635-660.
100. Pang, S. *Modelling of stresses and deformation of radiata pine lumber during drying*. in *7th International IUFRO wood drying conference*. 2001. Tsukabu, Japan.
101. Ekevad, M., N. Lundgren, and J. Flodin, *Drying shrinkage of sawn timber of Norway spruce (Picea abies): Industrial measurements and finite element simulations.* Wood Material

Science & Engineering, 2011. **6**(1-2): p. 41-48.

102. Ormarsson, S., O. Dahlblom, and H. Petersson, *A numerical study of the shape stability of sawn timber subjected to moisture variation Part 1: Theory.* Wood Science and Technology, 1998. **32**(5): p. 325-334.
103. Ormarsson, S., O. Dahlblom, and H. Petersson, *A numerical study of the shape stability of sawn timber subjected to moisture variation Part 2: Simulation of drying board.* Wood Science and Technology, 1999. **33**(5): p. 407-423.
104. Ormarsson, S., O. Dahlblom, and H. Petersson, *A numerical study of the shape stability of sawn timber subjected to moisture variation.* Wood Science and Technology, 2000. **34**(3): p. 207-219.
105. W., R., *Study on the development of mathematical model of mechanival properties of some wood materials undergoing changes in their moisture content.* Prace Instytutu Technologii Drewna, 1973. **20**(2(66)): p. 18-138.
106. Haque, M.N., *Modelling of solar kilns and the development of an optimised schedule for drying hardwood timber*, in *Chemical Engineering.* 2002, University of Sydney: New South Wales, Australia. p. 354.
107. Booker, J.D., *Acoustic emission and surface checking in Eucalyptus regnans boards during drying.* Holz als Roh -und Werkstoff, 1994. **52**: p. 383-388.
108. Innes, T.C., *Collapse and internal checking in the latewood of Eucalyptus regnans F. Muell.* Wood Science and Technology, 1996. **30**: p. 373-383.
109. Cabrero, J.M., G. Kifle, and G. Gebremedhin, *Evaluation of failure criteria in wood members*, in *11th World Conference on Timber Engineering 2010 (WCTE 2010)*, A. Ceccotti, Editor. 2010, Trees and Timber Institute, National Research Council: Trentino, Italy. p. 1274-1280.
110. Mascia, N.T. and R.A. Simoni, *Analysis of failure criteria applied to wood.* Engineering Failure Analysis, 2013. **35**: p. 703-712.
111. Tsai, S.W. and E.M. Wu, *A General Theory of Strength for Anisotropic Materials.* Journal of Composite Materials, 1971. **5**(1): p. 58-80.
112. Tsai, S.W., *Theory of Composites Design.* 1992: Think Composites.
113. Vermaas, H.F. and M. Bariska, *Collapse during low temperature drying of Eucalyptus grandis W. Hill and Pinus silvestris L.* Holzforchung, 1995. **2**: p. 35-40.
114. Salin, J.G., *Modeling of wood drying: a bibliography.* Drying Technology, 1991. **9**: p. 775-793.
115. Perré, P., R. Rémond, and D. Aléon, *Energy Saving in Industrial Wood Drying Addressed by a Multiscale Computational Model: Board, Stack, and Kiln.* Drying

Technology, 2007. **25**: p. 75-84.

116. Perré, P. and J. Passard, *A physical and mechanical model able to predict the stress field in wood over a wide range of drying conditions*. Drying Technology, 2004. **22**: p. 24-44.

117. Bootle, K.R., *Wood in Australia - Types, properties and uses*. 2 ed, ed. C. Pike. 2005, Sydney: McGraw Hill. 452.

118. Rousset, P., P. Perré, and P. Girard, *Modification of mass transfer properties in poplar wood (P. robusta) by a thermal treatment at high temperature*. Holz Roh Werkst, 2004. **62**: p. 113-119.

119. Moura, M.J. and M.M. Figuerido, *Characterization of Eucalypt Wood by Mercury Porosimetry - Data Interpretation*. Bull. Mocrom. Industr. Corp., 2002. **13**(5): p. 8-9.

120. Agoua, E. and P. Perré, *Mass transfer in wood: Identification of structural parameters from diffusivity and permeability measurements*. Journal of Porous Media, 2010. **13**(11): p. 1017-1024.

121. AS/NZS:1080.3, *Timber - Methods of Test - Method 3: Density* 2000, Standards Australia: www.standards.com.au.

122. Perré, P., *MeshPore: a software able to apply image-based meshing techniques to anisotropic and heterogeneous porous media*. Drying Technology, 2005. **23**(9-11): p. 1993-2006.

123. Perré, P., *Experimental device for the accurate determination of wood-water relations on micro-samples*. Holzforschung, 2007. **61**(4): p. 419-429.

124. Ressel, J.B., *Wood anatomy - an introduction.*, in *Fundamentals of wood drying*, P. Perré, Editor. 2008, A.R.BO.LOR ENGREF: Nancy. p. 21-46.

125. Irvine, G.M., *The glass transition of lignin and hemicellulose and their measurement by different thermal analysis*. Tappi Journal, 1984. **67**(5): p. 118-121.

126. Placet, V., P. Perré, and J. Passard, *Viscoelastic properties of green wood across the grain measured by harmonic tests in the range 0-95°C: Hardwood vs. softwood and normal wood vs. reaction wood*. Holzforschung, 2007. **61**: p. 548-557.

127. Clarke, C.R.E., B. Palmer, and D. Gounden, *Understanding and adding value to Eucalyptus fibre*. Southern Forests: a Journal of Forest Science, 2008. **70**(2): p. 169-174.

128. Redman, A.L., *Improving quality of seasoned Tasmanian eucalypt species.*, in *Faculty of Engineering*. 2001, University of Tasmania: Launceston. p. 102.

129. Budgen, B., *Shrinkage and density of some Australian and South-east Asian timbers*. 1981, CSIRO, Australia: Melbourne.

130. Perré, P. and I. Turner, *Chapter 10 - Coupled heat and mass transfer*, in *Fundamentals of Wood Drying*, P. Perré, Editor. 2007, A.R.BO.LOR: Nancy. p. 203-241.

131. Zieminska, K., et al., *Fibre wall and lumen fractions drive wood density variation across 24 Australian angiosperms.* AoB Plants, 2013. **5**: p. 14.

132. Tiemann, H.D., *Collapse in Wood as Shown Through the Microscope.* Journal of Forestry Research, 1941. **39**(3): p. 271-282.

133. Kauman, W.G., *Cell collapse in wood.* 1965, CSIRO-Division of Forest Products: Melbourne. p. 1-66.

134. Dadswell, H.E., *The anatomy of eucalypt woods.* 1972, Commonwealth Scientific and Industrial Research Organisation: Melbourne. p. 1-40.

135. Perré, P., *Meshpore: A software able to apply image-based meshing techniques to anisotropic and heterogeneous porous media.* Drying Technology, 2005. **23**: p. 1993-2006.

136. Ressel, J.B., *Wood anatomy - an introduction.*, in *Fundamentals of wood drying*, P. Perre, Editor. 2008, A.R.BO.LOR ENGREF: Nancy, France. p. 19.

137. Bibiak, M., *Chapter 4 - Sorption isotherms of wood*, in *Fundamentals of Wood Drying*, P. Perré, Editor. 2007, A.R.BO.LOR: Nancy. p. 87-104.

138. Guernsey, F.W., *Collapse in western red cedar.* British Columbia Lumberman, 1951. **4**: p. 3.

139. Chafe, S.C., *The distribution and interrelationship of collapse, volumetric shrinkage, moisture content and density in trees of Eucalyptus regnans F. Muell.* Wood Science and Technology, 1985. **19**: p. 329-345.

140. Cuevas, L.E., *Shrinkage and collapse studies on Eucalyptus viminalis.* Journal of the Institute of Wood Science, 1969. **23**.

141. Pankevicius, E.R., *Influence of Position in Tree on Recoverable Collapse in Wood.* Forest Products Journal, 1961. **11**(3): p. 131-132.

142. Bisset, I.J.W. and E.L. Ellwood, *The relation of differencial collapse and shrinkage to wood anatomy in Eucalyptus regnans F.v.M. and E. gigantea Hook. F.* Australian Journal of Applied Science, 1950. **2**(1): p. 175-183.

143. Perré, P. and O. Wieslaw, *Chapter1 - From fundamentals to practice the interaction chain*, in *Fundamentals of Wood Drying*, P. Perré, Editor. 2007, A.R.BO.LOR.: Nancy, France. p. 1-9.

144. Harris, J.M., *Spiral grain and wave phenomena in wood formation*, ed. T.E. Timell. 1989, Berlin Heidelberg: Springer-Verlag. 215.

145. Raymond, C.A., et al., *Improving dimensional stability in plantation-grown Eucalyptus pilularis and E. dunii*, in *PN06.3017. Southern Cross- University report for Forestry and Wood Products Australia.* 2008: www.fwpa.com.au.

146. Redman, A.L., et al., *Mass transfer properties (permeability and mass diffusivity) of four*

Australian hardwood species. BioResources, 2012. **7**(3): p. 3410-3424.

147. Hamby, D.M., *A review of techniques for parameter sensitivity analysis of environmental models*. Environmental Monitoring and Assessment, 1994. **32**: p. 135-154.

148. O'Neill, R.V., R.H. Gardner, and J.B. Mankin, *Analysis of parameter error in a nonlinear model*. Ecological Modelling, 1980. **8**: p. 297-311.

149. Yu, C., J.J. Cheng, and A.J. Zielen, *Sensitivity analysis of the RESRAD, a dose assessment code*. Transactions of the American Nuclear Society, 1991. **64**: p. 73-73.

150. Rozsa, A. and R.G. Mills, *Index of kiln seasoning schedules*, in *Australian Timber Seasoning Manual*, G.C. Waterson, Editor. 1997, Australian Furniture Research and Development Institute: Launceston. p. 167-175.

151. Risbrudt, C.D., M.A. Ritter, and T.H. Wegner, *Wood handbook - Wood as an engineering material*. Centennial Edition ed. 2010, Madison, WI: U.S. Department of Agriculture, Forest Service, Forest Products Laboratory.

152. AS/NZS:4787, *Timber -Assessment of Drying Quality*. 2001, Standards Australia: www.standards.com.au.

153. Fernandez-Golfin, J.I. and H. Alvarez Noves. *Kiln and Continuous Vacuum Drying of Eucalyptus Globulus, Oak and Chestnut 27 and 50mm Thick Boards*. in *5th International IUFRO Wood Drying Conference*. 1996. Quebec City, Canada.

154. Möttönen, V., *Variation in Drying Behaviour and Final Moisture Content of Wood during Conventional Low Temperature Drying and Vacuum Drying of Betula pendula Timber*. Drying Technology, 2006. **24**: p. 1405-1413.

155. Redman, A.L., et al., *A relevant and robust vacuum-drying model applied to hardwoods*. Wood Science and Technology, 2017. **51**(4): p. 701-719.

156. Perré, P., *Multiscale aspects of heat and mass transfer during drying*. Transport in Porous Media, 2007. **66**: p. 59-76.

157. Redman, A., et al., *Heat and mass transfer modelling of vacuum drying Australian hardwoods*. Manuscript in preparation, 2016.

158. Strand7, *Theoretical Manual - Theoretical background to the Strand7 finite element analysis system*, ed. Strand7. 2005, Suite 1, Level 5, 65 York Street Sydney NSW 2000 Australia: Strand7.

159. Ekevad, M., et al., *Modelling of adequate pretwist for obtaining straight timber*. Wood Material Science & Engineering, 2006. **1**(2): p. 76-84.

160. Innes, T. and A.L. Redman, *Improvement of hardwood drying schedules*, Forest and Wood Products Australia (FWPA), Editor. 2005: www.fwpa.com.au. p. 114.

161. Lin, J. and A. Cloutier. *Finite Element Modelling of the Viscoelastic Behaviour of Wood*

During Drying. in *5th Int. IUFRO Wood Drying Conference*. 1996. Quebec, Canada.

162. Guitard, D. and F. El Amri, *Modèles prévisionnels de comportement élastique tridimensionnel pour les bois feuillus et les bois résineux*. Ann. For. Sci., 1987. **44**(3): p. 335-358.

163. Wang, S.J., C.M. Chui, and C.J. Lin, *Variations in ultrasonic wave velocity and dynamic Young's modulus with moisture contnet for Taiwana plantation lumber*. Wood and Fiber Science, 2002. **34**(3): p. 370-381.

164. Kretschmann, D.E., *Mechanical properties of wood*, in *Wood handbook - Wood as an engineerning material*, U.S.D.o. Agriculture, Editor. 2010, Forest Products Laboratory, USDA.

165. Rémond, R., J. Passard, and P. Perré, *The effect of temperature and moisture content on the mechanical behaviour of wood: a comprehensive model applied to drying and bending*. European Journal of Mechanics A/Solids, 2007. **26**: p. 558-572.

166. Nasrallah, S.B. and P. Perre, *Detailed study of a model of heat and mass transfer during convective drying of porous media*. International Journal of Heat and Mass Transfer, 1988. **31**(5): p. 957-967.

167. Dymond, J.H., *Handbook of Physical Properties of Liquids and Gases Pure Substances and Mixtures. Third Augmented and Revised Edition. By N. B. Vargaftik, Y. K. Vinogradov, and V. S. Yargin. Begell House, Inc., New York. 1996. 1359 pp. $165.00. ISBN 1-56700-063-0*. Journal of Chemical & Engineering Data, 1999. **44**(1): p. 165-165.

168. Perré, P. and I. Turner, *Determination of the Material Property Variations Across the Growth Ring of Softwood for the Use in a Heterogeneous Drying Model. Part2. Use of Homogenisation to Predict Bound Liquid Diffusivity and Thermal Conductivity*. Holzforschung, 2001. **55**: p. 417-425.

169. Perré, P. and I. Turner, *Determination of the material property variations across the growth ring of softwood for use in a heterogeneous drying model: Part 1 - Capillary pressure, tracheid model and absolute permeability*. Holzforchung, 2001. **55**(3): p. 318-323.

170. Bird, R.B., W.E. Stewart, and E.N. Lightfoot, *Transport Phenomena*. 1960, New York: John Wiley and Sons, Inc.